Characterization and Device Applications of II-VI Nanocomposites

by

Jason Randall Heine

B.S Materials Science and Engineering
Michigan Technological University, 1995

Submitted to the Department of
Materials Science and Engineering
in Partial Fulfillment of the Requirements
for the Degree of

Doctor of Philosophy

at the

Massachusetts Institute of Technology

June 2001

Signature of Author...
Department of Materials Science and Engineering
May 1, 2001

Certified by..................
Klavs F. Jensen
Lammot du Pont Professor of Chemical Engineering
Professor of Materials Science and Engineering
Thesis Supervisor

Accepted by..........................
Harry L. Tuller
Professor of Ceramics and Electronic Materials
Chair, Departmental Committee on Graduate Students

Characterization and Device Applications of II-VI Nanocomposites

by

Jason Randall Heine

Submitted to the Department of Materials Science and Engineering
on May 1, 2001 in Partial Fulfillment of the
Requirements for the Degree of Doctor of Philosophy in
Materials Science and Engineering

Abstract

This thesis describes the synthesis and characterization of CdSe core – ZnS shell (CdSe)ZnS nanocrystals, which behave as quantum dots (QDs), their incorporation into transparent polymers and ZnS, and possible device applications of the resulting luminescent materials.

The crystalline structure of these quantum dots is examined using XRD. The nature of the core-shell interface is inferred by comparison of the XRD spectra with calculated spectra and in consideration of TEM images of the QDs. The influence the addition of a shell material over the CdSe core has on the QD exciton energy is examined by comparing the measured and calculated change in band edge emission energy when ZnS or CdS are used as overcoat materials.

Methods of incorporating the QDs into various polymers are considered and the emission of a GaN LED/ QD-containing polymer composite structure is simulated and compared with the output of actual devices. The simulation is also used as a design tool in the production of a white-light LED. Embedding the QDs into ZnS films via an electrospray technique is carried out and the resulting films characterized with x-ray diffraction and photoluminesence measurements. QD film / ZnS film structures are also considered, with atomic layer deposition used as the method for depositing the ZnS to improve the film uniformity as well as to maintain high quality deposition at temperatures low enough to be compatible with the presence of QDs.

Finally, thin film devices are synthesized and the behavior of the QD photoluminescence when an electric field is applied is studied. Significant levels of photoluminescence quenching is observed when a voltage is applied across an ITO/ZnS/QD/ZnS/Al, and similar, devices. Various reasons for this quenching are considered.

Thesis Supervisor: Klavs F. Jensen
Title: Lammot du Pont Professor of Chemical Engineering

Acknowledgements

I would like to thank my advisor, Klavs Jensen, for his guidance and encouragement during my years working with him. He has always made time to be available for discussing both research and my future career direction, and his insights have been very valuable.

I also owe thanks to Professor Moungi Bawendi who was virtually a second advisor and provided much of the guidance that I needed while conducting my research. I am also very appreciative of the aid that my other thesis committee members, Prof. Rubner and Prof. Kimerling, provided with both laboratory equipment and supplies and by asking questions I had not considered.

While a new graduate student I relied heavily on Javier Rodriguez-Viejo, who got me started on the quantum dot work and taught me most of what I know about CVD systems and quantum dot synthesis. I especially appreciate his patience while teaching me how to operate equipment. I also thank Jinwook Lee for his help in lab and wish him well as he continues work with the quantum dots. Allie Linn, an undergraduate, was able, through her prior experience with atomic layer epitaxy, to explain several of the mysterious effects seen when we first began investigating atomic layer deposition of ZnS.

The camaraderie of my groupmates and the help they given me over the years has been invaluable: Brian Willis, Kathy Vaeth, Seth Rodgers, who helped get the simulation work started, Raj Venkataramani, David Quiram, Tamara Floyd, Sameer Ajmera, Nuria de Mas, Hang Lu, Rebecca Jackman, Maria Nevoraskaya, Istvan Lengyel, Aleks Franz, Matt Losey, Samara Firebaugh, and Leonel Arana, among others.

And with all the time I have spent in the basements of Chemistry buildings, the same sentiments apply to the Bawendi group: Bashir Daboussi, Fred Mikulec, Steve Empedocles, Ken Kuno, Catherine Leatherdale, Dima Dinega, Wing Woo, Vikram Sundar, Ken Shimizu, Robert Neuhauser, Hans Eisler, Mirna Vitasovic, Inhee Chung, and Drew.

My years at MIT would not have been nearly so enjoyable without the companionship of my friends: Jeev Makan, Aki Suwa, Mike Shin, Kevin Chen, Steve Ting, Mayank Bulsara, and many others. I especially want to note my apartmentmates Ellen Siem, Matt Currie, and Vab Andleigh. And special thanks to Vab for all his advice and for getting me to actually use my Bally's membership.

I am also grateful for the companionship and support from my fellow students in Graduate Christian Fellowship, especially the Wednesday Night Bible Study group. Many thanks to Donald Crankshaw for his prayers and his support, especially as fellow study co-leader. I also found encouragement and companionship with the congregation of Faith Lutheran Church. I am very thankful for their willingness to welcome me into their fellowship, and also into their homes during the holidays.

Finally, I wish to thank my family for their constant love and support over the many years of my education. I owe a great deal to my parents who worked very hard to give me a good education and encouraged me from kindergarten to graduate school.

Table of Contents

List of Figures

Chapter 2

Chapter 3

Chapter 4

Chapter 5

Chapter 6

Chapter 1

Introduction

1.1 Motivation for studying QD containing materials

Luminescent device fabrication would benefit from the development of a tunable wavelength luminescing material. This would enable the production of devices with different output wavelengths using the same material and processing technique. Currently, different pigments, phosphors, or semiconductors are required to produce devices with different output wavelengths. For example, light emitting diodes (LEDs) are fabricated using AlGaAs, AlGaInP,[1] and InGaN[2] for red, yellow through green, and blue output, respectively. Each of these semiconducting systems give off light corresponding to their respective band gaps. The band gaps are a function of semiconductor composition, necessitating the use of different semiconductors for different output wavelengths. Nanocomposites containing quantum dots (QDs) offer the ability to use a single material to generate all of the colors in the visible spectrum.

Quantum dots are nanometer sized crystals in which electrons and holes experience quantum confinement effects. This quantum confinement causes the energy of an electron-hole pair, or exciton, present in the crystal to be dependent on the crystallite size. When the electron-hole pair recombines a photon is given off which has an energy equal to the exciton energy. In particular, CdSe quantum dots ranging in size from 23 Å to 55 Å in diameter have been shown to produce light output from 470 nm to 625 nm.[3] The QDs can be incorporated into thin conducting films. These films can potentially be used in a wide range of devices including LEDs, laser diodes, and wide area, flat panel displays using low-voltage CL or alternating current thin film electroluminescence (ACTFEL).

To produce these devices highly luminescent and monodisperse QDs are required. Composite quantum dots (low band gap core with higher band gap outer shell) synthesized through wet chemical techniques using II-VI semiconductors are highly luminescent and are now well characterized.

1.2 Background

1.2.1 Physics of Quantum Dots

Quantum dots are nanoscale structures, which exhibit three dimensional confinement of electronic carriers, electrons and holes. With luminescence as the primary goal, the confinement of electron-hole pairs, or excitons, is of particular interest. When the exciton is confined to a region smaller than its bulk Bohr radius its energy is increased. The greater this confinement (the smaller the QD) the greater the exciton energy. This energy is released as a photon when the exciton recombines radiatively. Thus, by choosing the size of a quantum dot, luminescence in any color from blue to red can be chosen. Nonradiative recombination at defect sites, in the QD or on its surface, frequently dominate. Therefore, QD synthesis requires low defect density nanocrystals as well as electronic passivation of the nanocrystal surface. The absorption edge of the QDs varies with quantum dot size in the same way due to the necessity of the photon having enough energy to create an exciton.

1.2.2 (CdSe)ZnS Composite Quantum Dots

The quantum dots to be used are wurtzite CdSe nanocrystals which have been coated with two to four monolayers of wurtzite ZnS, denoted (CdSe)ZnS. The efficiency of the QD photoluminescence is given by the quantum yield (QY), i.e. the ratio of emitted photons to absorbed photons. Uncoated CdSe dots can luminesce with a QY of 10% when capped with trioctylphosphine oxide (TOPO), which binds to the surface Cd sites strongly. When the cap is changed to pyridine, which binds to the dot less strongly, the luminescence drops by a factor of 10 or more. The dependence of the luminescence efficiency on the capping group is due to the presence of surface states on the QD. With diameters ranging from 23 Å to 55 Å, a large fraction of the atoms in the dots are surface atoms. The resulting surface states provide nonradiative recombination pathways which greatly reduce the QY.

The nonradiative recombination problem has been partially mitigated by the addition of an inorganic cap, or shell, typically ZnS. This shell passivates the surface and also provides an energy barrier to the exciton. The energy barrier is in the form of the valence and conduction band offsets between CdSe and ZnS, which are both approximately 0.9 eV. The energy barrier is needed to prevent the electron and the hole from interacting with the surface. Overcoating the CdSe increases the luminescence, with QY reaching 50% in some cases.[3] Evidence of the passivation of the CdSe is also seen in the elimination of luminescent deep trap states in the smaller (<30 Å) dots. Uncoated small dots have a washed out, whitish luminescence due to the presence of radiative recombination at deep trap sites. Coating produces a nearly monochromatic blue luminescence. However, the passivation is not complete because exchanging the capping group for pyridine causes a factor of two or more drop in quantum yield. The dependence of the QY on the capping group suggests that the exciton still interacts with the surface of the composite dot.

1.2.3 Quantum Dots in Thin Films

Once formed the dots are incorporated into a thin film. There are several ways to go about this. The simplest way is to spin coat the dots onto a conductive material. The dots can then be left exposed or have another material deposited on top of them. Leaving the dots exposed enables accessibility by low energy electrons, such as those in a low-voltage CL device. Depositing another material as an electrical contact enables the production of a simple EL device. Contact materials include aluminum, a conductive polymer, or ZnS. Another way of incorporating the QDs is to embed them in a conductive material. This has be done with polymers, such as polyvinylcarbazole (PVK), and t-Bu-PBD (PBD),[4] and with inorganic materials, such as ZnSe[5] and ZnS[6].

1.3 Topics in This Thesis

Chapter 2 describes the effect of adding a passivating ZnS shell onto the CdSe core and how luminescence is improved. In particular, the behavior of the electron and hole wavefunctions when the CdSe QD is capped with TOPO, ZnS, and CdS is calculated. The loss of electron confinement and subsequent red-shift in QD luminescence when overcoated with CdS is found to agree with measurements. Furthermore, the crystallinity of the ZnS shell is analyzed using by modeling XRD spectra and comparing it to experiment.

Chapter 3 describes the process of incorporating (CdSe)ZnS nanocrystals into an optically clear polymer while maintaining high luminescence efficiencies. These QD – polymer composites are then used to modify the light emitted from a blue LED. A Monte-Carlo simulation has been developed which accurately reproduces the luminescence spectra emitted by these LED – polymer structures.

Chapter 4 describes the synthesis of (CdSe)ZnS QD containing ZnS films via a technique which simultaneously utilizes an electrospray to deposit the QDs onto a substrate surface while ZnS is grown over it via chemical vapor deposition (CVD). The film morphology and temperature constraints on the deposition conditions are examined.

Chapter 5 examines the use of a modified CVD process to get large area uniform ZnS film deposition. This technique, atomic layer deposition (ALD), and its implementation are described. Adding QDs into structures produced by ALD via spinning and casting are discussed. Optical experiments involving QD-layer/ZnS-layer structures are reviewed and possible physical explanations considered.

1.4 References

[1] M. Craford, Circuits and Devices **8** (1992) 24.
[2] S. N. Mohammad et. al., Proc. IEEE **83** (1995) 1306.
[3] B. O. Dabbousi, et. al., J. Phys. Chem., **101** (1997) 9463.
[4] B. O. Dabbousi, et. al., Appl. Phys. Lett. **66** (1995) 1316.

[5] M. Danek, et.al., Chem. Mater. **8** (1996) 173.
[6] J. Rodriguez-Viejo, et.al., Appl. Phys. Lett. **70** (1997) 2132.

Chapter 2

Synthesis, Optical and Structural Characterization of Highly Luminescent (CdSe)ZnS Core-Shell Quantum Dots

Highly luminescent (CdSe)ZnS composite quantum dots (QDs) with CdSe cores ranging in diameter from 23 Å to 55 Å may be useful phosphors for a wide range of applications. The narrow photoluminescence (FWHM ≤ 40 nm) from these composite dots spans most of the visible spectrum from blue through red with quantum yields of 30-50% at room temperature.[1] A determination of the structure of these (Cse)ZnS quantum dots would be useful in determining possible routes of improving them as well as how processing the QDs will effect their optical and electrical properties. In fact, these QDs have been characterized using a range of optical and structural techniques. Optical absorption and photoluminescence spectroscopies probe the effect of ZnS passivation on the electronic structure of the dots. Wavelength dispersive X-ray spectroscopy, X-ray photoelectron spectroscopy, small and wide angle x-ray scattering and transmission electron microscopy were used to analyze the composite dots and determine their chemical composition, average size, size distribution, shape and internal structure. Furthermore, the energy shift for the first excited state for (CdSe)ZnS and (CdSe)CdS dots with varying shell thickness has been modeled using a simplified theoretical approach. This chapter will focus on work done to characterize the growth of ZnS on CdSe cores and how the ZnS shell compares with that of a CdS shell and will refer to the other characterization work which is published in Ref. 1.

2.1 Introduction

Core-shell type composite quantum dots exhibit novel properties making them attractive from both an experimental and a practical point of view.[23456789] Overcoating nanocrystallites with higher band gap inorganic materials has been shown to improve the photoluminescence quantum yields by passivating surface non-radiative recombination sites. Particles passivated with inorganic shell structures are more robust than organically passivated dots and have greater tolerance to processing conditions necessary for incorporation into solid state structures. Some examples of core-shell quantum dot structures reported earlier include CdS on CdSe and CdSe on CdS,[2] ZnS grown on CdS,[3] ZnS on CdSe and the inverse structure,[4] CdS/HgS/CdS quantum dot quantum wells,[5] ZnSe overcoated CdSe,[6] and SiO_2 on Si.[7,8] Recently Hines and Guyot-Sionnest reported making (CdSe)ZnS nanocrystallites whose room temperature fluorescence quantum yield was 50%.[9]

This chapter describes the synthesis of a series of room temperature high quantum yield (30%-50%) core-shell (CdSe)ZnS nanocrystallites with narrow band edge luminescence spanning most of the visible spectrum from 470 nm to 625 nm. These particles are produced using a two step synthesis which is a modification of the methods of Danek et al.[6] and Hines et al.[9] ZnS overcoated dots are characterized spectroscopically and structurally using a variety of techniques. The optical absorption and photoluminescence spectra of the composite dots are measured and the lowest energy optical transition is modelled using a simplified theoretical approach. Also, the internal structure of the composite quantum dots and the lattice parameters of the core and shell are determined using wide angle x-ray scattering.

In addition to having higher efficiencies ZnS overcoated particles are more robust than organically passivated dots and potentially more useful for optoelectronic device structures. Electroluminescent devices (LED's) incorporating (CdSe)ZnS dots into heterostructure organic/semiconductor nanocrystallite light emitting devices may show greater stability.[1011] Thin films incorporating (CdSe)ZnS dots into a matrix of ZnS using electrospray organometallic chemical vapor deposition (ES-OMCVD) demonstrate more than two orders of magnitude improvement in the PL quantum yields (~10%) relative to identical structures based on bare CdSe dots.[12] In addition, these structures exhibit cathodoluminescence[12] upon excitation with high energy electrons and may potentially be useful in the production of alternating current thin film electroluminescent devices (ACTFELD).

2.2 Experimental Section

2.2.1 Materials

Trioctylphosphine oxide (TOPO, 90% pure) and Trioctylphospine (TOP, 95% pure) were obtained from Strem and Fluka respectively. Dimethyl cadmium ($CdMe_2$) and diethyl zinc ($ZnEt_2$) were purchased from Alfa and Fluka respectively and both materials were filtered separately through a 0.2μm filter in an inert atmosphere box. Trioctylphosphine selenide was prepared by dissolving 0.1 mols of Se shot in 100ml of TOP thus producing a 1M solution of TOPSe. Hexamethyl disilathiane(TMS_2S) was used as purchased from Aldrich. HPLC grade n-hexane, methanol, pyridine and n-butanol were purchased from EM Sciences.

2.2.2 Synthesis of Composite Quantum Dots

(CdSe)ZnS. Nearly monodisperse CdSe quantum dots ranging from 23 Å to 55 Å in diameter were synthesized via the pyrolysis of the organometallic precursors, dimethyl cadmium and trioctylphospine selenide, in a coordinating solvent, trioctylphosphine oxide (TOPO), as described previously.[13] The precursors were injected at temperatures ranging from 340-360°C and the initially formed small (d = 23 Å) dots were grown at temperatures between 290-300°C. The dots were collected as powders by precipitation[13] with methanol and then redispersed in hexane.

A flask containing 5g of TOPO was heated to 190°C under vacuum for several hours then cooled to 60°C after which 0.5 mL trioctylphosphine (TOP) was added. Roughly 0.1-0.4 μmols of CdSe dots dispersed in hexane were transferred into the reaction vessel via syringe and the solvent was pumped off.

Diethyl zinc ($ZnEt_2$) and hexamethyldisilathiane ($(TMS)_2S$) were used as the Zn and S precursors. The amounts of Zn and S precursors needed to grow a ZnS shell of desired thickness for each CdSe sample were determined as follows: First, the average radius of the CdSe dots was estimated from TEM or SAXS measurements. Next, the ratio of ZnS to CdSe necessary to form a shell of desired thickness was calculated based on the ratio of the shell volume to that of the core assuming a spherical core and shell and taking into account the bulk lattice parameters of CdSe and ZnS. For larger particles the ratio of Zn to Cd necessary to achieve the same thickness shell is less than for the smaller dots. The actual amount of ZnS that grows onto the CdSe cores was generally less than the amount added due to incomplete reaction of the precursors and to loss of some material on the walls of the flask during the addition.

Equimolar amounts of the precursors were dissolved in 2-4 mL TOP inside an inert atmosphere glove box. The precursor solution was loaded into a syringe and transferred to an addition funnel attached to the reaction flask. The reaction flask containing CdSe dots dispersed in TOPO and TOP was heated under an atmosphere of N_2. The temperature at which the precursors were added ranged from 140°C for 23 Å diameter dots to 220°C for 55 Å diameter dots.[14] When the desired temperature was reached the Zn and S precursors were added dropwise to the vigorously stirring reaction mixture over a period of 5-10 minutes.

After the addition was complete the mixture was cooled to 90 °C and left stirring for several hours. 5 mL of butanol were added to the mixture to prevent the TOPO from solidifying upon cooling to room temperature. The overcoated particles were stored in their growth solution to ensure that the surface of the dots remained passivated with TOPO. They were later recovered in powder form by precipitating with methanol and redispersed into a variety of solvents including hexane, chloroform, toluene, THF and pyridine.

(CdSe)CdS. Cadmium selenide nanocrystallites with diameters between 33.5-35 Å were overcoated with CdS to varying thicknesses using the same basic procedure as that outlined for the ZnS overcoating. The CdS precursors used were Me_2Cd and $(TMS)_2S$. The precursor solution was dripped into the reaction vessel containing the dots at a temperature of 180°C and a rate of ~1 mL/min. The solution became noticeably darker as the overcoat precursors were added. Absorption spectra taken just after addition of precursors showed a significant shift in the absorption peak to the red. In order to store these samples it was necessary to add equal amounts of hexane and butanol since the butanol by itself appeared to flocculate the particles.

2.2.3 Optical Characterization

UV-Visible absorption spectra were acquired on an HP 8452 diode array spectrophotometer. Dilute solutions of dots in hexane were placed in 1cm quartz cuvettes and their absorption and corresponding fluorescence were measured. The photoluminescence spectra were taken on a SPEX Fluorolog-2 spectrometer in front face collection mode. The room temperature quantum yields were determined by comparing the integrated emission of the dots in solution to the emission of a solution of rhodamine 590 or rhodamine 640 of identical optical density at the excitation wavelength.

2.2.4 Wide Angle X-Ray Scattering (WAXS)

The wide angle X-ray powder diffraction patterns were measured on the same setup as the SAXS in polymer dispersions. The TOPO/TOP capped nanocrystals were precipitated with methanol and exchanged with pyridine. The samples were prepared by dropping a heavily concentrated solution of nanocrystals dispersed in pyridine onto silicon wafers. A slow evaporation of the pyridine leads to the formation of glassy thin films which were used for the diffraction experiments.

2.3 **Results and Analysis**

2.3.1 Synthesis of Core-Shell Composite Quantum Dots

We use a two step synthetic procedure similar to that of Danek et al.[6] and Hines et. al.[9] to produce (CdSe)ZnS core-shell quantum dots. In the first step we synthesize nearly monodisperse CdSe nanocrystallites ranging in size from 23 Å to 55 Å via a high temperature colloidal growth followed by size selective precipitation.[13] These dots are referred to as "bare" dots in the remainder of the text, although their outermost surface is passivated with organic TOPO/TOP capping groups. Next, we overcoat the CdSe particles in TOPO by adding the Zn and S precursors at intermediate temperatures.[14] The resulting composite particles are also passivated with TOPO/TOP on their outermost surface.

The temperature at which the dots are overcoated is very critical. At higher temperatures the CdSe seeds begin to grow via Ostwald ripening and their size distribution deteriorates leading to broader spectral linewidths. Overcoating the particles at relatively low temperatures could lead to incomplete decomposition of the precursors or to reduced crystallinity of the ZnS shell. An ideal growth temperature is determined independently for each CdSe core size to ensure that the size distribution of the cores remains constant and that shells with a high degree of crystallinity are formed.[14]

The concentration of the ZnS precursor solution and the rate at which it is added are also critical. Slow addition of the precursors at low concentrations ensures that most of the ZnS grows heterogeneously onto existing CdSe nuclei instead of undergoing homogeneous nucleation. This probably does not eliminate the formation of small ZnS particles completely so a final purification step in which the overcoated dots are subjected to size selective precipitation provides further assurance that mainly (CdSe)ZnS particles are present in the final powders.

2.3.2 Optical Characterization

The synthesis presented above produces ZnS overcoated dots with a range of core and shell sizes. Figure 2.1 shows the room temperature photoluminescence spectra (PL) of CdSe dots ranging from 23 Å to 55 Å in diameter before (dashed lines) and after (solid lines) overcoating with 1-2 monolayers of ZnS. The definition of a monolayer here is a shell of ZnS which measures 3.1 Å (the distance between consecutive planes along the [002] axis in bulk wurtzite ZnS) along the major axis of the prolate shaped dots. The PL quantum yield increases from 5-15% for bare dots to values ranging from 30% to 50% for dots passivated with ZnS. In smaller CdSe dots the surface to volume ratio is very high and the PL for TOPO capped dots is dominated by broad deep trap emission due to incomplete surface passivation. Overcoating with ZnS suppresses deep trap emission by passivating most of the vacancies and trap sites on the crystallite surface resulting in PL which is dominated by band-edge recombination.

In order to understand the effect of ZnS passivation on the optical and structural properties of CdSe dots we synthesized a large quantity of ~40 Å diameter CdSe dots. We divided this sample into multiple fractions and added varying amounts of Zn and S precursors to each fraction at identical temperatures and addition times. The result was a series of samples with similar CdSe cores but with varying ZnS shell thickness. Figure 2.2 shows the progression of the absorption spectrum for these samples with ZnS coverages of approximately 0 (bare TOPO capped CdSe), 0.65, 1.3, 2.6 and 5.3 monolayers (see beginning of this section for definition of number of monolayers). The spectra reflect a constant area under the lowest energy $1S_{3/2}$-$1S_e$ absorption peak (constant oscillator strength) for the samples with varying ZnS coverages. As the thickness of the ZnS shell increases there is a shift in the $1S_{3/2}$-$1S_e$ absorption to the red, reflecting an increased leakage of the exciton into the shell, as well as a broadening of the absorption peak indicating a distribution of shell thicknesses. The left hand side of Figure 2.2 shows an increased absorption in the ultraviolet with increasing ZnS coverage as a result of direct absorption into the higher band gap ZnS shell.

The evolution of the PL for the same ~40 Å diameter dots with ZnS coverage is displayed in Figure 2.3. As the coverage of ZnS on the CdSe surface increases we see a dramatic increase in the fluorescence quantum yield followed by a steady decline after ~1.3 monolayers of ZnS. The spectra are red shifted (slightly more than the shift in the absorption spectra) and show an increased broadening at higher coverage. The inset to Figure 5 charts the evolution of the quantum yield for these dots as a function of the ZnS shell thickness. For this particular sample the quantum yield starts at 15% for the bare TOPO capped CdSe dots and increases with the addition of ZnS approaching a maximum value of 50% at approximately ~1.3 monolayer coverage. At higher coverages the quantum yield begins to decrease steadily until it reaches a value of 30%

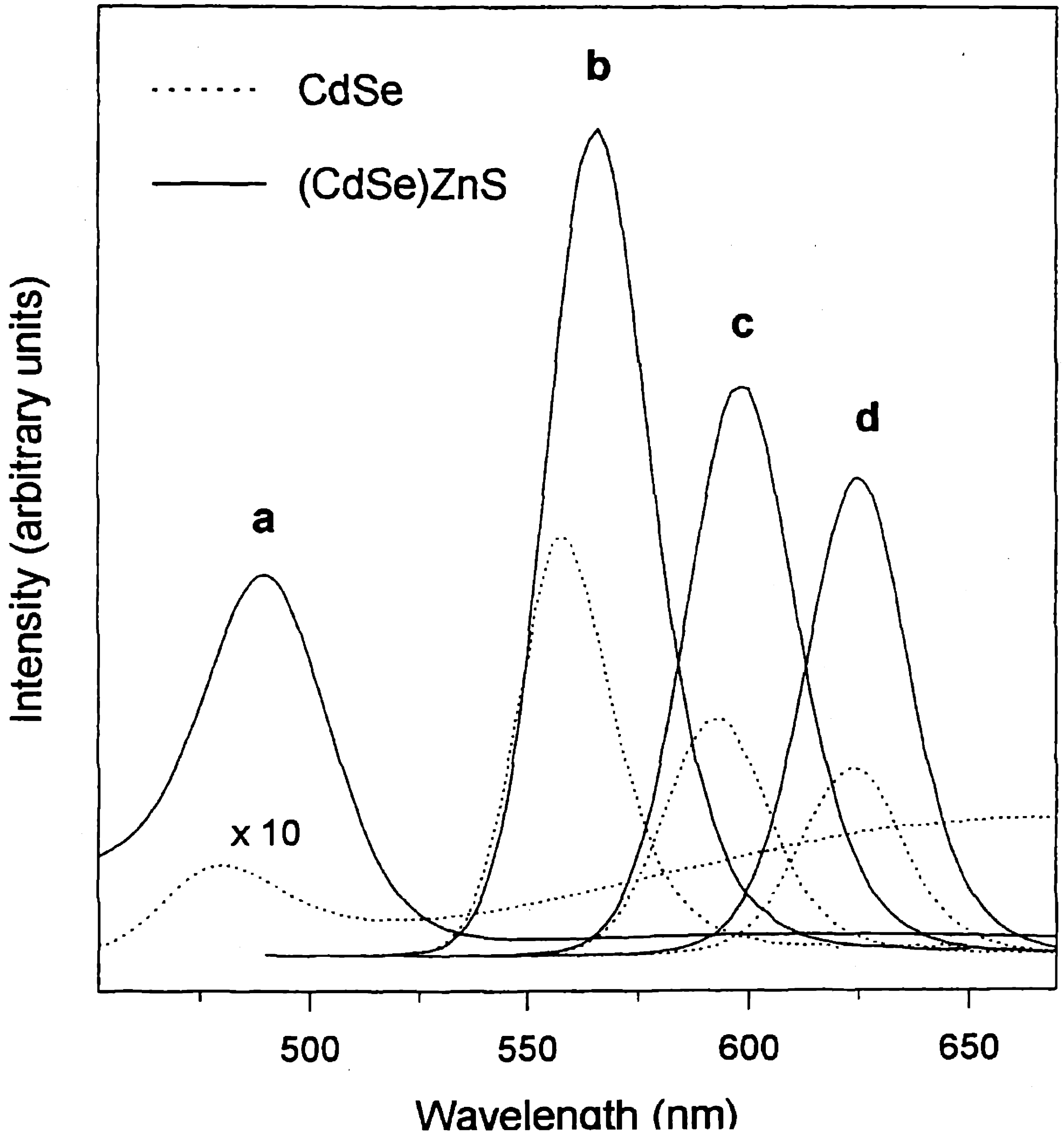

Figure 2.1 Absorption spectra for bare (dashed lines) and 1-2 monolayer ZnS overcoated (solid lines) CdSe dots with diameters measuring (a) 23 Å, (b) 42 Å, (c) 48 Å, and (d) 55 Å. The absorption spectra for the (CdSe)ZnS dots are broader and slightly red-shifted from their respective bare dot spectra.

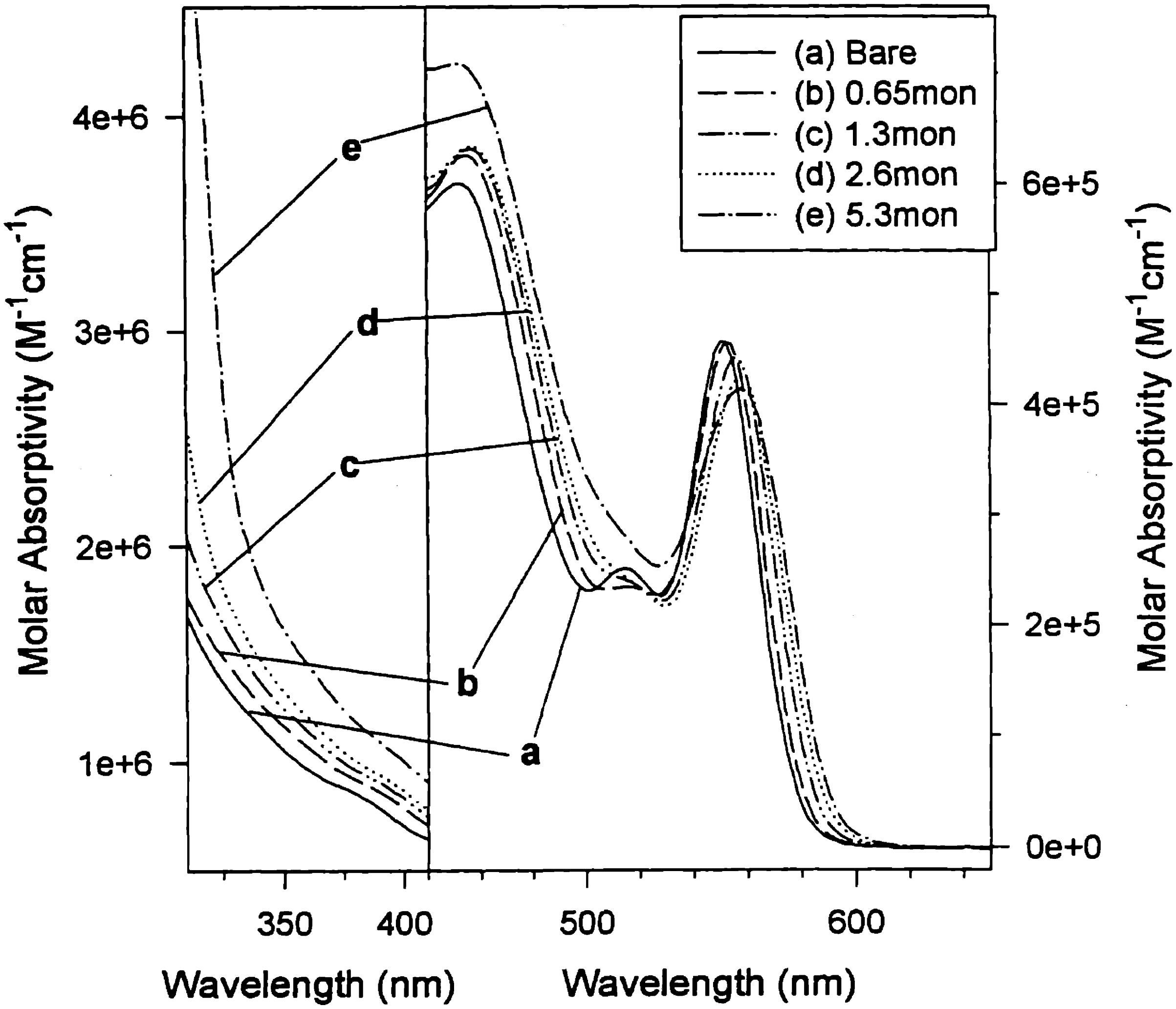

Figure 2.2 Absorption spectra for a series of ZnS overcoated samples grown on identical 42 Å ± 10% CdSe seed particles. The samples displayed have the following coverages: (a) bare TOPO capped, (b) 0.65 monolayers, (c) 1.3 monolayers, (d) 2.6 monolayers, and (e) 5.3 monolayers. (see definition for monolayers in text). The right hand side shows the long wavelength region of the absorption spectra showing the lowest energy optical transitions. The spectra demonstrate an increased red-shift with thicker ZnS shells as well as a broadening of the first peak as a result of increased polydispersity. The left hand side highlights the ultra-violet region of the spectra showing an increased absorption at higher energies with increasing coverage due to direct absorption into the ZnS shell.

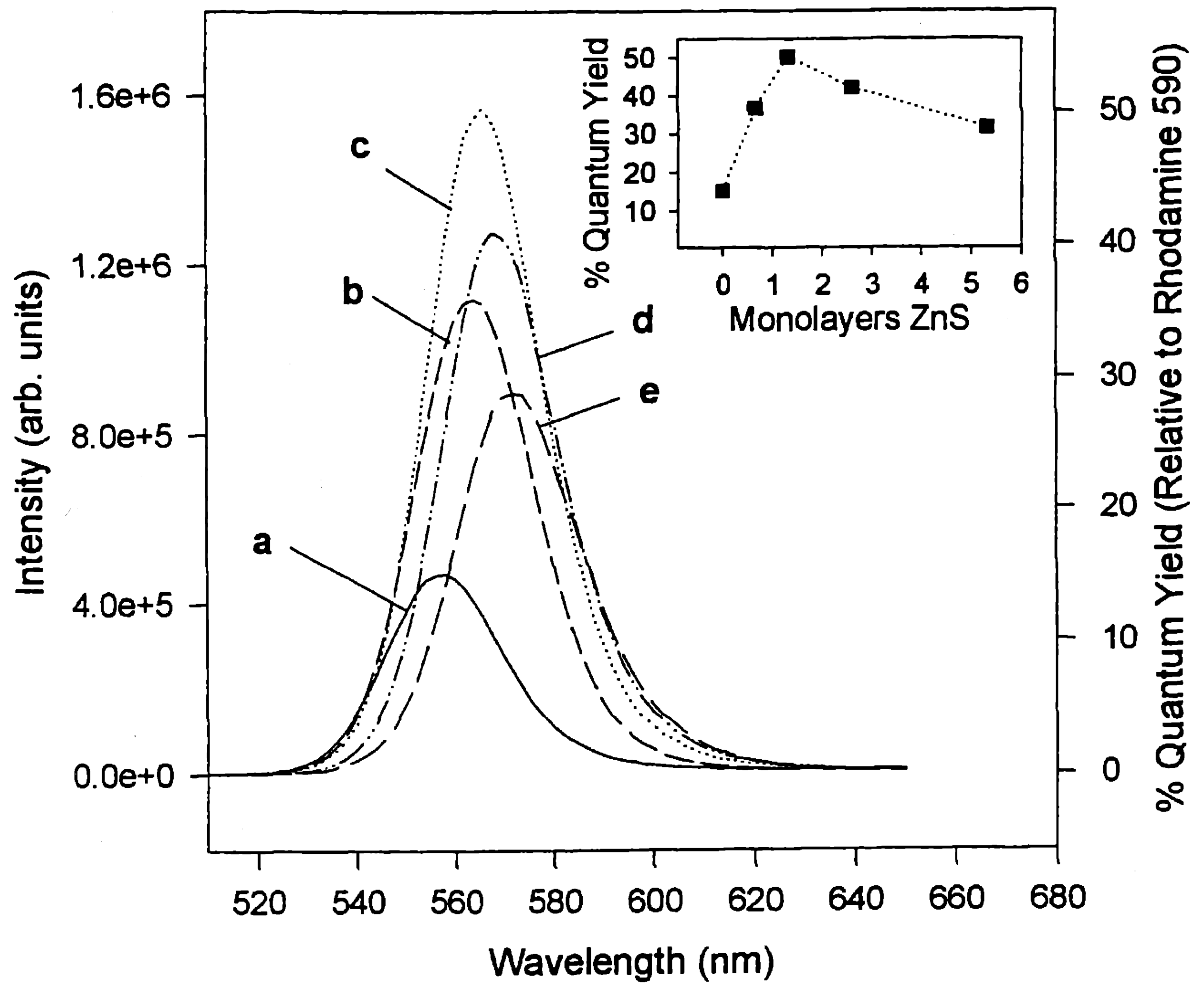

Figure 2.3 PL spectra for a series of ZnS overcoated dots with 42 ±10% Å diameter CdSe cores. The spectra are for (a) 0 monolayers, (b) 0.65 monolayers, (c) 1.3 monolayers, (d) 2.6 monolayers, and (e) 5.3 monolayers ZnS coverage. The position of the maximum in the PL spectrum shifts to the red and the spectrum broadens with increasing ZnS coverage. (Inset) The PL quantum yield is charted as a function of ZnS coverage. The PL intensity increases with the addition of ZnS reaching 50% at ~1.3 monolayers and then declines steadily at higher coverages. The line is simply a guide to the eye.

at about ~5 monolayer coverage. In the following sections we explain the trends in PL quantum yield based on the structural characterization of ZnS overcoated samples.

2.3.3 Structural Characterization

Wide Angle X-Ray Scattering

WAXS probes the internal structure of (CdSe)ZnS and provides information about the lattice parameters of the core and shell. To simulate the experimental data we use a discrete form of the Debye Equation,[13,15]

$$I(q) = I_0 \cdot \left(\frac{f^2(q)}{q} \right) \cdot \sum_k \frac{\rho(r_k)}{r_k} \cdot sin(qr_k) \qquad (1)$$

where I_0 is the incident intensity, f(q) is the angle dependent scattering factor and q=[4π sinθ/λ], where θ is the angle of reflection and λ is the wavelength of the x-rays, $\rho(r_k)$ is the number of times a given distance r_k occurs and the sum is over all interatomic distances. The position of the atoms in both the CdSe core and the ZnS shell are systematically generated in the wurtzite structure and only those atoms falling inside the outlined ellipsoids are used for the simulation. The dimensions of the ellipsoids were taken from TEM measurements. Figure 2.4 displays diffraction patterns for ~40 Å diameter CdSe particles overcoated with different amounts of ZnS as indicated previously. The experimental WAXS patterns of the composite

dots (solid circles) consist of rather broad features that do not match with the bulk wurtzite CdSe or wurtzite ZnS lines. Spectrum (a) corresponds to the bare CdSe nanocrystals used as nucleation centers for the ZnS growth. The first broad feature is a convolution of the (100), (002) and (101) reflections, and is indicative of the finite size of

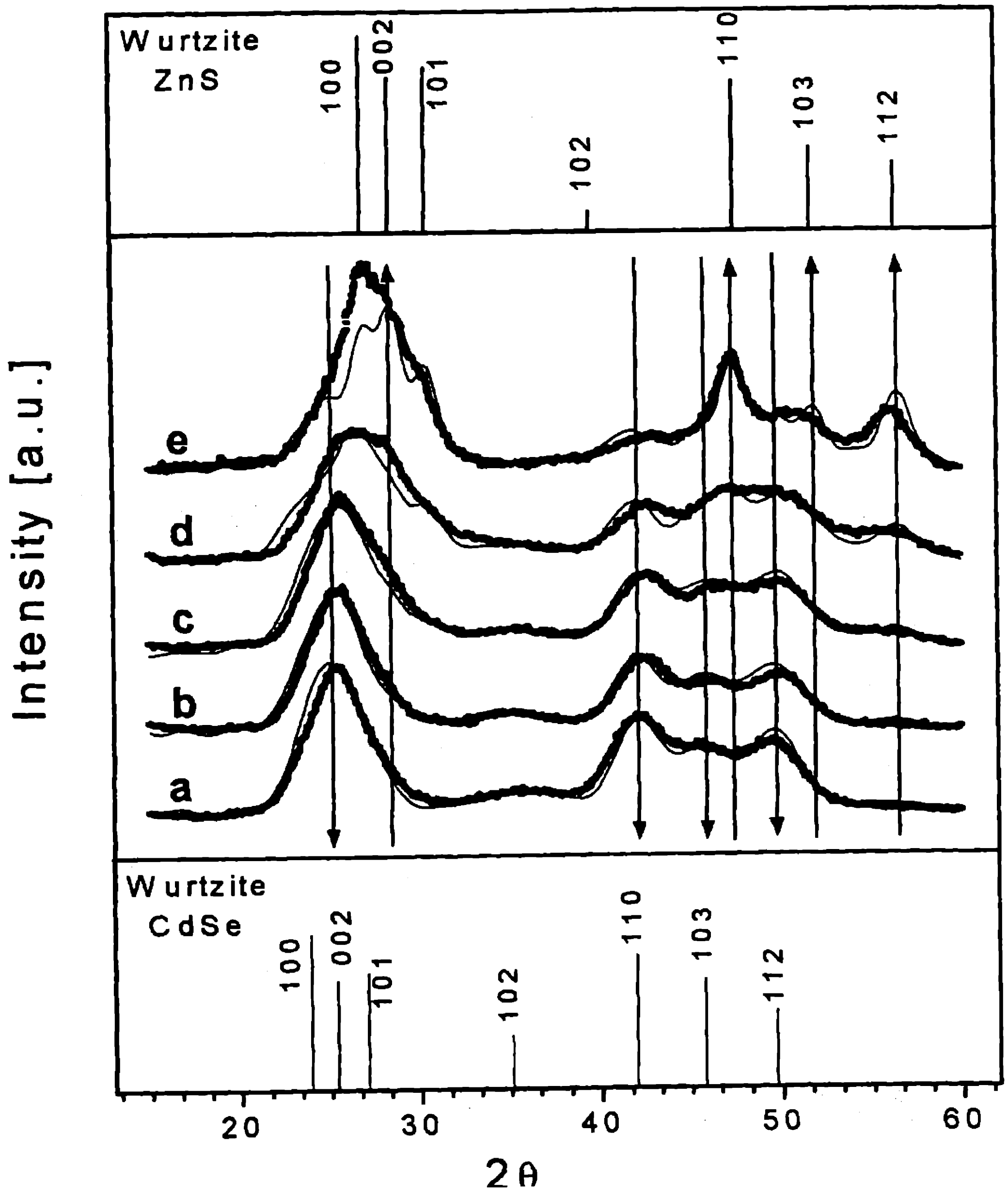

Figure 2.4 WAXS patterns for (a) ~ 40 Å diameter bare CdSe nanocrystals and ZnS overcoated samples with coverages of (b) 0.65 monolayers, (c) 1.3 monolayers, (d) 2.6 monolayers, and (e) 5.3 monolayers. Circles represent the experimental data while solid lines show the fits to the ellipsoidal model detailed in the text. The Zn/Cd ratios used in the simulations are comparable to the WDS measurements. The powder patterns for wurtzite CdSe and ZnS are shown for comparison in the bottom and top insets respectively.

the sample. The decrease in the intensity of the (102) and (103) peaks compared to the powder pattern of the bulk material, is caused by the presence of stacking faults along the [002] direction.[13] The x-ray diffraction patterns of composite nanocrystals with ZnS coverages ranging from (b) 0.65 monolayers to (e) 5.3 monolayers show a strong influence of the ZnS shell on the overall diffraction pattern. The solid lines in spectra (a-e) correspond to the calculated powder patterns. Again we use Eq. (1) to simulate the wide angle region ($15<\theta<60^{\circ}$). The simulation includes the effects of stacking fault density, thermal fluctuations, aspect ratio and size distribution.[13]

The experimental pattern of the bare dots is simulated using an average stacking fault density of 1.4 per crystallite and prolate particles containing ~1200 atoms with an aspect ratio of 1.1. These parameters are kept constant for the CdSe core in all other simulations. The following features can be outlined from Figure 2.4: a broadening and shift to higher angles of the first convolution feature initially located around 26°, a decrease in the intensity of the (102) CdSe line at 36°, a change in the position and relative intensities of the three peaks around 47°, and at high ZnS coverage (spectra d,e) the appearance of a new peak at 56°.

A glance at the powder patterns for wurtzite CdSe and ZnS (bottom and top insets in Figure 2.4) shows that the x-ray patterns of the composite particles may be fit by adding the weighted contributions to the scattering from both structures. To understand the structure of the composite particles we perform detailed simulations probing the effect of the ZnS shell on the WAXS patterns. The scattering factors of ZnS are smaller than those of CdSe leading to weaker contributions to the overall x-ray spectrum. We estimate that the integrated area of the first convolution feature in ZnS is a factor of 3 smaller than for CdSe. Thus, the presence of large amounts of ZnS is necessary to resolve its structure in the x-ray pattern, as is the case for the samples with 2.6 and 5.3 monolayers ZnS (Figure 2.4(d,e)). All the features mentioned above can be simulated by introducing ZnS shells of different thickness on the CdSe core. However, to obtain reasonable agreement between experimental and simulated patterns the lattice parameters of both structures must be set to their respective bulk values, $a_{CdSe} = 4.29$ Å and $a_{ZnS} =$

3.82 Å. In the case of samples with small coverage of ZnS (Figure 2.4(b,c)) the choice for the lattice parameter of ZnS had little effect on the fits to the x-ray scattering patterns.

Average size measurements and shape determinations from TEM define the dimensions of the ellipsoids in the simulations. While the aspect ratio for CdSe is 1.15, the value for the ZnS shell is weighted between 1.2 to 1.4 based on TEM measurements. At larger coverages most of the particles are elongated along the [002] axis and therefore the distribution of shapes is weighted towards the larger numbers.[1]

An interesting point revealed by the simulations is the presence of stacking faults (SF) along the [002] direction in the ZnS overlayer. The importance of the SF density is apparent in the simulated spectrum for the sample with the highest Zn/Cd ratio. The best fit occurs when an average of 3 SF per crystallite is included in the ZnS shell. Note that to fit the other spectra there is no need to include stacking faults because the thickness of the ZnS shell is at most 1-2.5 monolayers and its contribution to the overall x-ray signal is small. [Zn/Cd] ratios of 0.7, 1.4, 2.9 and 6.8 were used to obtain the best fits. These values are close to those obtained by WDS[1], supporting the validity of our simulations. The difference in the first broad diffraction peak between simulated and experimental profiles in spectrum (e) of Figure 2.4 suggests a possible change in orientation between the core and overlayer. However, rotating the overlayer to match the (100) planes of the ZnS structure to the (101) planes of the CdSe nanocrystal, did not improve the fit significantly.

One added problem comes from the difference in lattice parameters between the two materials which affects the matching of the interfaces. The summation in Eq. (1) has to be performed over all the distances and consequently it may take into account interactions among all the atoms in the composite structure, whether or not they belong to the same phase, provided that the atoms are not too far away from each other. Thus, the atomic positions at the interface may need to be modeled accurately. To determine the importance of this interaction on the x-ray profiles we carried out simulations with and without interactions between CdSe and ZnS. In the case of no interaction one only needs to add the x-ray scattering factors from the ZnS shell to the factors for the CdSe core. In the other case, the cross terms (I_{CdS},I_{ZnSe},I_{SSe},I_{CdZn}) in Eq. (2) need to be considered. Although small modifications exist in the x-ray pattern (mainly in the first diffraction feature) the difference between the non-interacting and the interacting case is much less significant than the effect of changing the Zn/Cd ratio, the aspect ratio or the stacking fault density in the patterns.

2.4 Discussion

After successfully producing (CdSe)ZnS dots with a wide range of core sizes, we focus our attention on one particular sample of CdSe seeds and study the evolution of the optical and structural properties as a function of ZnS coverage. We first use a simplified theoretical approach to model the shifts in energy with increasing shell thickness for CdSe dots overcoated with different amounts of ZnS or CdS. We then proceed to analyze the structure of (CdSe)ZnS composite dots with varying amounts of ZnS in order to determine how the structure of these dots influences their fluorescence. Finally, we attempt to characterize the growth mechanism for the ZnS shell onto the CdSe core.

2.4.1 Theoretical Modeling of the Electronic Structure

We use a simplified model of non-interacting particles in a spherical box to describe the electron and hole wavefunctions and confinement energies inside the composite quantum dots.[3,16,17] The Coulomb attraction between the electron and hole is added as a first order perturbation term in the Hamiltonian. We assume the dots consist of a spherical CdSe core surrounded by a concentric shell of ZnS and that there is no alloying at the interface. We assign a potential energy of zero inside the CdSe core and a barrier height of 0.9eV for both the electron and hole to tunnel into the ZnS shell.[18] In this picture the electron (hole) must tunnel through a 4eV (10eV) barrier to extend into the surrounding organic matrix. The wavefunctions in the CdSe core are the product of an angular part, spherical harmonics $Y_{l,m}(\theta,\varphi)$, and a radial part, which is a linear combination of spherical Bessel functions, $j_{n,l}\ (k\cdot r)$, and spherical Neumann functions, $n_{n,l}(k\cdot r)$. The wavefunctions in the ZnS shell decay exponentially. We obtain the exact solutions to the radial Equation for the composite particles by solving the continuity relations for the electron and hole wave functions, Eq. (2), and the probability currents, Eq. (3), at the CdSe/ZnS interface:

$$R_{1S,CdSe}(k_1 \cdot r_1) = R_{1S,ZnS}(\kappa_2 \cdot r_1) \tag{2}$$

$$\frac{1}{m^*_{CdSe}} \cdot \frac{d}{dr} R_{1S,CdSe}(k_1 \cdot r)\Big|_{r=r_1} = \frac{1}{m^*_{ZnS}} \cdot \frac{d}{dr} R_{1S,ZnS}(\kappa_2 \cdot r)\Big|_{r=r_1} \tag{3}$$

where $R_{1S,CdSe}$ and $R_{1S,ZnS}$ are the lowest energy radial wavefunctions for the electron or hole in the CdSe core and ZnS shell respectively, r_1 is the radius of the CdSe core, m^*_{CdSe} and m^*_{ZnS} represent the hole or electron bulk effective masses in CdSe and ZnS respectively, and k_1 and κ_2 are the wavevectors in CdSe and ZnS respectively.

Figure 2.5 shows the radial probabilities of the electron and hole in the lowest energy $1S_{3/2}$-$1S_e$ eigenstates for bare (TOPO capped) ~20 Å radius CdSe dots (a) and for the same dots with a 4 Å ZnS (b) or 4 Å CdS (c) shell. In the bare dots the wavefunction of the lighter electron spreads over the entire particle and tunnels only slightly into the surrounding organic matrix whereas the heavier hole has a higher probability at the center of the dot and does not extend into the surrounding matrix. When a shell of ZnS surrounds the CdSe particle the electron wavefunction tunnels into the ZnS shell while the hole wavefunction has a negligible probability of spreading into the ZnS layer. The increased delocalization of the electron lowers its confinement energy and consequently the energy of the excited state. Beyond a certain thickness of the ZnS shell the electron and hole wavefunctions cannot spread out further and the confinement energies remain constant.

In CdS the barrier height for the electron (0.2 eV) is smaller than the total energy of the electron and thus its wavefunction extends well into the CdS shell. The hole, however, must tunnel through a 0.55eV barrier into the CdS shell and therefore has lower probability of penetrating into the surrounding CdS matrix than the electron but extends into the CdS more than it does for a ZnS shell.

We estimate the energy shift as a function of ZnS shell thickness for a series of samples grown on ~20 Å radius CdSe dots. Figure 2.6 shows the experimental measurements (solid circles) of the difference in energy for the lowest energy $1S_{3/2}$-$1S_e$ transition between bare and ZnS overcoated dots as a function of the ZnS shell thickness.

The solid line represents the calculated values using a 4eV barrier for the electron to tunnel into the organic matrix and a

10eV barrier for the hole. These values generated the best fit to the experimental data but should not be taken literally since they are essentially fitting parameters which in addition to modeling the real difference in band offsets, also account for general deficiencies in this simplified model. The solid squares show the difference in energy between the PL peaks (excitation at 450 nm) for bare and overcoated samples. The dashed line represents the calculated values for the shift in PL vs. shell thickness. The shifts in PL are larger than the shifts in absorption with the discrepancy increasing at higher ZnS coverages. Most of the increase in the shift can be accounted for by the increased size distribution in the samples with higher coverage. A partial dependence of the non-resonant Stokes shift on the size distribution has already been demonstrated for bare (organically passivated) CdSe dots.[19] The increased shift is the result of preferential absorption into the largest dots in the size distribution at the excitation wavelength (100 nm to the blue of the first absorption feature) leading to a larger red-shift for broader size distributions.[20] The experimental values for the shifts in absorption and PL appear to be in agreement with the values obtained by simple theoretical modeling.

Figure 2.7 shows the energy difference between bare and CdS overcoated ~ 30 Å radius CdSe dots as a function of CdS shell thickness. The shift in the exciton energy as a function of CdS coverage is much larger than it was in the case of ZnS. This effect is not surprising since the introduction of a CdS shell lowers the electron confinement energies to a greater extent than in the ZnS shell. The measured values are shown as solid circles with the error bars reflecting the size distributions from TEM. The calculated values for the shifts are represented by the solid line.

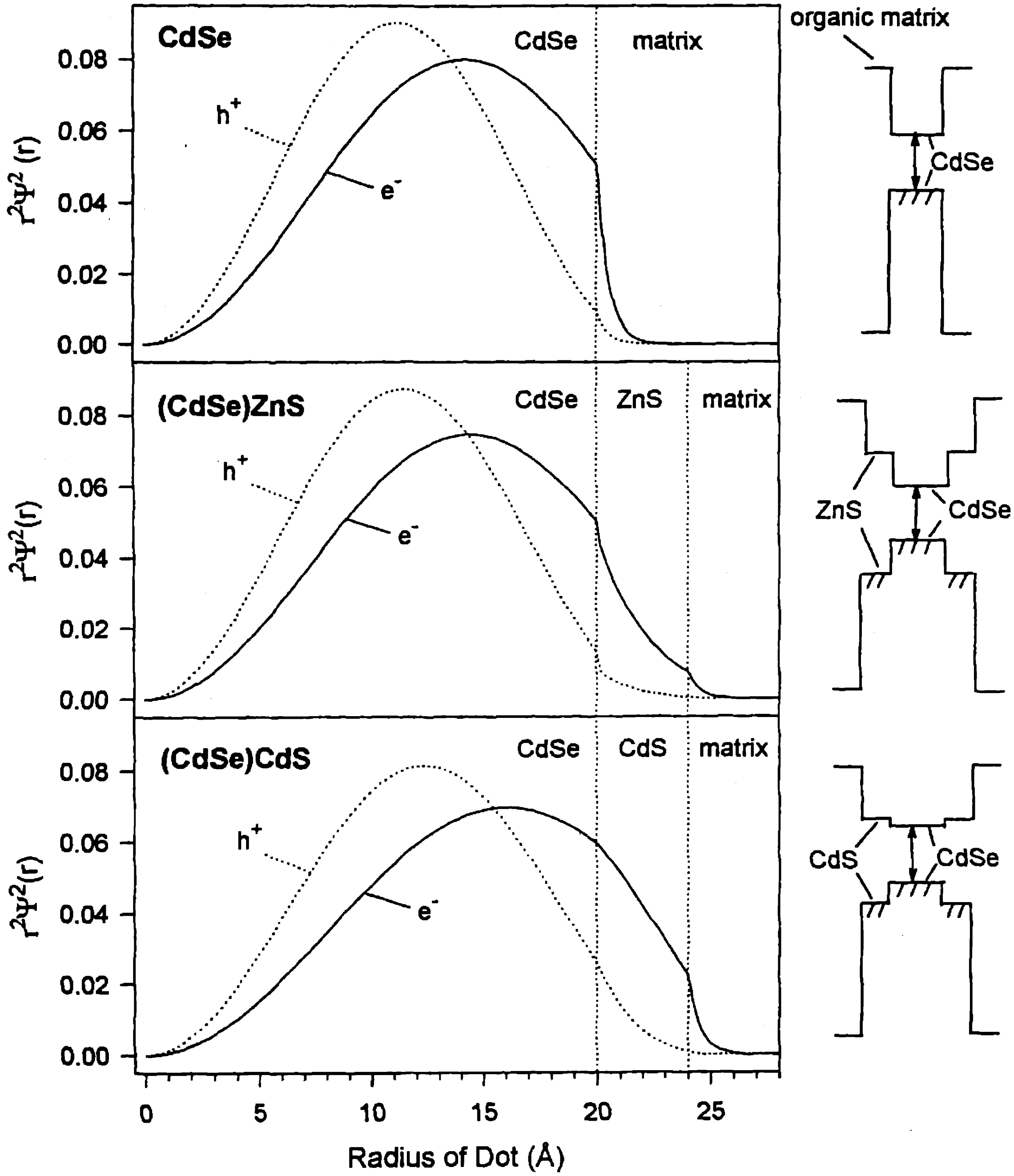

Figure 2.5 Radial probability functions for the lowest energy ($1S_{3/2}$-$1S_e$) electron and hole wavefunctions in (A) bare 20 Å diameter CdSe dots, (B) (CdSe)ZnS dots with a 20 Å diameter core and a 4 Å ZnS shell, and (C) (CdSe)CdS dots with an identical core and a 4 Å CdS shell. The sketches to the right show the approximate band offsets between the various components.

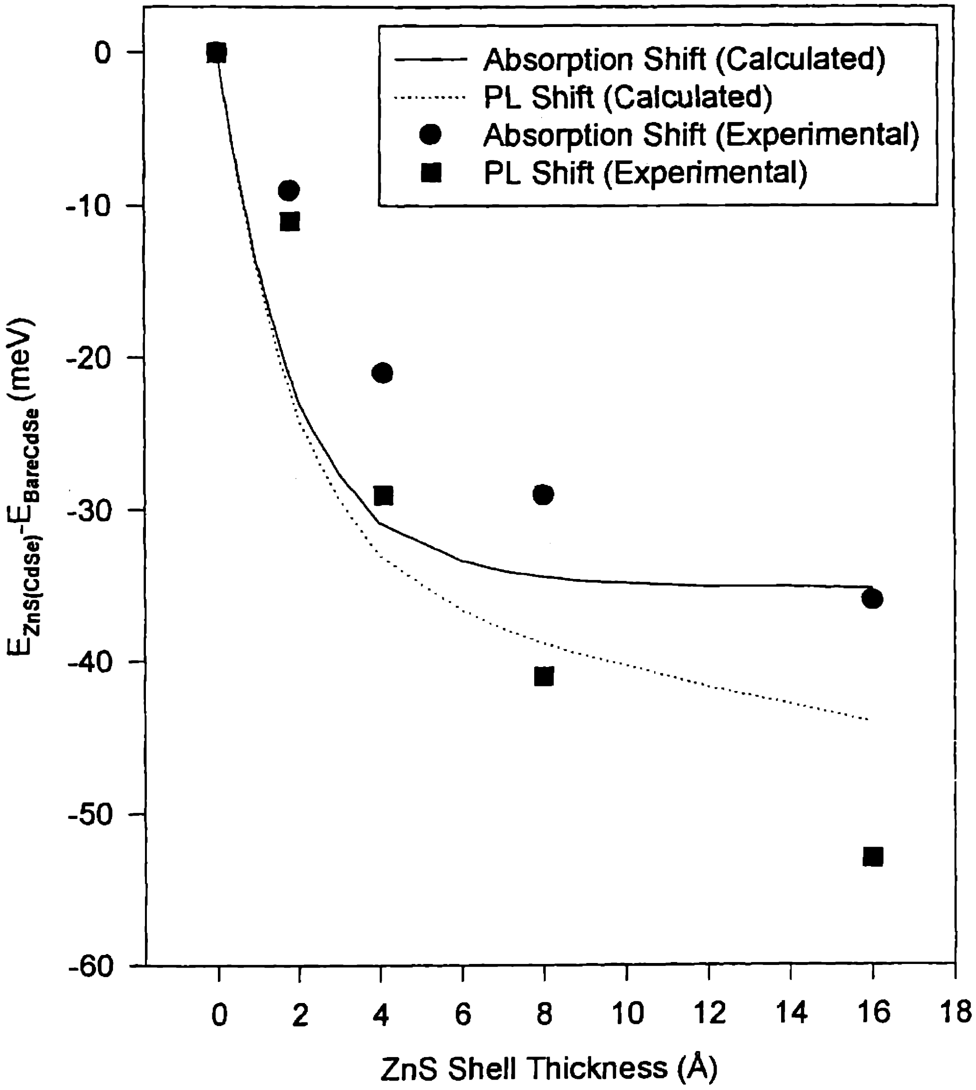

Figure 2.6 Energy difference between bare ~20 Å radius CdSe and (CdSe)ZnS particles as a function of ZnS shell thickness. The experimentally measured shifts in the first absorption feature appear as solid circles. The shifts in PL appear as solid squares. The calculated energy shifts for the absorption are plotted (solid line) vs. shell thickness. The calculated shifts in the positions of the PL peaks are represented by the dashed lines.

The largest shift in the first absorption feature for ~ 20 Å radius dots obtained for a 16 Å thick shell of ZnS is approximately 36 meV. The shift for a 16 Å shell of CdSe on top of the same ~ 20 Å radius particles would be almost an order of magnitude higher (290 meV). In the CdS overcoated particles the shift for a 15 Å shell of CdS deposited onto ~ 16 Å radius CdSe dots was ~ 210 meV. Depositing a 15 Å shell of CdSe onto these same particles instead of CdS would result in a ~ 390 meV shift.

2.4.2 Characterization of ZnS Shell and its Influence on PL Quantum Yield

Table I summarizes the structural information obtained from WDS, TEM, SAXS and WAXS which includes values for the average size, size distribution and Zn/Cd ratios obtained for the series of (CdSe)ZnS samples with a ~ 40 Å diameter core. The close agreement among the different methods lends credibility to the analysis and allows us to describe the structure of the composite dots with greater confidence.

Referring back to the inset of Fig. 5, two important features stand out: a maximum efficiency of 50% at ~1.3 monolayer coverage and a steady decrease in the quantum yield beyond that point with increasing ZnS coverage.

The first feature is explained by the results of XPS analysis which suggests that QDs with 1.3 monolayers of ZnS no longer oxidize upon exposure to air, which means that the majority of surface Se sites are passivated by an inorganic ZnS shell. The PL quantum yield reaches its maximum value at this same coverage indicating that most of the surface vacancies and non-radiative recombination sites are passivated.

We now focus our attention on understanding the growth of thicker ZnS shells and how that leads to a decline in the PL quantum yield. Detailed structural analysis via TEM on the higher coverage ZnS overcoated dots reveals slightly non-uniform growth of the ZnS shell and preferential growth in the [002] wurtzite direction of the CdSe core. This results in slightly elongated and in some cases irregularly shaped dots. These samples are also much more prone to irreversible flocculation than dots with lower ZnS coverage indicating poor coordination of the TOPO capping groups to the surface Zn atoms.

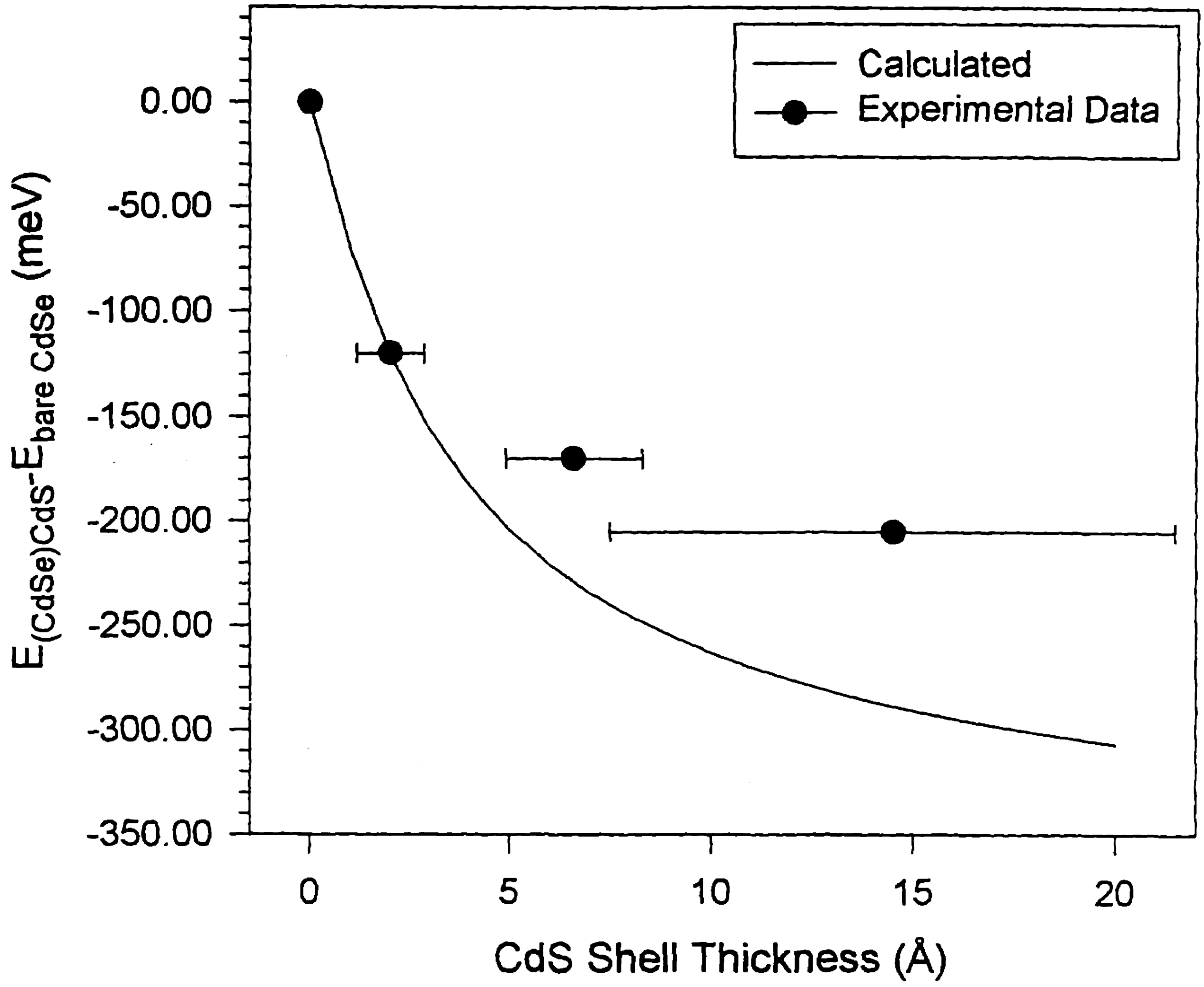

Figure 2.7 Energy difference between bare ~16 Å radius CdSe and (CdSe)CdS particles as a function of the CdS shell thickness. The experimental data appear as solid circles with error bars representing the size distribution obtained from TEM measurements. The estimated energy shifts for these particles assuming a 4eV (10eV) barrier for the electron (hole) to tunnel into the surrounding CdS matrix are shown for comparison (solid line).

In order to simulate the WAXS patterns for the highest coverage of ZnS on the CdSe cores it was necessary to use the bulk lattice parameters for CdSe and ZnS. Furthermore, we included on average three stacking faults per crystallite along the [002] direction in the ZnS shell to fit the experimental profiles. The presence of stacking faults along the [002] direction in these types of structures is due to their low energy of formation,[21] leading to preferential growth along that direction. This results in elongated particles with aspect ratios close to 1.3 and 1.4 as determined from TEM and SAXS. Defects in the ZnS shell may be the source of new non-radiative recombination sites and thus lead to a decline in the quantum yield of composite particles with thick ZnS shells.

Finally, we speculate as to the mechanism by which ZnS grows on top of the existing CdSe seed particles and how the growth affects the PL quantum yield at higher coverages. Excluding the presence of separate ZnS particles, the growth of ZnS on the CdSe nanocrystals may occur in one of three ways: incoherent epitaxial growth of the overlayer on the CdSe surface (with dislocations); coherent epitaxial growth with large distortion or strain; or the formation of a highly disordered shell.

The presence of a highly disordered ZnS shell can be eliminated because the x-ray diffraction peaks clearly originate from a crystalline structure. The other two possibilities are more difficult to differentiate. The initial growth of ZnS on the surface of CdSe is hard to characterize from the data available. The WAXS patterns for the low coverage samples are dominated by scattering from the heavier Cd and Se and very little information can be derived from the ZnS shell. However, at a coverage higher than ~2 monolayers the ZnS shell grows with the bulk lattice parameter indicating an incoherent growth. WAXS patterns clearly show that the ZnS shell has its own lattice parameter, but simulated spectra were insensitive to the orientation of the shell. The nanocrystallites examined using TEM appear to have an epitaxial ZnS shell, but the resolution was not sufficient to measure a difference between the core and the shell. Using the information from these two techniques, we describe the thicker overlayers as epitaxial but incoherent.

Regarding the actual mechanism of ZnS shell growth, there are two likely scenarios. The first and most likely possibility is that the growth could initially be coherent at low coverage but as the thickness of the shell increases, the strain due to the lattice mismatch (12%) between CdSe and ZnS could lead to the formation of dislocations and low-angle grain boundaries, relaxing the structure and causing the growth to proceed incoherently. These defects could be the source of non-radiative recombination sites within the ZnS overlayer. This behavior has already been reported for ultrathin CdSe/ZnSe quantum wells where the lattice misfit between subsequent layers is only 7%.[22] In this case, the reduction in the PL intensity was attributed to the generation of misfit dislocations when the thickness of the CdSe layer exceeded 4 monolayers.

Another possibility is that the growth begins with a large density of nucleation sites producing many, small island-like clusters of ZnS which are locally coherent with the core. These islands then coalesce as the thickness of the shell increases to form a continuous film on the CdSe surface with a structure that has relaxed at the outer boundary to that of bulk ZnS. The formation of grain boundaries as the islands coalesce could then be the origin of non-radiative recombination sites. In either case, particles with very high ZnS coverage would have the bulk ZnS lattice parameter and their quantum yield would decrease with increasing ZnS coverage as is observed in these samples.

2.5 Conclusion

A synthetic procedure for the production of core-shell quantum dots whose emission spans most of the visible spectrum is described. WAXS is used to probe the internal structure of the dots and indicates that at very high coverage the ZnS shell retains its bulk lattice parameter.

The influence of surface passivation on the optical properties is also evaluated. We explain the shift in the absorption using a simple theory treating the charge carriers as particles in a spherical box. We find that the quantum yield of ZnS overcoated samples reaches a maximum value shortly after ~1.3 monolayers of ZnS are added. At this coverage XPS measurements indicate that most of the surface Se sites are coordinated. The decrease in quantum yield at higher coverages is attributed to the formation of defects in the ZnS shell.

2.6 References

[1] B. O. Dabousi, J. Rodriguez-Viejo, F. V. Mikulec, J. R. Heine, H. Mattoussi, R. Ober, K. F. Jensen, and M. G. Bawendi, J. Phys Chem. B 101 (1997) 9463.

[2] Tian, Y.; Newton, T.; Kotov, N. A.; Guldi; D. M. and Fendler, J. *J. Chem. Phys*. **1996**, 100, 8927.

[3] Youn, H.C.; Baral, S.; Fendler, J.H. *J. Phys. Chem*. **1988**, 92, 6320.

[4] Kortan, A.R.; Hull, R.; Opila, R.L.; Bawendi, M.G.; Steigerwald, M.L., Carroll, P.J.; Brus, L.E. *J. Am. Chem. Soc*. **1990**, 112, 1327.

[5] Mews, A.; Eychmuller, A.; Giersig, M.; Schooss, D.; Weller, H. *J. Phys. Chem*. **1994**, 98, 934.

[6] Danek, M.; Jensen, K.F., Murray, C.B.; Bawendi, M.G. *Chem. Mater*. **1996**, 8, 173.

[7] Littau, K.A.; Szajowski, P.J.; Muller, A.J.; Kortan, A.R.; Brus, L.E. *J. Phys. Chem*. **1993**, 97, 1224.

[8] Wilson, W.L.; Szajowski, P.J.; Brus, L.E. *Science* **1993**, 262, 1242.

[9] Hines, M.A.; Guyot-Sionnest, P. *J. Phys. Chem*. **1996**, 100, 468.

[10] Mattoussi H, Radzilowski LH, Dabbousi BO, Fogg DE, Schrock RR, Thomas EL, Rubner MF, Bawendi MG, J. Appl. Phys. **86** (1999) 4390.

[11] Mattoussi H, Radzilowski LH, Dabbousi BO, Thomas EL, Bawendi MG, Rubner MF, J. Appl. Phys. **83** (1998) 7965.

[12] RodriguezViejo J, Jensen KF, Mattoussi H, Michel J, Dabbousi BO, Bawendi MG, Appl. Phys. Lett. **70** (1997) 2132.

[13] Murray, C.B.; Norris, D.J.; and Bawendi, M.G. *J. Am. Chem. Soc*. **1993**, 115, 8706.

[14] The temperatures at which each individual size of dots was overcoated are as follows: 23 Å diam. (140 °C), 30 Å diam. (140 °C), 35 Å diam. (160 °C), 40 Å diam. (180 °C), 48 Å diam. (200 °C), 55 Å diam. (220 °C).

[15] Murray, C.B PhD thesis, Massachusetts Institute of Technology, **1996**.

[16] Haus, J.W.; Zhou, H.S.; Homma, I.;Komiyama, H. *Phys. Rev. B* **1993**, 47, 1359.

[17] Schooss, D.; Mews, A.; Eychmuller, A.; Weller, H. *Phys. Rev. B* **1994**, 49, 49.

[18] Nethercot, A.H. *Phys. Rev. Lett*. **1974**, 33, 1088.

[19] Kuno, M.; Lee, J.K.; Dabbousi, B.O.; Mikulec, F.V.; and Bawendi, M.G. *J. Chem. Phys*. **105** (1997) 9869.

[20] We obtain an effective size distribution for the ZnS overcoated dots based on their absorption linewidths by relating this linewidth to a size distribution of bare CdSe dots. To account for the size preference of the absorption into the larger particles we convolute the PL peak with the cube of the effective radius (a^3) since the density of states is proportional to the volume of the dots. This results in a larger red-shift of the PL with increasing effective size distribution as observed experimentally.

[21] Aven, M.; Prener, J.S. *Physics and Chemistry of II-VI Compounds*; North Holland, Amsterdam, **1967**, pp. 144.

[22] Zajicek, H.; Juza, P.; Abramof, E.; Pankratov. O.; Sitter, H.; Helm, H.; Brunthaler, G.; Faschinger, W.; Lischka, K. *Appl. Phys.Lett*. **1993**, 62, 717.

Chapter 3

Synthesis of Mixed Color LEDs and Monte Carlo Simulation of Light Generation and Propagation in a Quantum Dot - Containing Transparent Medium

3.1 Color Theory and Mixed Color LEDs

Full color luminescent displays typically emit light at red, green and blue (RGB) wavelengths. Mixing of these three colors enables the generation of any color desired. This is described quantitatively by the Commission Internationale de L'Eclairage (CIE) Chromaticity Diagram.[1] The chromaticity diagram maps out the colors perceived by the eye when stimulated by light of given wavelengths and relative intensities. The points on the outer envelope of the diagram correspond to monochromatic light, which produces saturated colors. Points in the interior of the diagram are colors that are produced by mixing light from saturated color sources. In fact, the CIE diagram can be used in much the same way as a phase diagram, with mixed colors lying on a line connecting two saturated colors, being mixtures of those two colors. For example, light with CIE coordinates X = Y = 1/3 corresponds to white light. White light can be generated using red, green, and blue light sources, near the corners of the CIE diagram, or with blue and yellow light sources, which appear on opposite sides of (1/3, 1/3) on the CIE diagram. For a full-color display system, the best light emitting materials should produce light near the corners (RGB) of the diagram so as to have the largest color gamut possible.

Light emitting diodes (LEDs) are used in a wide variety of applications that require small, but bright luminescence sources. However, the light output of an LED is monochromatic because the color of the light emitted is set by the bandgap of the semiconducting material in the LED active region. Thus, producing different colors requires using different semiconductor materials; from InGaN, to generate blue, to AlGaAs, to generate red. Closely spaced monochromatic LEDs are used to produce the effect of mixed colors in large displays. However, there is a large market for single source white (and other unsaturated color) devices. Single source LED-based devices emitting white light use a monochromatic LED to excite a phosphor, such as an organic dye or π-conjugated polymer,[2,3] which emits its own color, which adds to that of the original light source creating a mixed color.

In this work (CdSe)ZnS quantum dots (QDs) rather than an organic dye are used as the phosphor. As shown in the previous chapter, nearly the entire visible spectrum, from blue to red, can be produced by (CdSe)ZnS quantum dots with CdSe core radii ranging from 12.5 Å (blue) to 40 Å (red). Furthermore, these QDs exhibit high photoluminescent efficiencies of 30% to 50%. Work done to create a high brightness QD-polymer composite will be described below. J. Lee, et. al.[4] demonstrated that polylaurylmethacrylate (PLMA) is an excellent host medium for the quantum dots and have produced an optically clear, photoluminescent QD-polymer composite. By controlling the size and spatial distribution of the quantum dots in the material, the color produced can be specifically tailored. This material can be placed at the end of a blue LED to create a mixed color LED.

3.2 Embedding Quantum Dots in Polymer

Bare CdSe quantum dots have been embedded in polyvinylcarbazole[5] and poly(vinyl butyral) (PVB)[6], and (CdSe)ZnS quantum dots have been embedded in a phosphine functionalized diblock copolymer [methyltetracyclododecene]$_{300}$-[norbornene-$CH_2O(CH_2)_5P(oct)_2$]$_{20}$, and PVB.[7] In all cases the quantum dots and polymer were first dissolved in a solvent to create a quantum dot – polymer solution. The solvent was then removed by evaporation. In attempts to produce a high brightness polymer-QD composite several polymers, and techniques for dispersing quantum dots within them, were tried.

3.2.1 Poly(vinyl butyral)

Early attempts to create large (3-4 mm thick, 4-5 mm wide polymer caps for blue diodes used a similar technique. Different sizes of (CdSe)ZnS quantum dots, with absorption maxima from 500nm to 600nm, were dispersed in toluene. PVB was then added and the solvent removed by evaporation. A large drop in luminescence was detected by eye. Adding small amounts of tri-n-octylphosphine (TOP) or tri-n-octylphosphine oxide (TOPO) to the solution to provide better capping increased the luminescence in solution but yielded a low brightness polymer – quantum dot solution after drying. Furthermore, solutions containing both green and red quantum dots (in an attempt to make white light) exhibited yellow emission to the eye before drying. After drying, however, the red emission dominated, suggesting agglomeration of the quantum dots and subsequent energy transfer from the green QDs to the red ones,[6,8] or possibly, enhanced degradation of the green QD luminescence due to the greater surface to volume ratio.

3.2.2 Poly(4-vinyl pyridine)

To avoid the use of TOP/TOPO to coordinate the surface of the quantum dots, I attempted to disperse them in poly(4-vinyl pyridine) (PVP). QDs with absorption maximum of 614 nm were cap-exchanged with pyridine by dispersing them in and precipitating them out of pyridine solution several times. The pyridine was then evaporated under vacuum leaving a dry QD powder. This powder was brought into a glove box and dispersed in 4-vinyl pyridine. The solution was polymerized with the aid of <1% concentration 1,1'-azobis(cyclohexanecarbonitrile), which acted as an initiator, and heating (on hot plate with low temperature setting). About one minute after beginning heating, rapid bubbling began and the polymer solution polymerized within several seconds. The polymer luminescence was moderately bright. Further experiments showed that with high concentrations of initiator (50 mg initiator / 1 mL monomer) polymerization was rapid (~5minutes) with vigorous bubbling. The final product was a hard, frothy, luminescent polymer. Decreasing the initiator concentration by one half reduced the rate of bubbling but increased the polymerization time to greater than 10 minutes. The increased heating time led to the degradation of QD luminescence. Reducing initiator concentration (10 mg/mL) and/or polymerization temperature (by heating in an oil bath) led to much longer polymerization times and, frequently, incomplete polymerization. To form the QD-polymer into a cap while maintaining relatively high brightness, I attempted to dissolve the polymerized QD-PVP frothy solid and then cast it into a mold hoping that the PVP would remain coordinated to the QD surface and would prevent luminescence degradation. Both pyridine and chloroform were found to dissolve the polymer, but with a decrease in the luminescence.

3.2.3 Amino-terminated polystyrene

Neither PVB nor pyridine bind very well to the QD surface which leads to a significant drop in the luminescence efficiency of the QD since defect states at the QD surface are not passivated well. The high luminescence efficiencies found when the QDs are coordinated by TOP or TOPO suggests that a polymer with a phosphine or an amine functionality would tend to bind to the surface of the QD and passivate deep trap states that are present there. CdSe QDs have been shown to be soluble in amino-terminated polystyrene, and will segregate into the polystyrene when added to a block copolymer system.[9] Amino-terminated polystyrene (molecular weight ~2000) (PS) and (CdSe)ZnS QDs were both dissolved in toluene. The resulting QD-polymer material left after allowing the solvent to evaporate away was analyzed.

For example, a 250 mg/mL solution of PS in toluene and a solution of 504nm absorption QDs with an optical density (OD) of 140 (for a 1cm path length) in toluene were prepared. Equal volumes (0.1 mL total) of PS and QD solutions were mixed together. The resulting solution was very bright and optically clear.[10] To produce a polymer cap for the blue LED, the solution was placed into the tip of a 5 mm diameter NMR tube. The solvent was evaporated away under vacuum yielding a cloudy yet still bright solid. This cap, when placed over a blue LED, was able to completely absorb the blue light and give a solid green color. Reducing the QD concentration to a point where the solid remained optically clear resulted in a polymer cap which still let through a significant amount of blue light. This is reasonable because the cap produced with the concentrated solution likely had a minimum optical density of 7 to 10 at wavelengths from 450 nm to 475 nm in regions where the polymer was only 1 mm thick. Cutting the concentration in half would allow the blue light to become visible through the green cap. Longer chain (MW = 45,000) non-functionalized polystyrene was added to the solution to help stabilize the QD - short chain PS mixture. Due to the viscosity of the resulting solution it was very difficult to dry the cast polymer cap. Ultimately, the inability to thoroughly dry a bulk polymer cap that is sufficiently thick to enable a low QD concentration solution to absorb all of the blue light prevented success with this polymer.

3.2.4 Polylaurylmethacrylate

To get a good QD-polymer system, the QDs would have to be chemically stable, ideally coordinated with TOPO, or some other phosphine, just as they are after being grown. Furthermore, it should not be necessary to remove any solvent so that large (several mm thick) pieces of polymer can be produced. Ideally, the QDs would be dispersed in a monomer which is subsequently polymerized. Such a system was developed by J. Lee, et al.[4] Quantum dots capped with TOPO are dispersed in a 10:1 solution of lauryl-methacrylate (LMA) and TOP. Ethylene glycol dimethacrylate (EGDMA), which acts as a cross-linker, is then added to the solution to form a 10:2.5:1 solution of LMA:EGDMA:TOP. The initiator, AIBN, is then added and comprises 1% of the final solution. The resulting solution is left to polymerize in air at 60 °C for 1.5 to 2 hours in test tubes. The resulting polymer rods are optically clear and typically have quantum yields of 30%. The TOP, which was added with the LMA, maintains a large supply of capping molecules for the QDs so that they remain chemically passivated during the polymerization process. The polylaurylmethacrylate has a long 12-carbon chain hanging off its backbone which acts as a non-polar structure which attracts the octyl groups of the TOP molecules attached to the QD, thus keeping them soluble in the polymer. This QD-polymer system is used for the LED simulation work described below.

3.3 Monte-Carlo Simulation of Mixed Color LED

To determine the key parameters in designing a luminescent polymer LED cap, we created a Monte – Carlo simulation of light emission from a quantum-dot containing polymer. A blue ray of light from the exciting LED is followed through the polymer, absorbed, emitted at a wavelength chosen from the distribution of wavelengths produced by the quantum dots present at the point of absorption, and the subsequent ray of light is followed through the medium. The amount and wavelengths of light reaching the end are recorded. The resulting luminescence spectrum is then compared with that generated by an actual device. Good agreement is found between simulated and measured spectra. The simulation is then used to calculate the QD-polymer structure needed to create white light, and the resulting LED is produced.

3.3.1 Optical Behavior of Solutions of Quantum Dots

When a large number of QDs are excited, the spectrum of light produced by them is influenced by the wavelength of the exciting light, their size distribution and their concentration. Figure 3.1 plots the photoluminescence produced by green-emitting QDs as the wavelength of the exciting light is increased from 375nm, which is well above the QD band gap and where all QDs absorb (see below), to 500nm, which is the band edge absorption peak maximum. The luminescence peaks are all gaussian in appearance, but shift slightly with exciting wavelength. In particular, there is a significant bias of the peak to the blue, the maximum peak position shifts 5nm to 6nm from the average position of 520nm, when excited in the range of 475nm to 490nm. This range corresponds to the blue side of the first absorption peak, which is shown in Figure 3.2.

This photoluminescent behavior of an ensemble of quantum dots can be understood by considering the physics of a single quantum dot and then considering the effect of the presence of a large ensemble of quantum dots.[11] Here we provide a qualitative analysis. The three dimensional confinement of an exciton within a quantum dot gives rise to discrete energy states somewhat like the discrete states possessed by atoms. Photoluminescence from solitary CdSe and (CdSe)ZnS QDs has a very narrow linewidth (<1.5 meV) which indicates the discreteness of the band edge transition of the QDs.[12] Photoluminescence excitation measurements of bare CdSe QDs have demonstrated the existence of numerous yet separated energy transitions just higher in energy than the band edge transition,[13] providing further evidence for the presence of numerous discrete, energy states for the electron and hole.

However, the transition peaks are not sharp but overlap. Thus a particular QD will absorb to some extent all wavelengths shorter than that for its band edge transition. The broadening of absorption features away from the band gap can be understood by the Heisenberg Uncertainty Principle. Higher energy states have very short lifetimes and therefore have a large uncertainty in transition energy. Measurements have shown sub-picosecond intraband relaxation of the electron[14] and hole[15] from the absorbing state to the emitting state in bare CdSe QDs. Coupled with the decreasing separation of energy states far from the band gap, the QD absorption becomes a continuum for energies 0.5 eV above the band gap. Exciting QDs away from the first absorption peak will excite all of the QDs and give a PL spectrum which is largely invariant to excitation wavelength. This is seen for excitation wavelengths from 375nm to 460nm in Figure 3.1.

Transitions just to the blue of the band edge have a lower absorption cross-section than does the band edge transition. This can be seen with absorption spectra of large ensembles of QDs, such as that shown in Figure 3.2 for green QDs with the first (band edge) absorption peak at 500nm. Also plotted is the shift to the blue the emission peak exhibits when excited by different wavelengths of light relative to 520nm. The largest deviation occurs on the blue side of the first absorption peak. In this wavelength range the smallest QDs are being excited directly at their first (band edge) energy transition which has a relatively high optical cross-section. QDs to the red are only being excited at their second or third transition and therefore do not emit as much light as do the smaller QDs. Hence, there is a bias in the luminescence peak to the blue.

An ensemble of QDs possesses a nearly gaussian size distribution.[7] With QDs emitting in a narrow wavelength range set by their size, the luminescence intensity will qualitatively follow the size distribution. A composite or liquid solution of QDs that has a low concentration of QDs, exhibits a PL peak whose position and FWHM is characteristic of the mean size and standard deviation of the QD size distribution, respectively. The luminescence of the QDs exhibits a Stokes Shift relative to the band edge absorption peak.[11] However, there remains significant overlap between the emission peak and the first absorption peak. This overlap results in the absorption of emitted light by other QDs; larger QDs absorb light produced by smaller QDs and, in

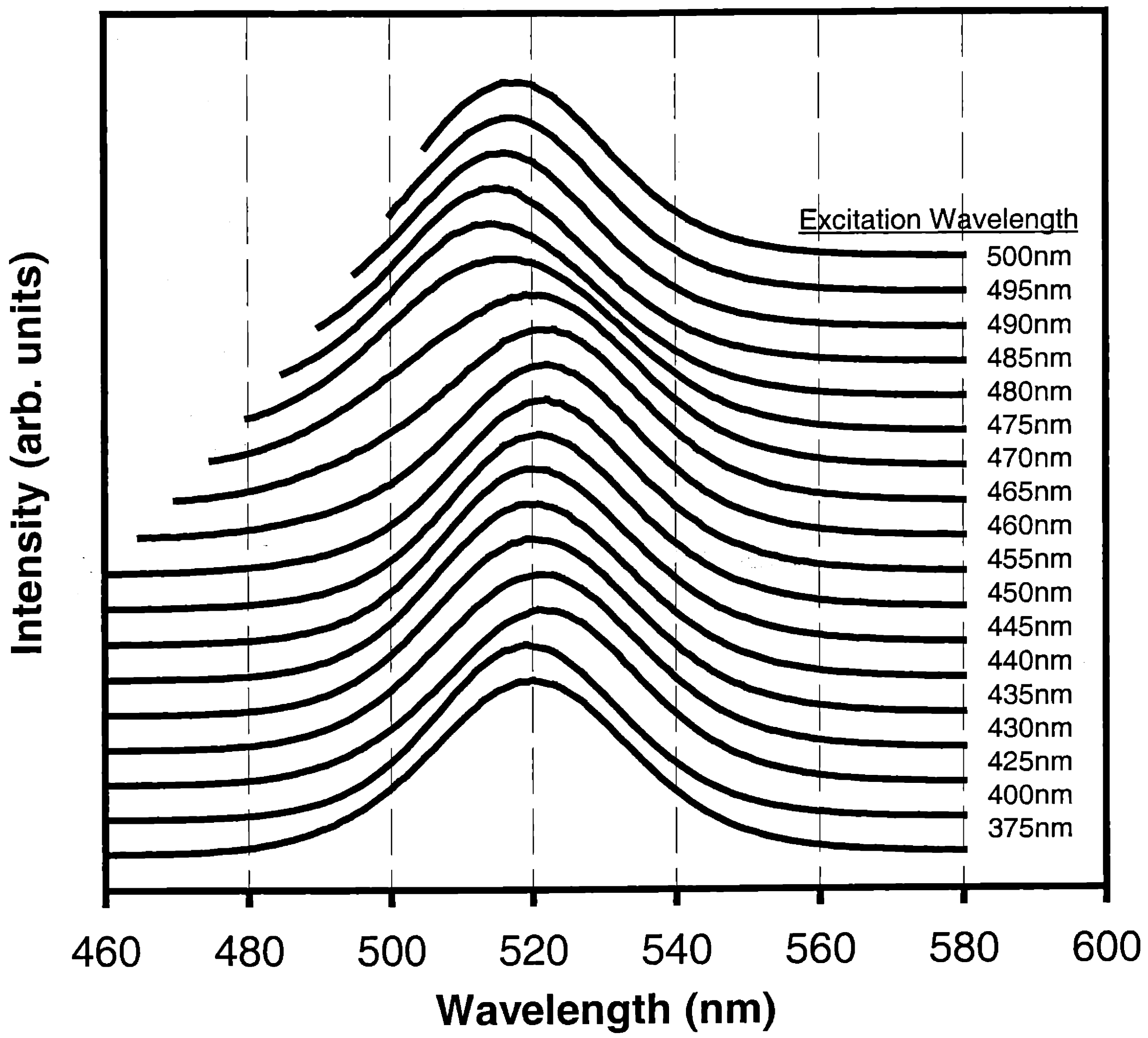

Figure 3.1 Photoluminescence of green-emitting QDs (band edge absorption peak at 500nm) in dilute solution (OD < 0.1) in hexane at various excitation wavelengths. PL peak varies only slightly until QDs are excited between 475nm and 490nm. Shift of peak to blue indicates preferential excitation of bluer QDs because of the direct excitation of their band edge absorption state.

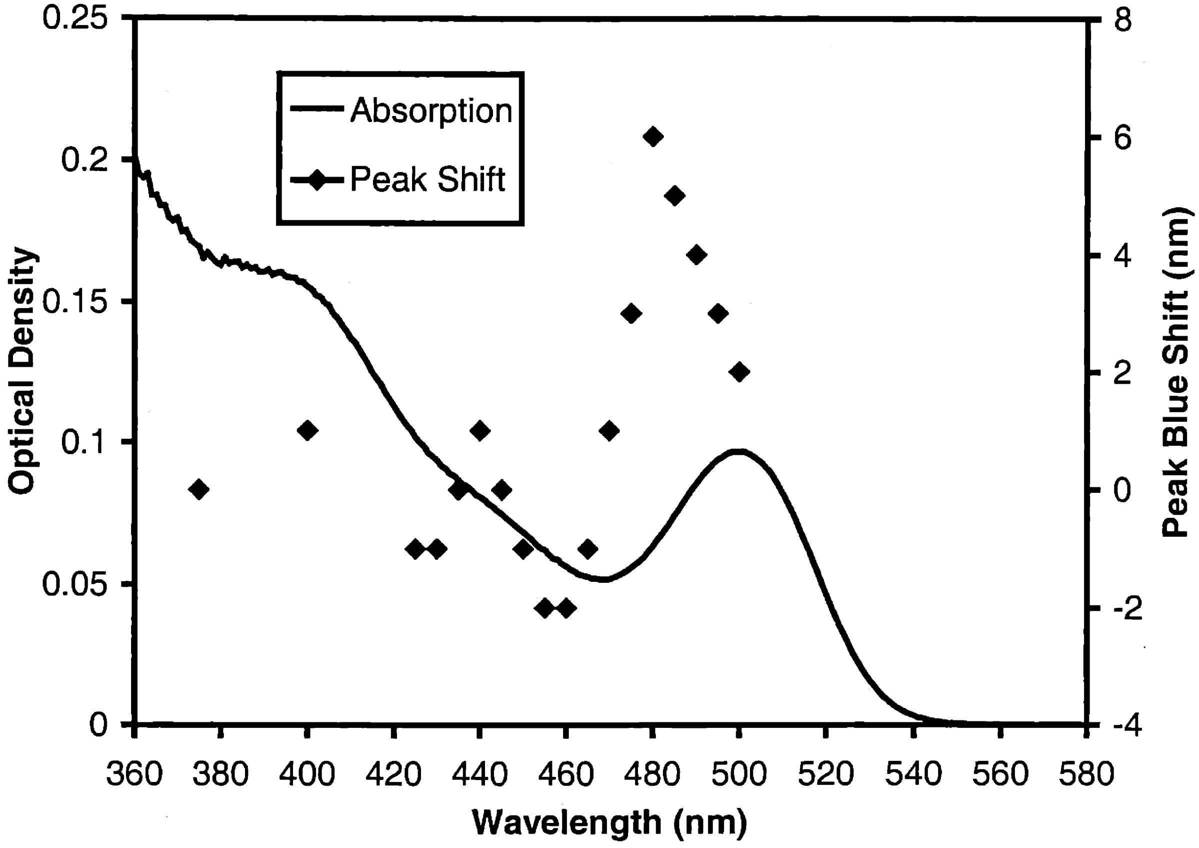

Figure 3.2 Solid line is the absorption profile of the 500nm QDs whose luminescence is shown in Figure 3.1. The diamonds correspond to the blue shift of the luminescence peak from 520nm. The blue shift reaches a maximum on the blue end of the band edge absorption peak.

turn, emit light characteristic for their size. With increasing QD concentration or optical path length the chance of the bluer emitted light being absorbed increases. A high concentration solution of QDs results in a red-shift and narrowing of the PL peak.

The presence of deep trap states at the surface of the quantum dots causes low intensity, broad emission to the red of the main emission wavelength.[7] Passivation of the CdSe core with a ZnS shell eliminates most of this emission. In dilute solution the broad red luminescence is very weak (<1% of the main peak intensity). However, the absorption and re-emission process described above can significantly enhance the presence of the deep trap emission relative to the intensity of the band edge emission.

3.3.2 Simulation Model

During the simulation, a ray which begins at the emitting region of the exciting LED is followed as it moves through the device. The ray is subject to absorption, and subsequent re-emission, in the parts of the device containing the QDs, and reflection at polymer/air interfaces. Cartesian coordinates are used for both the position and direction of the ray as it travels through the device. The center axis of the device is defined as the x-axis with the y and z axes pointing away from the center radially. Figure 3.3 shows a diagram of the modeled device structure. Light emerges from the blue LED and travels through the QD-containing layer(s) until it reaches the end of the device where it emerges and is collected. The blue excitation light source is modeled as a narrowed cosine distribution, with the center of the cone of emitted light directed down the center of the polymer rods. The direction of the excitation source ray is chosen at random from the possible directions available in a cone with a vertex angle of θ_{max}. First, the polar angle, θ, which is measured from the x-axis, and the azimuth angle, ϕ, are chosen:

$$\theta = \cos^{-1}\left(\cos\theta_{\max} + \left(1 - \cos\theta_{\max}\right)R_f\right) \qquad \text{Eqn 3-1}$$

$$\phi = 2\pi R_f \qquad \text{Eqn 3-2}$$

R_f is a random number chosen from the range [0,1].

Then the direction cosines (l, m, and n) along the x, y, and z axes, respectively, are calculated using θ and ϕ:

$$\begin{aligned} l &= \cos\theta \\ m &= \sin\theta\cos\phi \\ n &= \sin\theta\sin\phi \end{aligned} \tag*{Eqn 3-3}$$

Once the direction is known, the intensity of the ray, I, is calculated:

$$I = \cos\left(\frac{90^\circ}{\theta_{\max}}\cdot\theta\right) \tag*{Eqn 3-4}$$

With a maximum cone angle of approximately 15° into air, the cone angle used for light entering the polymer, θ_{max}, was set at 22.5°, which takes into account the higher index of refraction of the QD-containing PLMA ($n = 1.5$) compared to that of air ($n = 1$). The ray's wavelength is chosen at random from the luminescence spectrum of the source LED. The position and direction of the ray after reaching the clear polymer / QD-polymer interface is recorded and used in the calculations which follow the ray through the next, QD-containing layer.

The distance the ray then travels through the next layer is determined using the absorption profile of the QDs in that layer. The absorption profile is measured as the optical density (OD) of the sample over a range of wavelengths. The OD is the logarithm of the attenuation of light that is transmitted through the sample being measured.

$$OD = -\log_{10}\left(\frac{I_{transmitted}}{I_{incident}}\right) \tag*{Eqn 3-5}$$

$I_{incident}$ is the unattenuated incident light intensity, and $I_{transmitted}$ is the attenuated transmitted intensity.

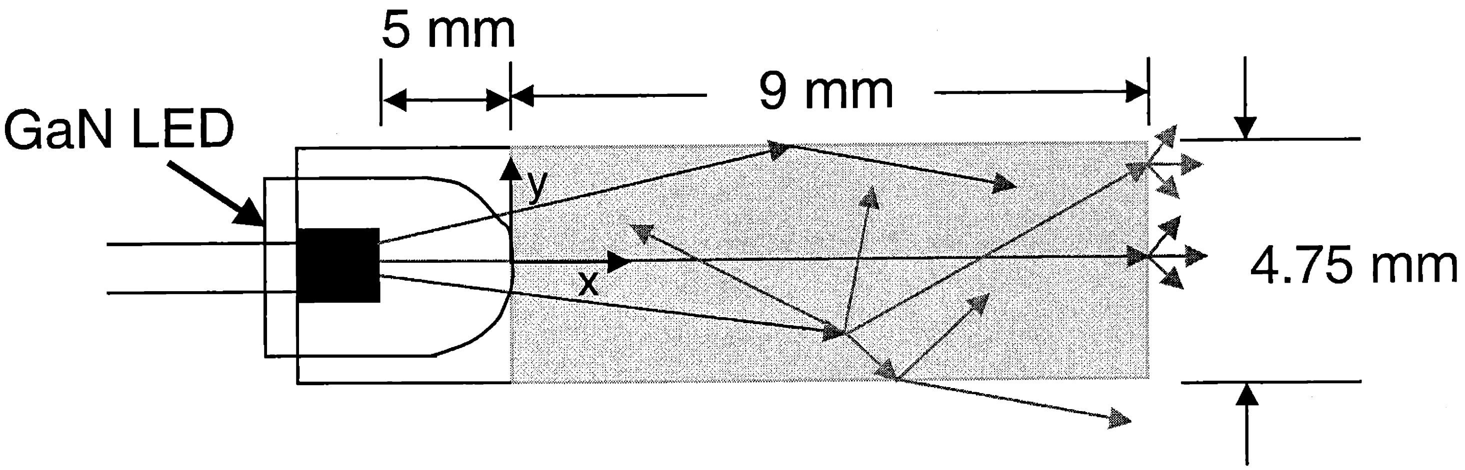

Figure 3.3 Cartoon of device model used in simulation. Here a single layer of green QDs are excited by a blue LED. Arrows running from LED into QD/polymer area and subsequent arrows radiating outward from those initial rays suggest possible outcomes for a ray emitted from the LED and travelling through the device. The coordinate axes have their origin at the cylindrical center of the polymer cap and right at the tip of the blue LED. Travelling down the center towards the final emission end is moving down the +x axis.

The mean path length, Λ, at a given wavelength, λ, is:

$$\Lambda = \frac{0.4343P}{OD(\lambda)} \qquad \text{Eqn 3-6}$$

P is the path length of light through the absorbing material, and OD(λ) is the optical density at the wavelength of interest. A particular ray travels distance D_Λ,

$$D_\Lambda = -\Lambda \ln(1 - R_f) \qquad \text{Eqn 3-7}$$

This distance is compared to that of the cylinder wall, D_{wall}, and the cylinder end, D_{end}.

$$D_{wall} = \frac{-(my+nz)+\sqrt{(my+nz)^2-(m^2+n^2)(y^2+z^2-r^2)}}{m^2+n^2} \qquad \text{Eqn 3-8}$$

$$D_{end} = \frac{L-x}{l} \qquad \text{Eqn 3-9}$$

where x is the center axis coordinate; y and z are the radial coordinates; l, m, and n are the direction cosines along the x, y, and z axes, respectively; L is the cylinder length; and r is the cylinder radius.

If D_Λ is the smallest value, the ray is absorbed, with the position of the absorption event (x, y, z) recorded. The probability of a photon being emitted from that position is equal to the quantum yield. This is modeled by multiplying the intensity of the ray by the quantum yield. The direction of travel is chosen at random to model the isotropic nature of emission from an ensemble of QDs. The emitted wavelength is also chosen at random from the dilute PL fitting with the constraint that the new photon can not be to the blue of the absorbed photon. Using a truncated dilute PL fitting to choose the new wavelength is justified by considering the PL spectra shown in Figure 3.1. Because of the absorption of all wavelengths to the blue of the band edge for a particular quantum dot, the emission produced by excitation at a wavelength within the dilute PL spectrum almost identical to that produced by excitation far from the band edge. Ignoring the significant blue shift of the PL when exciting on the blue side of the band edge absorption peak is justified by considering that the "excess" blue light emitted will experience the highest re-absorption (being at the peak of the band edge absorption) and will therefore be shortly absorbed and re-emitted with a wavelength distribution similar to that of the "average" emission peak.

If D_{wall} is the smallest, then the light either reflects back into the interior of the rod or it escapes. The reflection probability, R, is calculated by averaging the squares of the transverse electric (TE) and transverse magnetic (TM) reflection coefficients:

$$R = \tfrac{1}{2} r_{TE}^2 + \tfrac{1}{2} r_{TM}^2 \qquad \text{Eqn 3-10}$$

$$r_{TE} = \frac{n_1 \cos\theta_1 - n_2 \cos\theta_2}{n_1 \cos\theta_2 + n_2 \cos\theta_1}$$

$$r_{TM} = \frac{n_2 \cos\theta_1 - n_1 \cos\theta_2}{n_2 \cos\theta_1 + n_1 \cos\theta_2}$$

where n_1 is the index of refraction of the polymer, n_2 is the index of refraction of air, and θ_1 and θ_2 are the angles of incidence in the polymer and air respectively. Also, θ_1 and θ_2 are related by Snell's Law. The ray's intensity is multiplied by R, then D_Λ and D_{end} are reduced by D_{wall}, and D_{wall} is recalculated.

If D_{end} is smallest, the reflection probability is calculated using Eqns. 4. The ray's intensity, I, is multiplied by R, and the intensity $(1-R)I$ is added to the value recorded in an array at the array index that is equal to the wavelength of the ray. The ray is followed through the rod until it's intensity falls below a particular threshold. At that point the process starts over again. The final sum of intensities recorded in the array is the output of the model.

3.3.3 Characterization of Quantum Dots Used in Mixed Color LEDs

Before fabricating LEDs to study and compare with the simulation, we characterize the optical properties of the QDs to be used in the device. Three sizes of QDs were used in creating the devices. For red emission, we used large QDs (~30 Å radius, ~10 Å ZnS shell thickness) having a peak emission of 636 nm (R636). A yellow-green solution of QDs (~20 Å radius, ~10 Å ZnS shell thickness) having a peak emission at 544 nm (G544), and a green solution (~15 Å radius, ~10 Å ZnS shell thickness) having a peak emission at 524 nm (G524) were used for green light emission.

The luminescence and absorption properties needed for simulating the optical behavior of the QDs are: the PL spectrum of a dilute solution of QDs, the absorption profile of the QDs, their quantum yield, and the absorbance of the QDs in the final polymer composite at a particular wavelength (usually the wavelength at which the excitation light is peaked). PL spectra of dilute (optical density at peak of first absorption feature less than or equal to 0.1) QD solutions are taken using a SPEX Fluorolog spectrometer. Figure 3.4 shows dilute PL spectra taken from samples G520, G544, and R636. By using a dilute solution of QDs for the PL measurement, the effect of re-absorption, larger QDs absorbing light emitted by smaller QDs, is minimized. This PL spectrum is then fitted using the sum of two or more gaussian curves. The broad deep trap emission is modeled as a sum of error functions. These error functions are the result of integrating the gaussian fits of the main peaks and multiplying by a suitable constant to match the observed deep trap emission. The gaussian and error function curves found by fitting the PL peaks are then used to generate arrays that are used to determine the wavelength emitted by the QDs during the simulation. Absorption profiles for the same samples of QDs were taken with a UV-Vis HP 8452 diode array spectrophotometer. The absorption profile, in conjunction with the known absorbance at a particular wavelength in the composite, enables the calculation of the mean free path length of a photon of a particular wavelength in the material. The quantum yield is the ratio of emitted photons to absorbed photons, i.e. the probability that a typical QD will emit after absorbing a photon. The quantum yield of the QDs is determined by comparing the PL intensity of a dilute solution of QDs with that of an organic dye with known quantum yield. Specifically, rhodamine 590 and 640 were used as the reference dyes. When dispersed in monomer solution, G520, G544, and G636 have quantum efficiencies of 20%, 30%, and 30%, respectively.

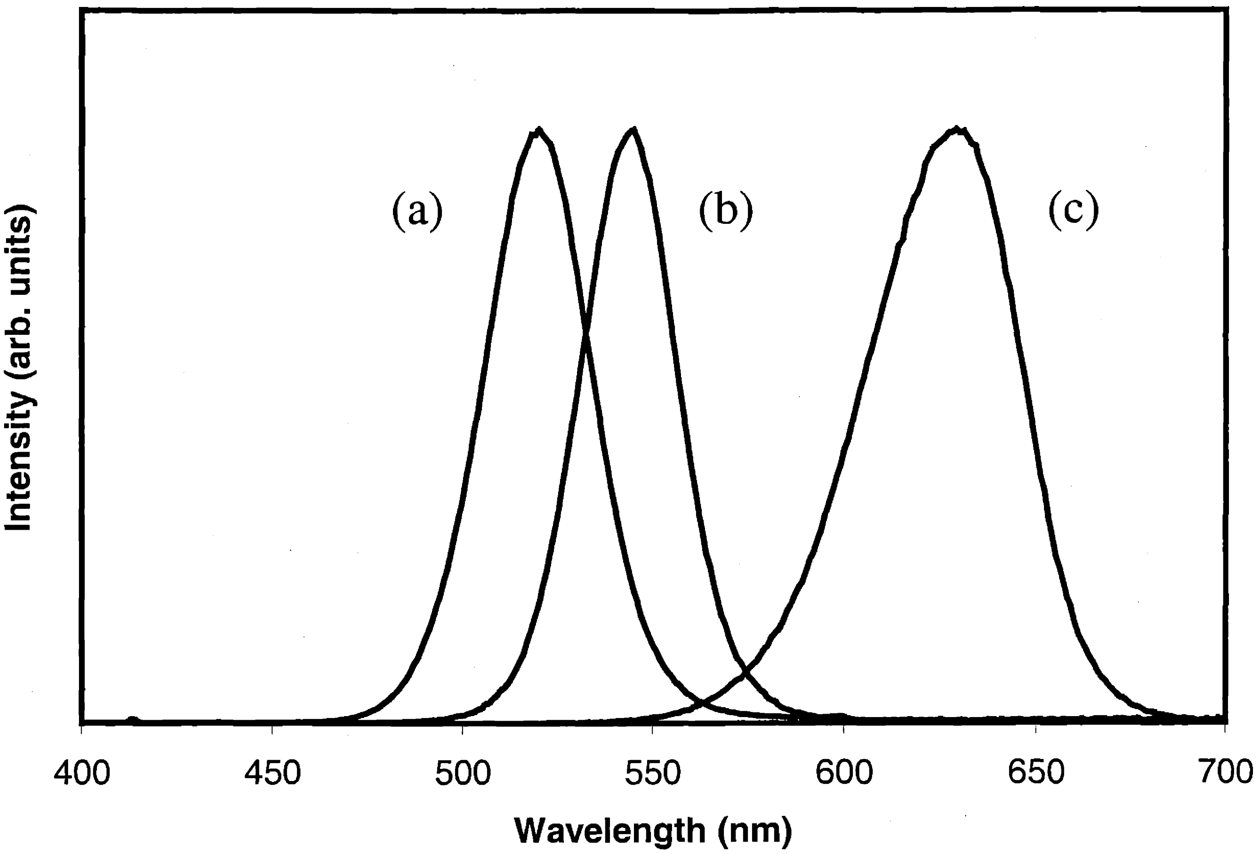

Figure 3.4 Photoluminescence spectra of (a) G520, (b) G544, and (c) R636. The spectra are taken of the quantum dots while they are dispersed in hexane. The optical density of the solutions at the first absorption peak is less than 0.1 to prevent self-absorption to skew the luminescence detected from the solutions. These spectra are fitted with sums of gaussian functions and error functions which are then used in the simulation.

Additional inputs for the simulation are the index of refraction of the polymer and the direction and wavelength of the incident excitation light. The index of refraction of the polymer is assumed to be 1.5, which is close to the value of that of LMA, which is 1.49. Calculations made with n = 1.4 and 1.6 showed little change in the resulting output.

3.4 Synthesis of Mixed Color LEDs

Mixed light LEDs were produced using two similar procedures, one for simple, one QD-containing layer LEDs and the other for two layer, near-white emitting LEDs. GaN LEDs emitting near 465nm and with an emission cone angle of approximately 15° were ordered from Nichia Chemical Co.

To check the simulation for accuracy, very simple LED structures were created. G544 QDs were dispersed in 10:2.5:1 LMA:EGDMA:TOP monomer solution and the absorption spectrum taken with the solution in a cuvette. The solution was then added to a 6mm outer diameter culture tube and polymerized for ~15 minutes at 60 °C. After this initial hardening of the polymer, a diode was placed in the culture tube end down, and resting on the partially polymerized G544 containing polymer rod. Clear monomer solution was added to embed the diode in clear polymer and the system was placed back in the oven at 60 °C for 1.5 to 2 hours. The diode/polymer rods were then removed from the culture tubes and their tips microtomed flat to give a flat reflective end, which would behave optically like the end of the simulation model.

When using the simulation as a predictive tool, greater precision with regard to QD spatial distribution, length, and optical density were required. In this case, the green , red and clear/diode sections were all polymerized separately. After polymerization, the resulting polymer rods were removed from the test tubes and cut to the length required for the proper optical density.

The actual optical densities of the cut pieces of rod were checked by measuring the absorption of the rods end-on using the UV-Vis spectrometer. The optical density measurement required placing the cut rods in a hole of the same diameter as the rods which had been drilled into an opaque block. The block's dimensions were the same as those of a cuvette so as to fit securely in the UV-Vis spectrometer cuvette holder. All of the rod pieces had rough end surfaces where they had been cut by a razor to the correct length. The pieces were too short to be held well by the microtome grip so another method of preventing scattering at the surfaces had to be found. For the absorption measurements a drop of paraffin (or white) oil was placed on the ends of the rod when placed in the opaque block. The oil wet the surface and greatly reduced the light scattering due to the surface roughness. Even so, the reduction of light caused by the opaque block as well as remaining scattering from the rod/oil system gave very high background readings. Furthermore, the background was not flat but had characteristic features. These features appeared to be due to scattering at the rod end. Fairly smooth, uniform rod ends had less pronounced absorption background and background features. After carrying out absorption measurements on the rods with QDs present, the absorption measurement of a clear polymer rod was used to eliminate the absorption features so that the background was flat and the optical density of the rods at 465nm could be ascertained. Figure 3.5 shows the background corrected absorption spectrum for both G520 and R636 used to make the near-white diode simulated below.

The clear polymer/LED end is cut flat. The QD-containing polymer rods are then epoxied onto the LED and a piece of a glass coverslip is epoxied onto the end of the device. The epoxy produces a clear, small index change joint between the polymer pieces. The piece of coverslip provides a smooth end surface, which is easier to model with respect to reflection. Figure 3.6 is a schematic of the device.

The luminescence from these devices is measured using a SPEX Flourolog spectrometer, with the light from the device scattered by reflection off of a matte white surface prior to entering the receiving slit of the spectrometer. Scattering the light emitted by the device is necessary because the spectrum of colors emitted by the device is dependent on the viewing angle. The highly directional blue output from the GaN LED varies with direction differently than does the isotropic emission from the QDs. This leads to a greater blue component in light emitted directly outward along the device axis, while light emitted toward the side is richer in light emitted by QDs.

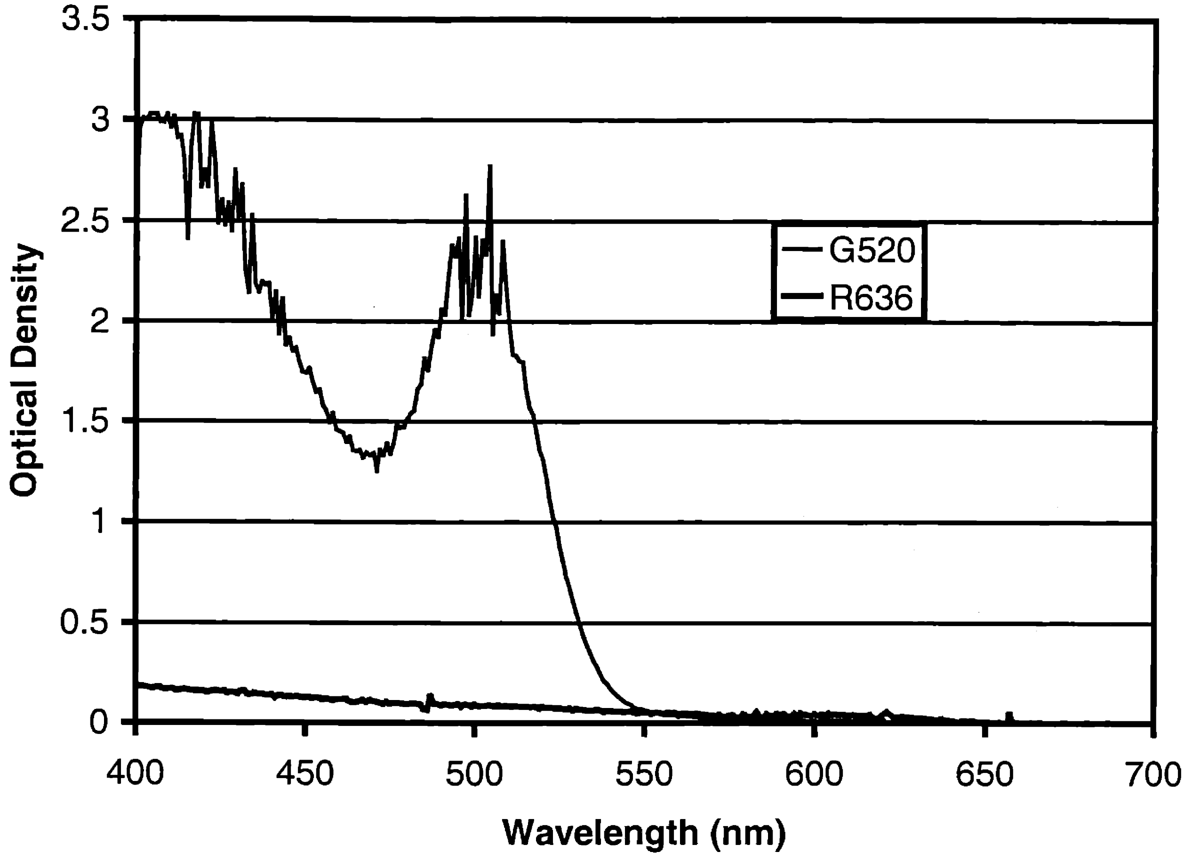

Figure 3.5 Corrected optical density measurements of both G520 and R636. The optical density at 465nm (the LED emission peak) is 1.4 for G520 and 0.12 for R636. The need to subtract a background with noticeable features and the detection limits of the spectrometer (note the noisiness of the G520 measurement with OD > 2) make getting a precise optical density measurement difficult.

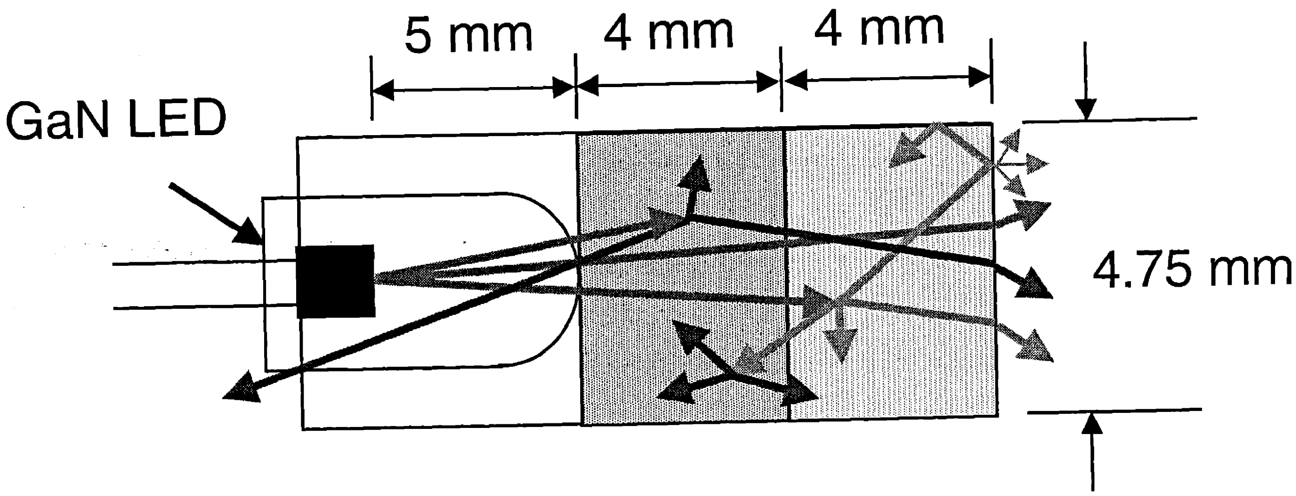

Figure 3.6 Cartoon of composite LED structure. A blue GaN LED emits a 15° cone of 465 nm blue light. This light then travels through the red and green layers exciting the quantum dots in each layer as it proceeds. The green layer is closer to the end than is the red so that the green light that is emitted does not need to travel through the red and be absorbed. The simulation takes into account the optical density of the layers, their physical dimensions, and the reflectivity of the polymer-air interface.

3.5 Results and Discussion

Figure 3.7 shows the measured and calculated emission profiles of devices with a single layer of G544 with two different optical densities. The primary change in spectral peak positions and shapes is a red-shifting and narrowing of the peaks. This is due to the re-absorption process as described above. Light to the blue end of the emission spectrum is rapidly absorbed while light at the red tail of the emission sees little to no absorption and escapes. Note also the enhancement of the low intensity flat emission to the red of the peak. This emission from deeptrap states is enhanced just as is the reddest band edge emission. The blue LED emission also exhibits the red-shifting and narrowing. This is because the optical density of the QDs rises with decreasing wavelength at the wavelengths the LED is emitting. Thus the blue side of the LED peak is absorbed more than is the red side. The relative positions of the blue LED emission, green QD emission and QD absorption are shown in Figure 3.8. There is good agreement between the calculated and measured spectra.

Given this agreement, the simulation was used to find a combination of red and green QD layers that would provide white light. In the design the red layer was placed closer to the blue emitting LED than was the green layer. In this way, the emission from the green QDs would not be reabsorbed by the red QDs, which would reduce the luminescent efficiency of the device. Emission spectra of devices with different red and green layer optical densities were calculated. The CIE diagram coordinates which correspond to each spectrum were calculated using the tabulated values and formulae in Reference 1. The resulting X – Y values were interpolated to find the optical densities which would give X = Y= 1/3.

The X, Y coordinates calculated for the various simulated emission spectra are plotted in Figure 3.9 and outline the color gamut available using the 465nm blue from the LED, the 544nm green from G544, and the 636nm red from R636. Increasing the concentration of R636 causes a shift along straight lines in the interior of the color gamut. Increasing the concentration of G544 produces a path which curves away from the blue-green side of the diagram and towards the green-red side.

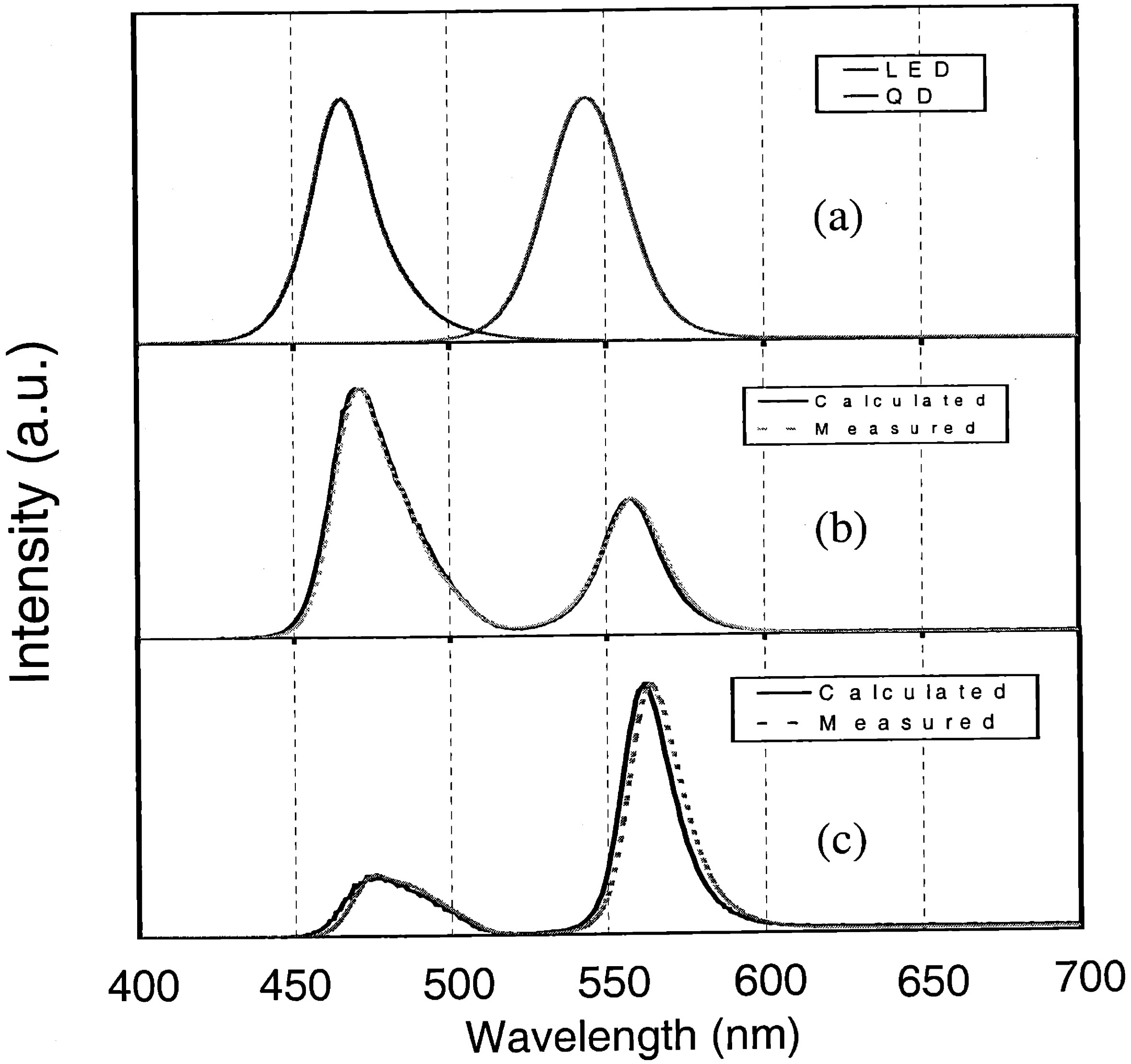

Figure 3.7 Evolution of luminescence with increasing concentration of G544. The top spectrum, (a), shows the normal output of the blue LED and the dilute solution spectrum of the green, G544, quantum dots. This corresponds to zero absorption. (b) and (c) correspond to optical densities of 0.24 and 0.64. The simulation tracks the data well. The expected red-shifting of both the blue and green peaks are captured in the data and simulation.

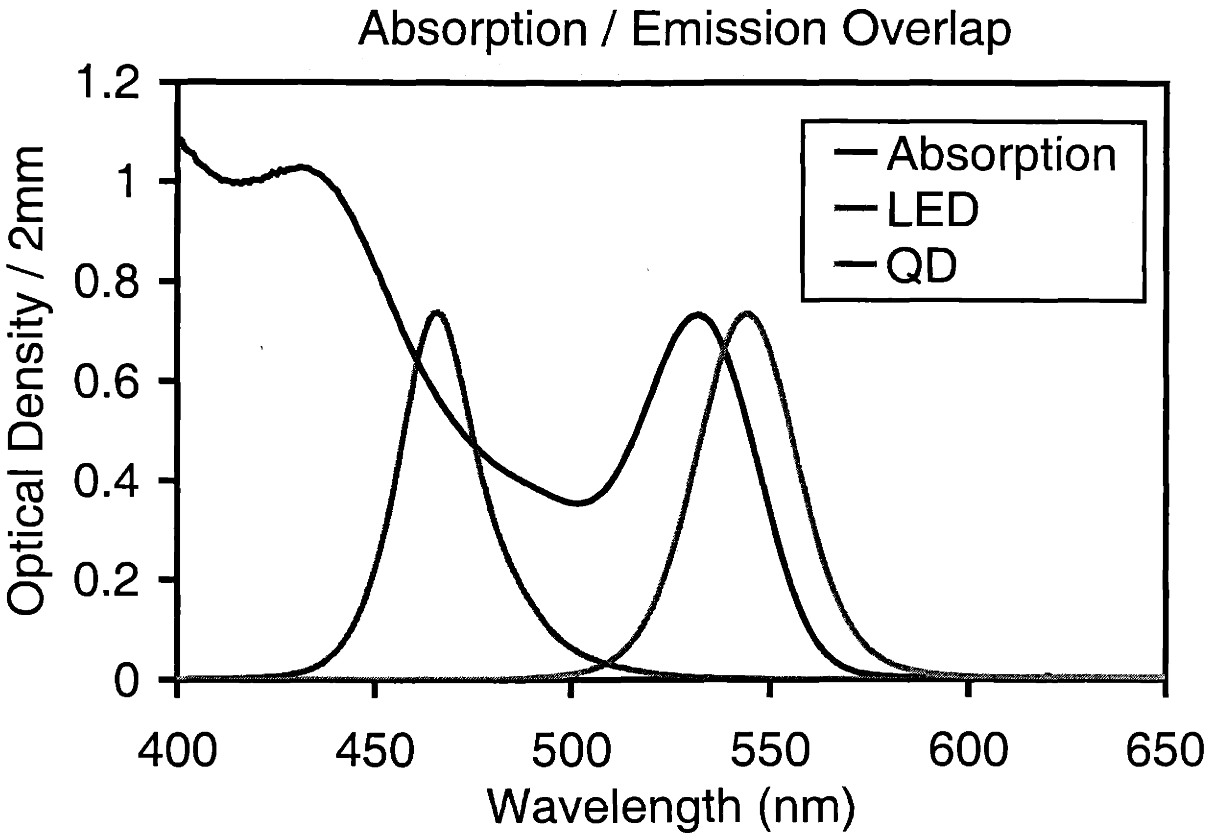

Figure 3.8 Absorption profile and dilute PL spectrum of G544 in hexane along with the 465nm emission of a blue Nichia GaN LED. Note the significant overlap of the G544 band edge absorption and emission peaks. The emission peak of the LED is seen to be located where the absorption profile of the G544 QDs is decreasing with increasing wavelength.

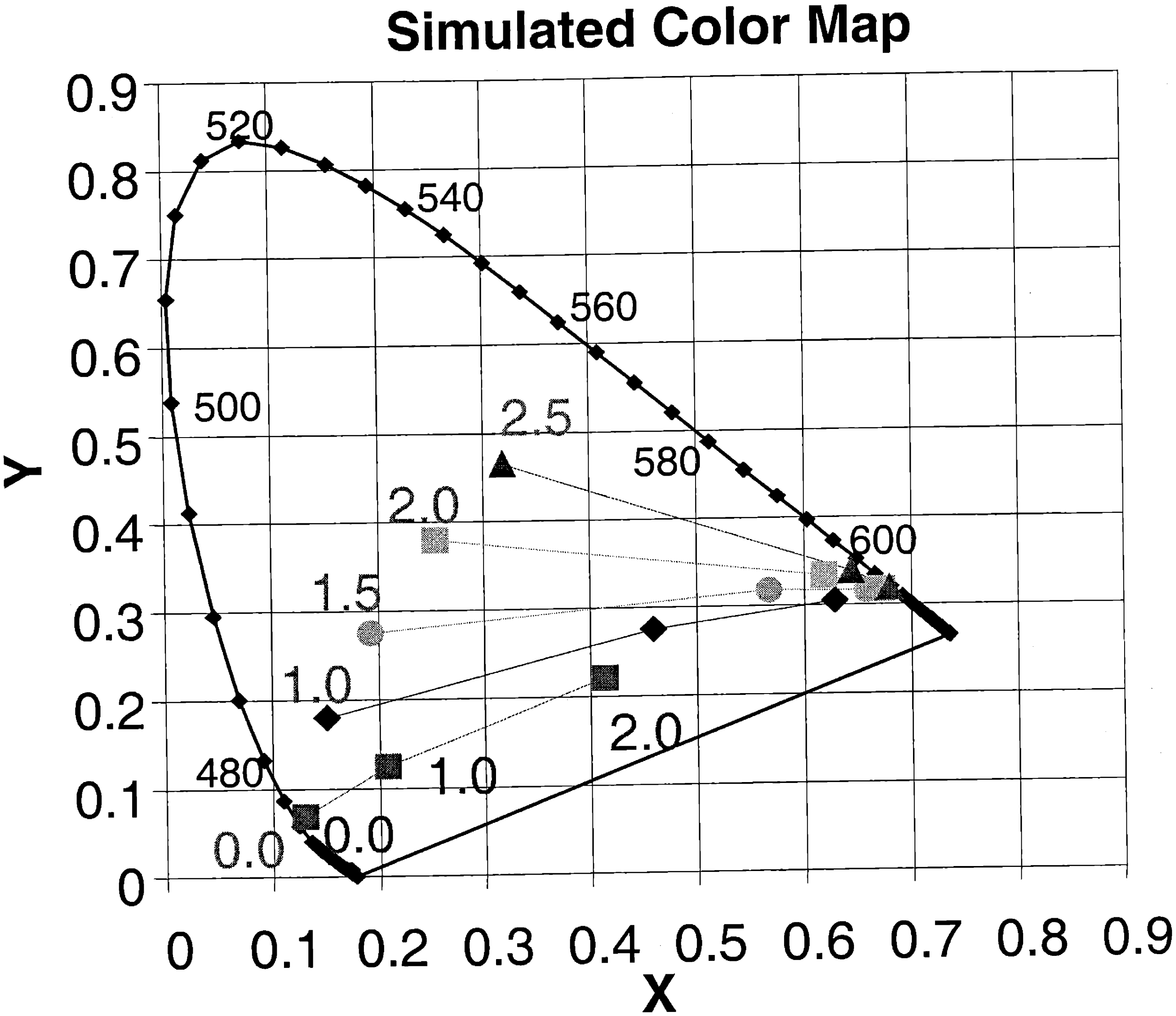

Figure 3.9 The color gamut, or range of colors, available using a 465nm blue Nichia LED, 544nm green quantum dots and 636nm red quantum dots is shown above. Each point was calculated with a given optical density of green and red quantum dots in their respective 4mm thick layers. Altering the red optical density produces a linear change in the X-Y coordinate because of the close spacing of red wavelengths in the corner of the diagram. Red shifting has little effect. For the green, however, the red-shift in green output with increasing green concentration has a large effect on the effective green color coordinate, thus producing a curved response to increasing green concentration.

As the concentration of G544 is increased, re-absorption and re-emission shifts the green peak toward the red, thereby moving its X,Y coordinate towards the red corner of the CIE diagram. The X,Y coordinate of the red peak, however, is almost constant even with re-absorption. This is due to the close spacing of wavelengths in the red corner of the diagram.

Figure 3.11 shows the spectrum of a device produced using G520 and R636. The R636 piece has an optical density of 0.12 and a length of 5.0mm. The G520 piece has an optical density of 1.35 and a length of 9.0mm.

The initial calculations were made with assumed piece lengths of 4.0mm each. However, the QD concentrations in the synthesized rods were lower than that assumed, so longer pieces had to be used. Both the comparison of simulation results with the measured spectrum, and simulation runs that vary the piece length while holding the optical density constant show that this does not have an effect. The reason this is, is the acceptance cone angle of the polymer rod. The acceptance cone angle determines the cone of light that can escape the rod end. Light that is emitted at an angle within approximately 45° of the x-axis will experience total internal reflection if it strikes the rod wall, or is likely to escape if it strikes the rod end. However, light outside of this cone will escape out the sides or reflect off the end. Thus, wherever the light is emitted, its chance of escaping is set by its direction of travel rather than position.

Both the red and green peaks match the simulation well. Care must be taken to get an accurate measure of the relative blue intensity, however. The directional nature of the blue emission of the diode requires the use of an enclosing scattering surface, like an integrating sphere. In this case, the interior of a disposable cuvette is painted matte white. A hole in the side of the cuvette allows scattered light to escape and be analyzed by the spectrometer. A cartoon of the measurement system is shown in Figure 3.10. In Figure 3.11 simulation results with a G520 optical density of 1.5 is included with that of 1.35. The intensity of the blue peak is essentially the only thing effected. However, the significant change in blue intensity with a 10% change in green optical density shows the high sensitivity of the output to the optical density of various pieces of the system. Thus great care must be taken to precisely measure the optical density of each component if the simulation is to be used as a design tool.

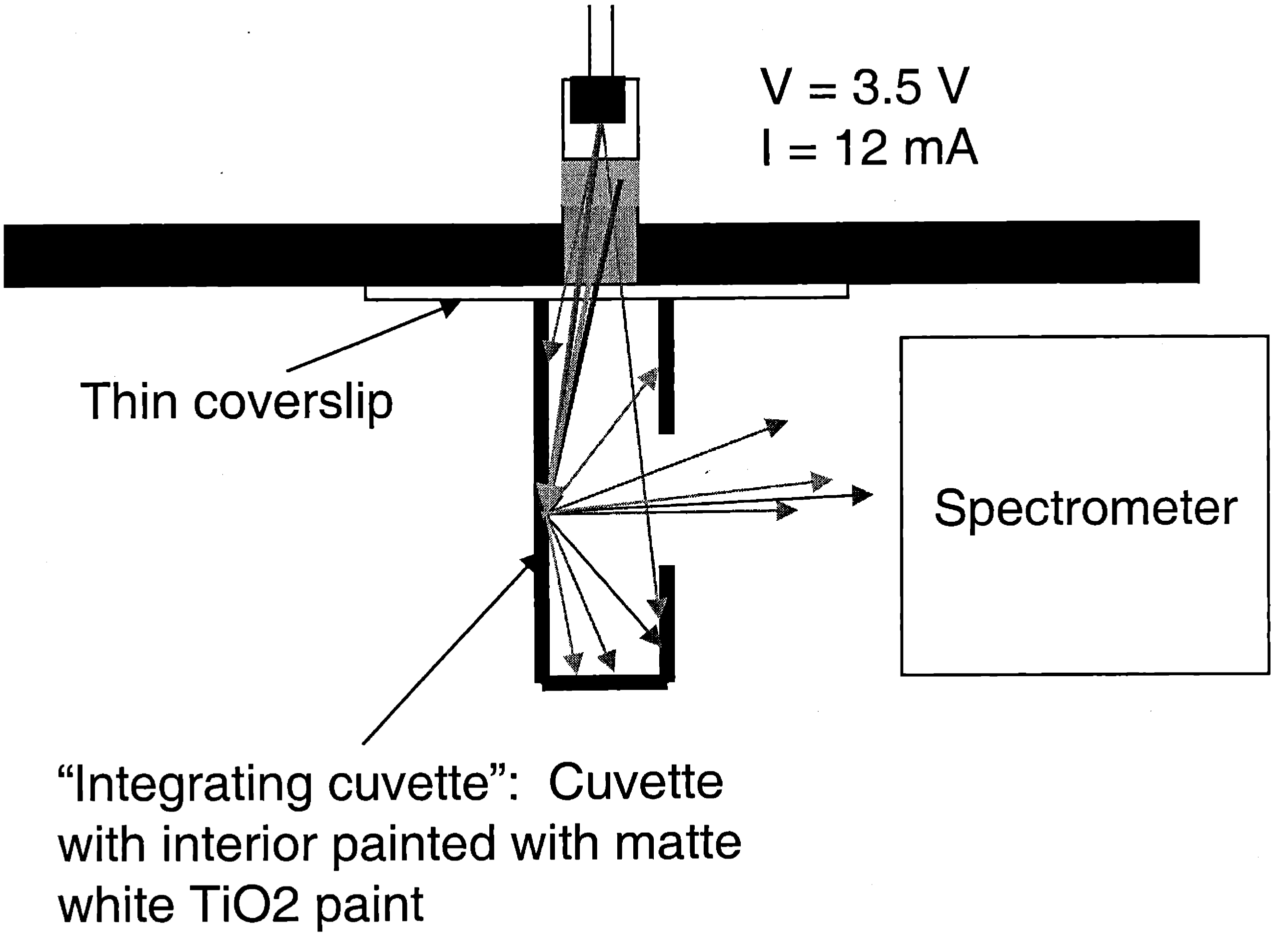

Figure 3.10 A cartoon of the measurement setup used while measuring luminescence spectra from Nichia LED/ R636 /G524 devices. The interior matte white paint thoroughly scatters the incoming light so that what is sent on to the spectrometer is an accurate measure of the spectrum of all light leaving the end of the device. This sampling of light to the spectrometer should match the characteristics of all the light which leaves the end, which is the result calculated in the simulation.

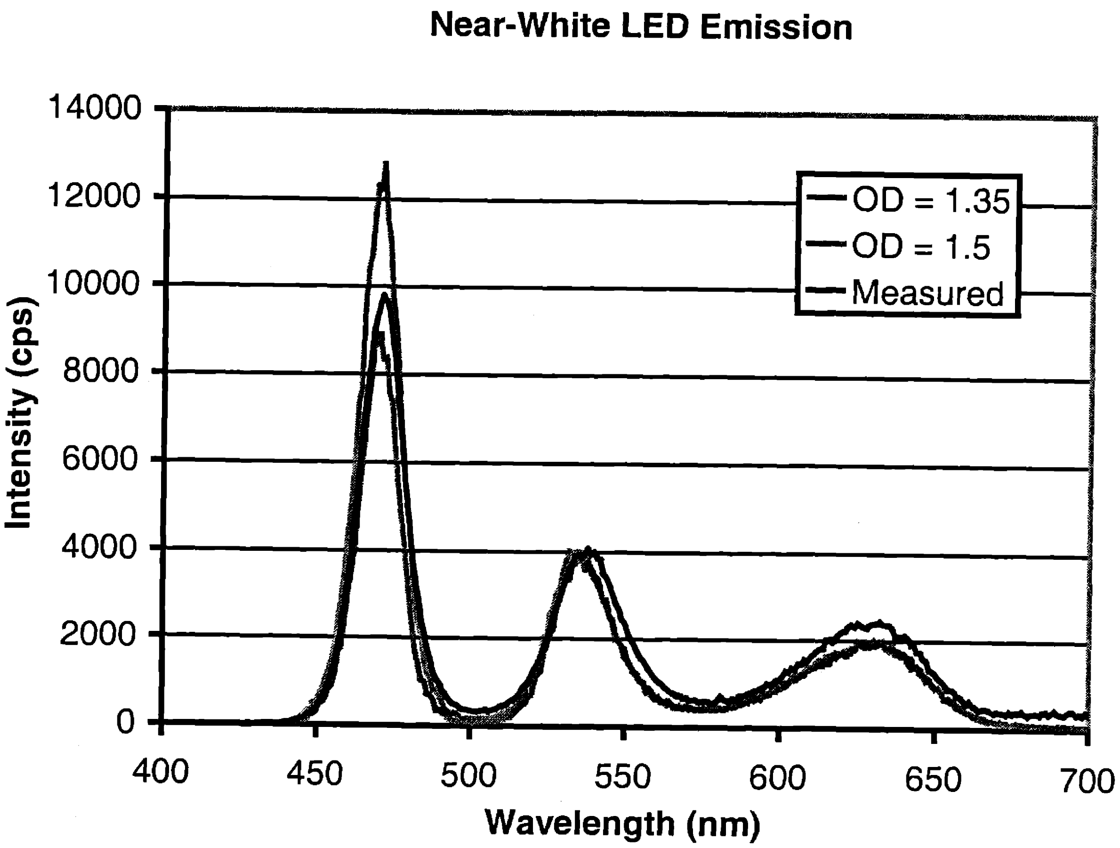

Figure 3.11 Comparison of luminescent output from Nichia LED/ R636/ G524 to simulation runs with a green optical density of 1.35 and 1.5. The green OD = 1.35 is the absorption of the green rod measured directly. A 10% increase in OD significantly changes the blue intensity. Use of the simulation as a predictive tool must be taken with care.

As mentioned above, the use of QDs with a dilute emission peak at 520nm still produced a relatively small color gamut due to re-absortion of the green light and the subsequent red-shifting of the green layer's emission. Furthermore, the absorption minimum to the blue of the first absorption peak (Figure 3.2) lies almost exactly at the peak emission wavelength of the blue LED, 465nm. Thus the absorption of the blue light by the green is less "efficient" than is the red-shifting process caused by absorption near the green emission peak. An improvement in QD absorption efficiency and final, red-shifted emission wavelength, may be produced by using QDs with an absorption maximum at the blue LED emission maximum. Thus absorption is improved, reducing the amount of green quantum dots needed, and the red-shifting produced by re-absortion would move the green emission peak from approximately 485nm towards the corner of the CIE diagram at 520nm. Furthermore, the narrowing of the emission peak, also an effect of re-absortion, would bring the X,Y coordinate of the green emission peak closer to the sharp bend of the CIE diagram, further extending the accessible color gamut.

3.6 Conclusion

Several candidate polymer systems for use as matrices for QD containing solids have been evaluated. The most successful system, polylaurylmethacrylate, makes use of the presence of TOP capping group to maintain the surface passivation of the QDs while the lauryl carbon chains act to maintain solubility of the QD/TOP mixture. Having found a high brightness, high optical density QD/polymer system energy down-conversion devices in the form of LEDs illuminating QD/polymer sections were synthesized. The luminescence of these devices was both measured and simulated using a Monte-Carlo technique. Good agreement was found between measurement and simulation. With this good agreement, the simulation may be used as a device design tool.

3.7 References

1. P. Keller, Proc. SID **24** (1983) 317.

2. S. Guha, R. A. Haight, N. A. Bojarczuck, and D. W. Kisker, J. Appl. Phys. **82** (1997) 4126.

3. F. Hide, P. Kozodoy, S. P. DenBaars, A. J. Heeger, Appl. Phys. Lett. **70** (1997) 2664.

4. J. Lee, V. C. Sundar, J. R. Heine, M. G. Bawendi, and K. F. Jensen, Adv. Mater. **12** (2000) 1102.

5. B. O. Dabbousi, M. G. Bawendi, O. Onitsuka, and M. F. Rubner, Appl. Phys. Lett. **66** (1995) 1316.

6. C. R. Kagan, C. B. Murray, and M. G. Bawendi, Phys. Rev. B **54** (1996) 8633.

7. B. O. Dabbousi, J. Rodriguez-Viejo, F. V. Mikulec, J. R. Heine, H. Mattoussi, R. Ober, K. F. Jensen, and M. G. Bawendi, J. Phys. Chem. B **101** (1997) 9463.

8. C. R. Kagan, C. B. Murray, M. Nirmal, and M. G. Bawendi, Phys. Rev. Lett. **76** (1996) 1517.

9. Y. Fink, A. M. Urbas, M. G. Bawendi, J. D. Joannopoulos, and E. L. Thomas, J. Lightwave Tech. **17** (1999) 1963.

10. Quantum yield measurements were made of 13.4 Å radius CdSe, 4 monolayer ZnS QDs in hexane, pyridine, and PS in toluene. The pyridine and PS/toluene solutions were both prepared by initially cap exchanging with pyridine. The pyridine capped QDs could be redispersed in a PS/toluene solution but not in neat toluene. Furthermore, the QY values were 22% (hexane), 9% (pyridine), and 14% (PS/toluene). The solubility and QY data suggest that the PS does indeed coordinate with the QD surfaces.

11. M. Kuno, J. K. Lee, B. O. Dabbousi, F. V. Mikulec, and M. G. Bawendi, J. Chem. Phys. 106 (1997) 9869. This reference analyzes in detail the predicted Stokes shift of the luminescence of an ensemble of QDs by integrating the Stokes behavior of a very narrow size selection of QDs via fluorescence line narrowing experiments.

12. S. A. Empedocles, D. J. Norris, and M. G. Bawendi, Phys. Rev. Lett. **77** (1996) 3873.

13. D. J. Norris and M. G. Bawendi, Phys. Rev. B, **53** (1996) 16338.

14. V. I. Klimov and D. McBranch, Phys. Rev. Lett. **80** (1998) 4028.

15. V. I. Klimov, A. A. Mikhailovsky, S. Xu, A. Malko, J. Hollingsworth, C. A. Leatherdale, H.-J. Eisler, and M. G. Bawendi, To Be Published

Chapter 4

Synthesis of CdSe quantum dot – ZnS matrix thin films via electrospray organometallic cemical vapor deposition

4.1 Embedding QDs in inorganic matrix

In chapter 3 it was demonstrated that QDs could be embedded in an optically clear polymer and excited optically. These QD – polymer composites could then be used to modify light emitted by a standard inorganic LED to create mixed colors. However, in such a system the QDs were not accessible electronically. To electronically excite or otherwise interact with the QDs would require embedding them in a conducting or semiconducting matrix. In fact, bare CdSe QDs have been embedded in polyvinylcarbazole (PVK) and an oxadiazole dirivative (t-Bu-PBD).[1] The PVK acted as a hole transport material and the t-Bu-PBD was an electron transport material. Electroluminescence was demonstrated at cryogenic temperatures.

Embedding the CdSe-core ZnS-shell, (CdSe)ZnS, nanocrystals (NCs) in a wide band gap semiconductor, such as ZnS (E_g = 3.7 eV), would also enable optical or electronic excitation of the NCs while providing a transparent, chemically robust matrix which would encapsulate and protect them from the environment. (CdSe)ZnSe NCs have been embedded in ZnSe films via a technique dubbed electrospray organometallic chemical vapor deposition (ES-OMCVD).[2,3] However, the photoluminescence efficiency of the (CdSe)ZnSe NCs was quite low (0.3% to 0.4% when dispersed in pyridine)[3] compared to what has been achieved by overcoating with ZnS (10% to 15% in pyridine).[4] The higher luminescence efficiencies of the (CdSe)ZnS NCs described in Chapter 2 offer a significant improvement in film luminescence. Furthermore, ZnSe (E_g = 2.7 eV) absorbs blue light while ZnS is transparent to the entire visible spectrum. In this chapter we investigate the properties of films produced using the deposition technique described in References 2 & 3, while using (CdSe)ZnS NCs and embedding them in ZnS rather than ZnSe.

Earlier work by Rodriguez-Viejo, et. al. (Reference 4) demonstrated that these thin films exhibit absorption, photoluminescence, and cathodoluminescence corresponding to electronic transitions within the NCs. The dependence of the thin film composite luminescence on the size and crystallinity of the ZnS matrix has been examined. ZnS films containing 33 Å and 42 Å diameter NCs exhibit luminescence peaks at 560 nm and 600 nm, respectively, with linewidths of 30 – 40 nm. The thin film PL peak is red-shifted 6 – 10 nm from the PL peak produced by a dilute solution of NCs dispersed in a solvent. This red-shift is thought to be due to agglomeration of the NCs in the film, which enables energy transfer from the smaller NCs to the larger ones.[5] The PL quantum yields of the films is ~10% – 15%.

Cathodoluminescence from the films originates in the embedded NCs as well. The CL peak exhibits an additional red-shift (~6 nm) and wider linewidth (40 to 50 nm). The red-shift is attributed to a quantum-confined Stark effect. Furthermore, the intensity of the CL is strongly affected by the deposition temperature. Films grown at 250 °C are significantly brighter than those grown at 100 °C. Also, the CL intensity falls more quickly for the 100 °C samples than for those formed at higher temperatures. X-ray diffraction profiles of the films grown at the two temperatures indicate that the 250 °C grown samples possess a primarily cubic (zinc blende) crystal structure and are well crystallized. The 100 °C samples are not as well crystallized and also contain a hexagonal (wurtzite) phase. It is thought that the poorer crystallinity of the 100 °C samples is indicative of a larger number of defect states in ZnS films. These defect states may act to trap electrons ejected from the NCs due to the electron bombardment, thereby producing ionized NCs. The ionized NCs would no longer luminesce, leading to a decrease in the CL intensity, similar to the optical darkening effect seen with semiconductor doped glass after exposure to laser irradiation.[6] Attempts to improve the CL intensity of low temperature grown films by annealing at 300 °C resulted in alloying of the NCs and a subsequent drop of the PL quantum yield.

4.2 Experimental Procedure

We now investigate the evolution of the NC-film composite photoluminescence and crystallinity with deposition temperature. Smaller NCs (28 Å diameter) were used due to the general decrease in NC stability with decreasing size. The smaller NCs have a greater surface to area ratio, allowing more interaction of the exciton with NC surface states and the surrounding matrix. Also, any alloying which occurs would shift the PL of a small NC more than that of a larger NC, since small changes in the exciton radius have the greatest effect on the PL wavelength at the smallest NC sizes.

(CdSe)ZnS nanocrystals were synthesized using techniques described in Chapter 2. CdSe nanocrystals with an average diameter of 28 Å were grown and then overcoated with ~5 Å of ZnS. NC-ZnS thin films were then synthesized using an electrospray technique[7] described by Danek, et al[2] and Rodriguez-Viejo, et al.[4] The NCs were dispersed in a 2:1 acetonitrile:pyridine solution. Typical QD concentrations ranged from 0.5 to 1 mg/mL, which was lower than that normally used (1-4 mg/mL). This solution was then injected into a CVD reactor (Figure 1) at 10-30 μL/min via a capillary tube. A voltage of 3.7 – 4.0 kV was applied to the capillary to charge the QD solution being injected; producing a highly dispersed spray of NCs into the reaction chamber. The ZnS precursors, diethyl zinc (2.5 μmol/min) and hydrogen sulfide (25 μmol/min), along with the H_2 carrier gas mixed with the NCs before reaching the substrate surface. At the substrate surface, the NCs and ZnS were deposited simultaneously. The films were grown on glass substrates and had thicknesses ranging from 0.5 μm to 1 μm. Approximately 0.1 μm of ZnS was grown before and after QDs were introduced into the reactor to insure complete encapsulation of the QDs in the ZnS. Films with and without NCs were grown at 100 °C, 200 °C, 250 °C and 300 °C.

The microstructure of the NC-ZnS composite thin films was analyzed via x-ray diffraction and profilometry. The optical behavior of the films was studied using optical spectroscopy. Photoluminescence measurements were carried out at room temperature in a Spex Fluorolog-2 spectrometer with front-face collection. UV-Vis absorption spectra were acquired using a Hewlett-Packard 8452 diode array. X-ray diffraction (XRD) measurements were carried out on a Rigaku 300 rotating anode diffractometer in the θ-2θ

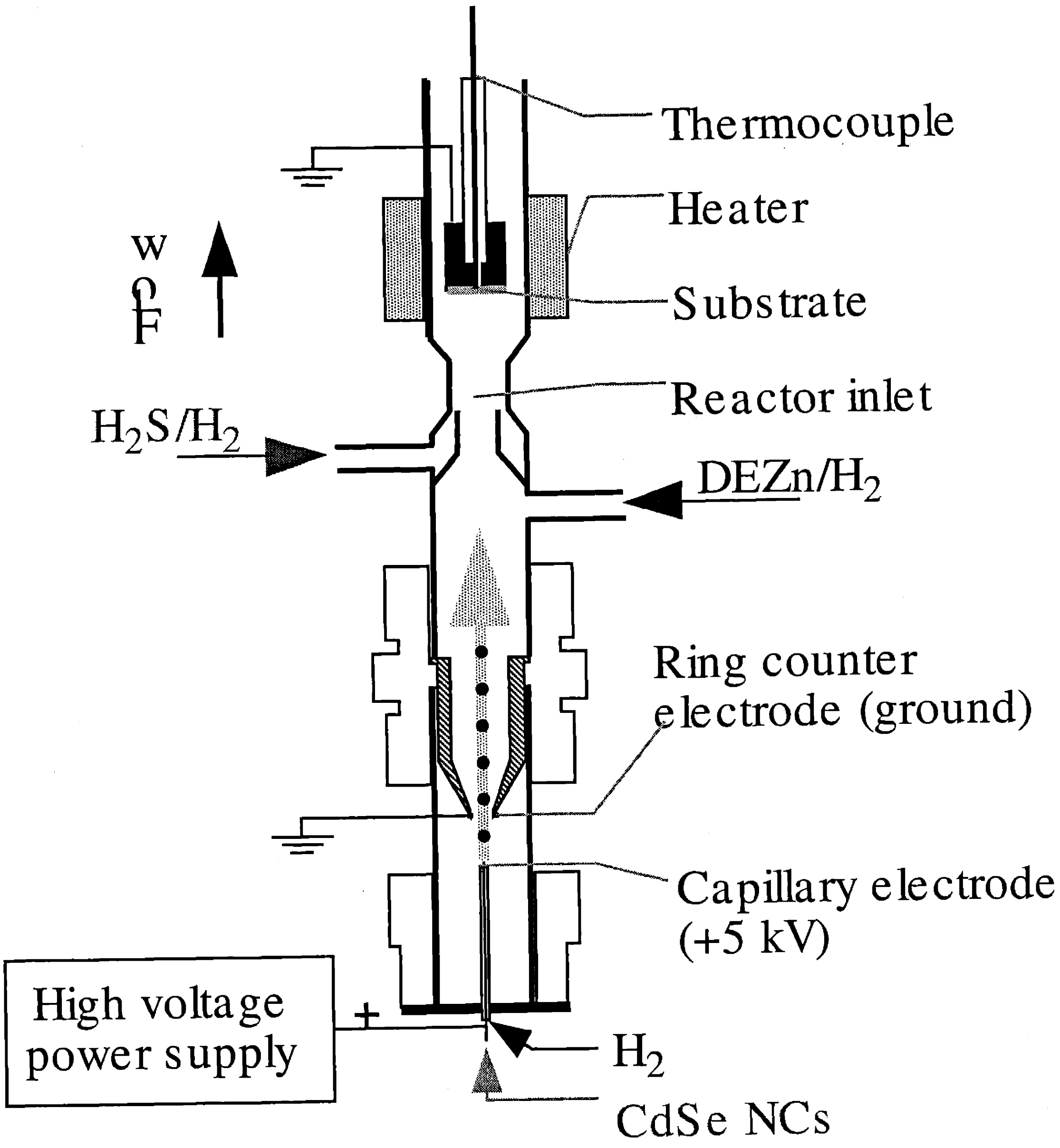

Figure 4.1 Schematic of ES-OMCVD reactor. NCs dispersed in 2:1 acetonitrile:pyridine solution slowly injected into base of reactor using syringe pump. hydrogen flow through outer concentric capillary tube carries droplets up to substrate. Droplets charged due to high voltage on capillary tube and break up as evaporate due to coulombic repulsion of charges on surface. ZnS deposited via CVD at substrate surface simultaneously.

configuration using Cu Kα radiation. Film thickness and roughness measurements were carried out using a Tencor P-10 profilometer.

Little difference was seen in the XRD profiles of the samples with NCs compared to those without NCs. X-ray diffraction profiles of films with and without nanocrystals show the same change in crystal structure with increasing temperature. X-ray diffraction profiles of films grown at the four deposition temperatures are shown in Figure 2. The films grown at 100 °C exhibit a hexagonal crystal structure (wurtzite) while those grown at higher temperatures have a cubic structure (zinc blende). This is consistent with the XRD profiles of the thin films containing higher concentrations of larger NCs. All of the films are highly oriented with the wurtzite films primarily possessing a (100) orientation and the zinc blende films possessing a (111) orientation. The average grain size of the films was estimated using the Scherrer formula: $L \sim \lambda/(\Delta 2\theta) \cos(\theta)$ where L is the average grain size, λ is the x-ray wavelength (1.54 Å), $\Delta 2\theta$ is the full-width-half-maximum (FWHM) dimension of a given diffraction peak in radians, and θ is the diffraction angle.

4.3 Results and Discussion

Grain sizes of the zinc blende samples range from 300 Å to 400 Å as calculated using the (111) peaks. The wurtzite grain sizes ranged from 200 Å to 250 Å as calculated using the (100), (002), and (110) peaks of the wurtzite samples. The presence of NCs did not significantly effect the x-ray diffraction peak widths and consequently did not change the grain size of the samples at any temperature.

Deposition without NCs at both 100 °C and 250 °C yields ZnS films with a surface roughness of ~500 Å to ~2000 Å. Adding QDs significantly increases the roughness (~2500 Å to 5000 Å) which gives rise to scattering of light off the film surface and a “frosted” appearance. The increase in roughness appears related to the amount of QDs deposited in the film. Films deposited while spraying an acetonitrile-pyridine solution which did not contain quantum dots have the same roughness as films deposited in the absence of spraying. Samples with an uneven coating of QDs exhibited increased roughness in areas with higher concentrations of QDs. There was no measurable variation of film thickness between areas of high roughness and low roughness.

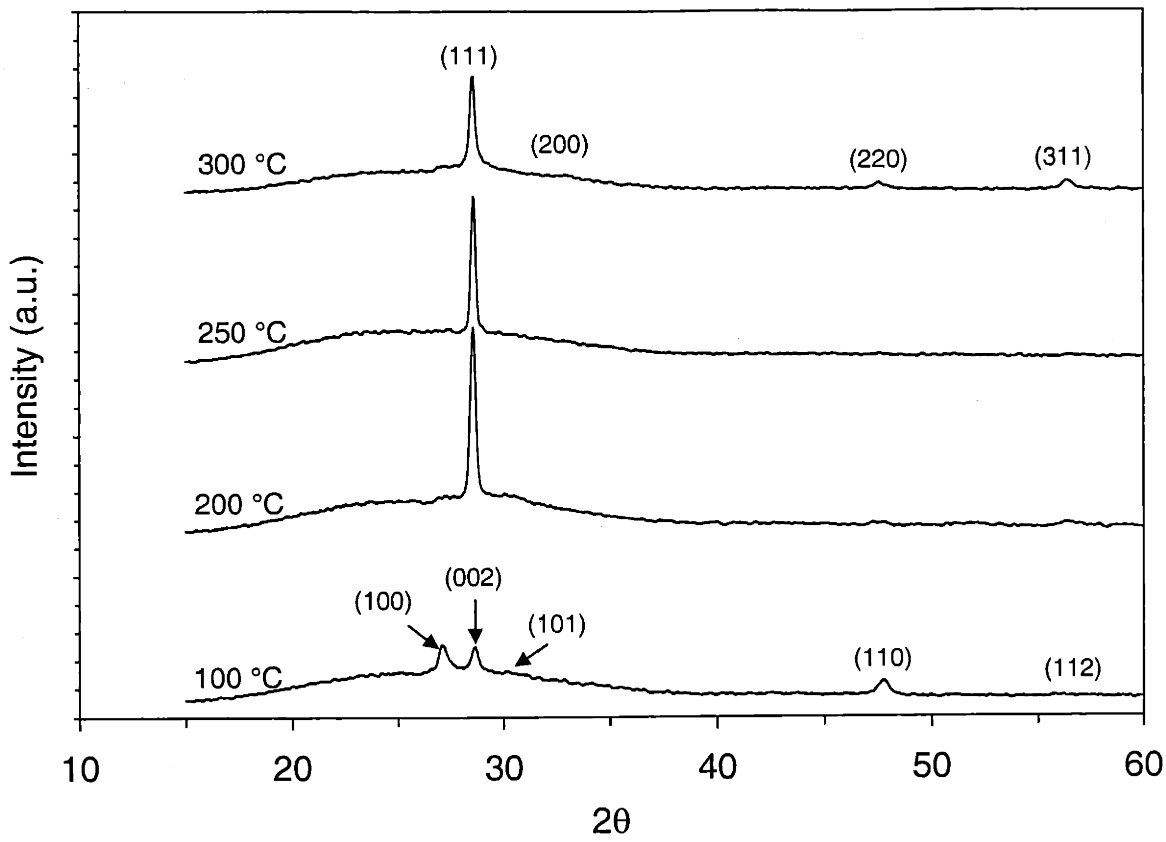

Figure 4.2 X-ray diffraction profiles of thin films grown at 100 °C, 200 °C, 250 °C, and 300 °C without nanocrystals. The zinc blende and wurtzite diffraction peaks have been labeled above the 300 °C and 100 °C data, respectively. The absence of some of the cataloged powder diffraction peaks indicates the presence of a preferred film orientation. The high relative intensity of the zinc blende (111) and wurtzite (100) peaks show that those planes are primarily oriented parallel to the film surface. The broad background peak is due to amorphous scattering from the glass substrate.

The photoluminescent behavior of the thin films, with and without nanocrystals, was examined. When excited by 340 nm light, samples with films grown without nanocrystals produced broad, low intensity emission at 450 nm. This broad luminescence was produced by the glass substrate rather than by the ZnS film. Glass substrates without ZnS exhibited the same PL peak. Furthermore, the PL was greatly diminished in intensity at excitation wavelengths less than 335 nm due to the absorption of excitation light by the ZnS film. The ZnS matrix is not photoluminescent at room temperature.

The PL spectra of films containing NCs grown at the four different temperatures are shown in Figure 3. The PL of the 100 °C and 200 °C films is nearly identical to that of the NCs in pyridine. The low concentration of NCs deposited in the films eliminated the red-shift due to agglomeration. The PL peaks of the films grown at 250 °C and 300 °C are blueshifted, approximately 9 nm and 16 nm, respectively. Nanocrystals cast onto glass substrates and annealed at 250 °C for 1 hr show a 6 nm blueshift similar to that in the 250 °C films. This suggests that the blueshift is independent of the ZnS matrix and is a result of alteration of the CdSe-ZnS nanocrystal. The blueshift is likely caused by alloying of the CdSe core with the surrounding ZnS shell. The inward diffusion of the Zn and S atoms reduces the radius of low bandgap material in the NC thereby reducing the size of the exciton. The broad background emission to the red of the main peak is due to radiative emission from deep trap states on the NC surface.[8] Photoluminescence excitation (PLE) scans verify that the film luminescence is dominated by the NC luminescence and that the excitons recombining in the NCs were also generated in the NCs and not the ZnS matrix. The evolution of the film emission at the red tail of the PL peak (590 nm) was measured for the 100 °C sample and for the NCs dispersed in pyridine, as shown in Figure 3. Instead of enhancing the photoluminescence, absorption by the ZnS matrix of some of the excitation light below 350 nm reduces the luminescence of the films when compared to that of NCs in pyridine solution. Also, the variation of the PL intensity near the NC band edge is roughly proportional to the absorption of the NCs near their band edge. PLE scans taken with an emission wavelength of 650 nm behave similarly, indicating that the broad low intensity red emission also comes from recombination of the excitons in the NCs.

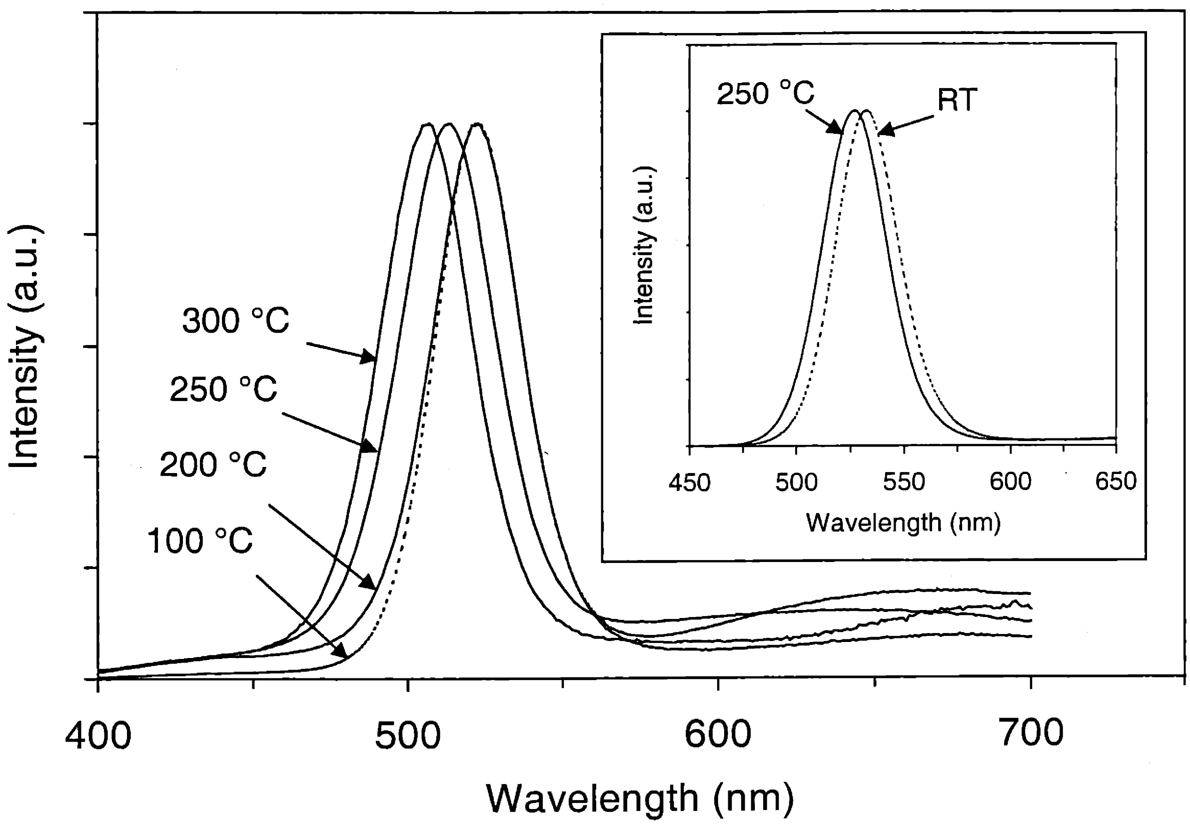

Figure 4.3 Photoluminescence spectra of NC-containing thin films grown at 100 °C, 200 °C, 250 °C and 300 °C, and of NCs cast onto a glass substrate and heated to 250 °C and left at room temperature (inset). The excitation wavelength used was 380 nm. The peak heights have been normalized. The peak maxima for the samples are 523 nm, 523 nm, 514 nm, and 507 nm, for the 100 °C, 200 °C, 250 °C, and 300 °C samples, respectively. The broad emission to the red of the main peak is due to radiative recombination at surface states on the NC.

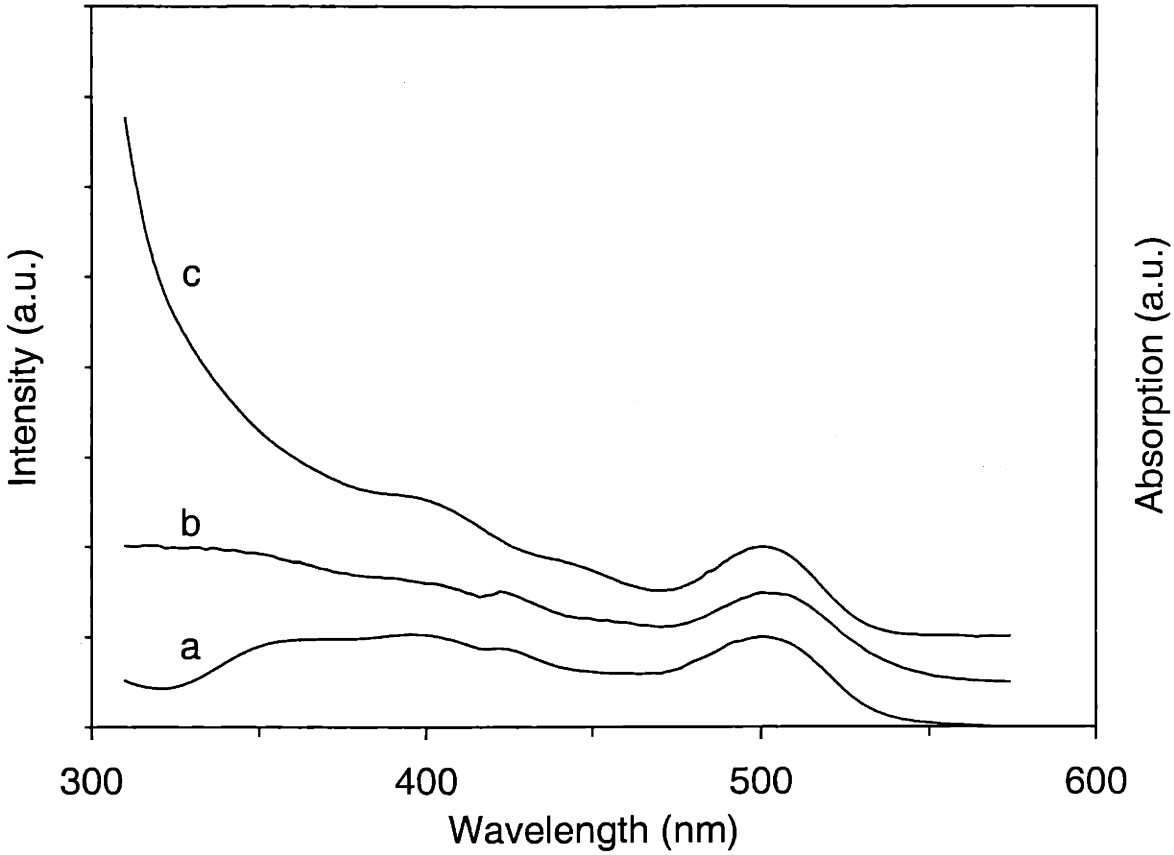

Figure 4.4 Photoluminescence excitation scans of a NC containing thin film grown at 100 °C (a), and NCs dispersed in pyridine (b) along with the absorption spectrum of the NCs in pyridine (c). The emission wavelength is 590 nm, which is on the red tail of the main PL peak. The drop-off in intensity, seen in (a), at wavelengths less than 340 nm is due to absorption of the excitation light by the ZnS matrix. The PLE and absorption maxima near 500 nm correspond to the first absorption line of the NCs.

4.4 Conclusions

The photoluminescent behavior of the NC-ZnS thin film composites is set by the PL behavior of the NCs. The excitons confined in the NCs are not significantly influenced by the ZnS matrix. The variation in the PL wavelength is caused by alterations, such as alloying, of the NCs themselves due to heating during thin film synthesis. Preventing alloying of the NCs requires low deposition and operating temperatures (<250 °C). While the matrix does not significantly influence the PL behavior of the films, its quality is critical when electronic excitation (e.g. CL) is involved. For electroluminescent and cathodoluminescent applications the thin film crystallinity must be high to reduce the number of deep trap states in the matrix. This requires relatively high deposition temperatures (>200 °C). To produce quality NC-ZnS composite thin films, minimization of alloying must be balanced against loss of crystallinity.

4.5 References

1. B. O. Dabbousi, M. G. Bawendi, O. Onitsuka, and M. F. Rubner. Appl. Phys. Lett. **66** (1995) 1316.

2. M. Danek, K. F. Jensen, C. B. Murray, M. G. Bawendi, J. Cryst. Growth **145** (1994) 714.

3. M. Danek, K. F. Jensen. C. B. Murray, and M.G. Bawendi, Chem. Mater. **8** (1996) 173.

4. J. Rodriguez-Viejo, K.F. Jensen, H. Mattoussi, J. Michel, B. O. Dabousi, and M. G. Bawendi, Appl. Phys. Lett. **70** (1997) 2132.

5. C. Kagan, C. B. Murray, and M. G. Bawendi, Phys. Rev. Lett. **76** (1990) 3203.

6. D. I. Chepic, A. L. Efros, A. I. Ekimov, M. G. Ivanov, V. A. Kharchenko, I. A. Kudriatsev, and T. V. Yazeva, J. Lumin. **47** (1990) 113.

7. B. O. Dabbousi, J. Rodriguez-Viejo, F. V. Mikulec, J. R. Heine, H. Mattoussi, R. Ober, K. F. Jensen, and M. G. Bawendi, J. Phys. Chem. B **101** (1997) 9463.

Chapter 5

QD-layer / ZnS-layer Structures

5.1 Controlled Layer Deposition of QDs and ZnS

It was found in the previous chapter that ES-OMCVD has some drawbacks. Both the quantum dot and ZnS deposition was non-uniform. The spatial non-uniformity of the QD deposition is attributed to the collimated behavior of the QD/solvent spray. Rather than becoming a completely diffuse cloud before reaching the substrate, the sprayed particles remained in a fairly narrow and irregular jet, and the QDs are deposited mainly on certain areas of the substrate surface. The resulting differences in QD density over the substrate surface gives rise to great variability of luminescence across the substrate. Furthermore, the enhancement of surface roughness in areas with greater concentrations of QDs makes laying down an electrode on top to create a device much more difficult.

The variabiltiy of the ZnS deposition rate over the surface is due to the uneven flow of precursors past various areas of the substrate surface. The small diameters of the susceptor (substrate mount) and the quartz reactor tubing enclosing the substrate, produced a significantly increased gas flow at the edges of the substrate relative to the center. Also, if the substrate/susceptor was not precisely centered in the quartz reactor tube, the increased gas flow around the narrower gap gave rise to a gradient in the ZnS growth from one side of the substrate to the other. Improving the ZnS deposition would require a reactor setup with uniform temperature and flow over the entire substrate. However, even with a uniform ZnS growth rate the increased roughness produced by incorporating the QDs is still an obstacle.

Furthermore, it was found that heating the substrate to temperatures greater than 200 °C while QDs were present on the surface degraded their luminescence. High quality ZnS film growth on Si, GsAs, or glass, via CVD occurs at temperatures above 400 °C to maximize the crystallinity of the film that is put down. So another, low temperature deposition process is needed.

5.1.1 Atomic Layer Epitaxy

Atomic layer epitaxy (ALE) is an alternative to normal CVD that produces epitaxial films at low temperatures (150 °C to 250 °C).[1] ALE is a pulse-purge technique. One of two reactive precursors (A) is flowed into a reactor and reacts with the substrate surface. Then the remaining amount of un-reacted precursor A is removed by switching the precursor flow to the system exhaust and allowing the carrier gas to purge the reactor leaving behind a monolayer of chemisorbed A. The other precursor (B) is then introduced into the reactor and reacts with the previously deposited monolayer of A. After a sufficient amount of precursor is introduced the surface is saturated with B. Then the reactor volume is purged in the same way as with A. Then A is flowed into the reactor again and reacts with the monolayer of B just added, and the process is repeated. Figure 5.1 is a cartoon of the precursor reactions. This process is repeated until the desired film thickness is reached. The advantages of ALE are: the elimination of gas phase nucleated particles (because the precursors are not present in the reactor at the same time), a uniform, conformal coating over the entire substrate surface (because of the saturation and chemisorption of the precursor over the entire substrate), and control of film thickness down to the monolayer (due to the self-limiting nature of the reaction with one precursor reacting with the monolayer deposited previously and the excess unable to react).

ALE has been used to deposit a wide range of semiconductors and device structures. These include numerous II-VI,[2] III-V[3,4], and group IV semiconductors[5] as well as metals such as tungsten[6]. Device structures include strained layer superlattices[7] and multiple quantum wells[8], dielectric mirror structures such as the surface passivation[9] of quantum well lasers and oxide multilayer reflectors[10], as well as electroluminescent devices[11]. High quality films of ZnS and ZnSe have been deposited on Si substrates using dimethyl zinc (DMZn) as the Zn precursor and hydrogen sulfide (H_2S) and hydrogen selenide (H_2Se) as S and Se precursors respectively.[1] The growth rate for ZnS

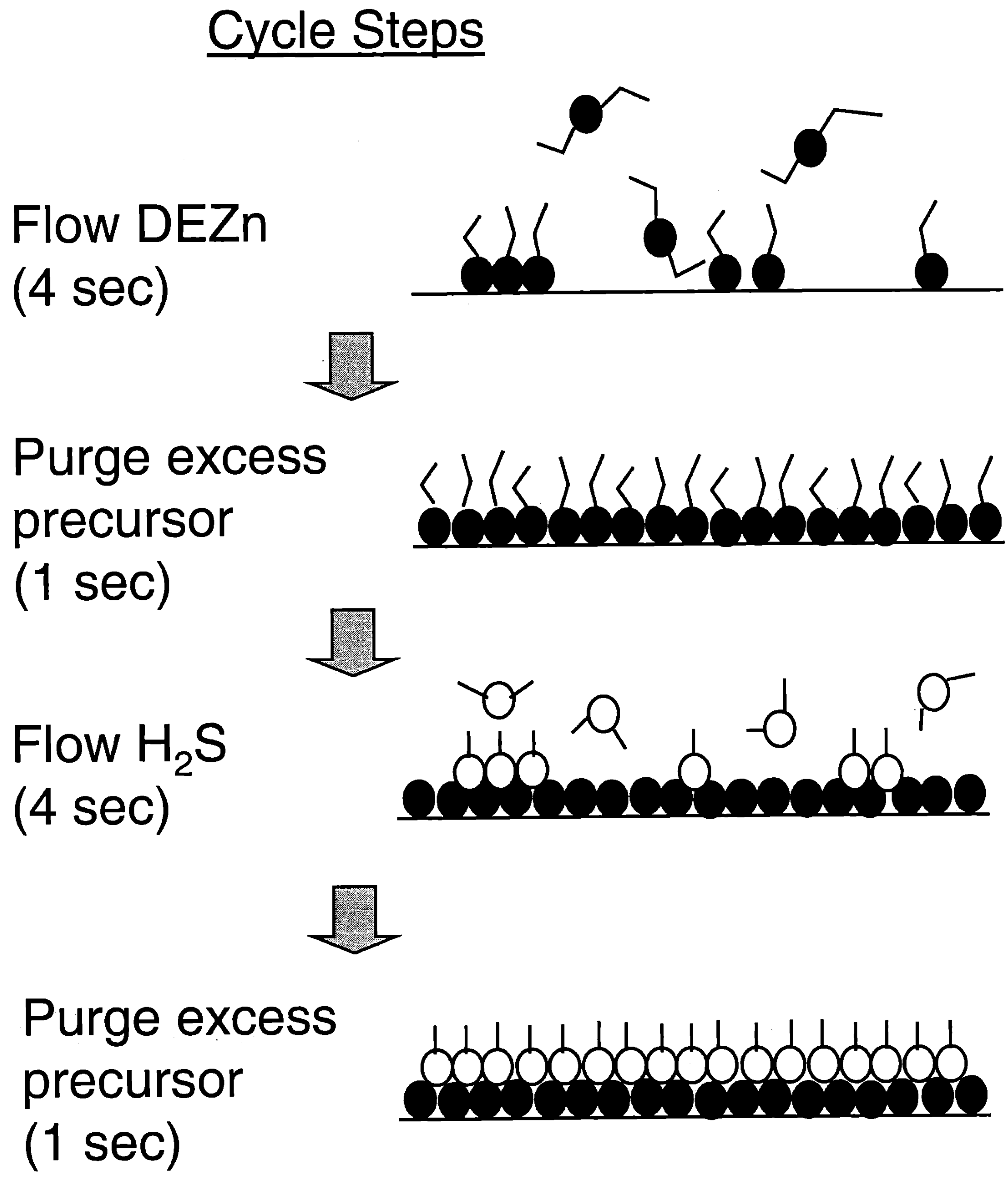

Figure 5.1 Cartoon of precursor arrival and reaction with surface during ALE.

was found to saturate at 2.7 Å/cycle in the temperature range of 120 °C to 170 °C. This temperature range is compatible with the presence of (CdSe)ZnS QDs during deposition.

The general evolution of ALE growth rate with temperature is shown in Figure 5.2. The behavior has been discussed by Suntola, et. al.[12] At low temperatures, the growth rate diverges from one monolayer/cycle either through condensation of precursor onto the surface, producing a high growth rate, or because the reaction activation energy is too large for reaction at low temperatures, causing a low growth rate. At deposition temperatures at which ALE occurs, excess physisorbed reactant desorbs from the surface and is purged away between precursor pulses and the reactants are able to react completely producing a surface-saturated, chemisorbed layer. At higher temperatures, thermal decomposition of one or both precursors will produce a high growth rate, while premature loss of precursor ligand at the surface inhibits chemisorption at the next precursor pulse, causing a low growth rate.

5.1.2 Casting of QDs

Uniform deposition of the QDs themselves is possible either by spin casting or drop casting. Drop casting the QDs requires that they be dispersed in a solvent that wets the substrate. If it does not, QDs will aggregate at the edge of the droplet of solvent and leave a large number of QDs in a ring pattern. If it does wet the substrate, then the entire area of the substrate contacted by the solvent will receive an even coating of QDs. TOPO-capped QDs, being soluble in non-polar solvents because of the octyl chains which hang off its surface, are insoluble in polar solvents. This insolubility in polar solvents is used in a casting technique in which CdSe QDs are dispersed in a 9:1 octane/octanol solution. As the solvent evaporates, the octane, which has the higher vapor pressure, is removed first and the QDs become increasingly unstable in the increasingly octanol rich solution, and slowly precipitate out in an ordered lattice.[13] Close-packed films have also been synthesized with QDs capped with pyridine.[14] The QDs are dispersed in a 9:1 solution of methanol/pyridine and cast onto a Si substrate, with a thin surface oxide, which has been treated to make the SiO_2 surface more hydrophilic.

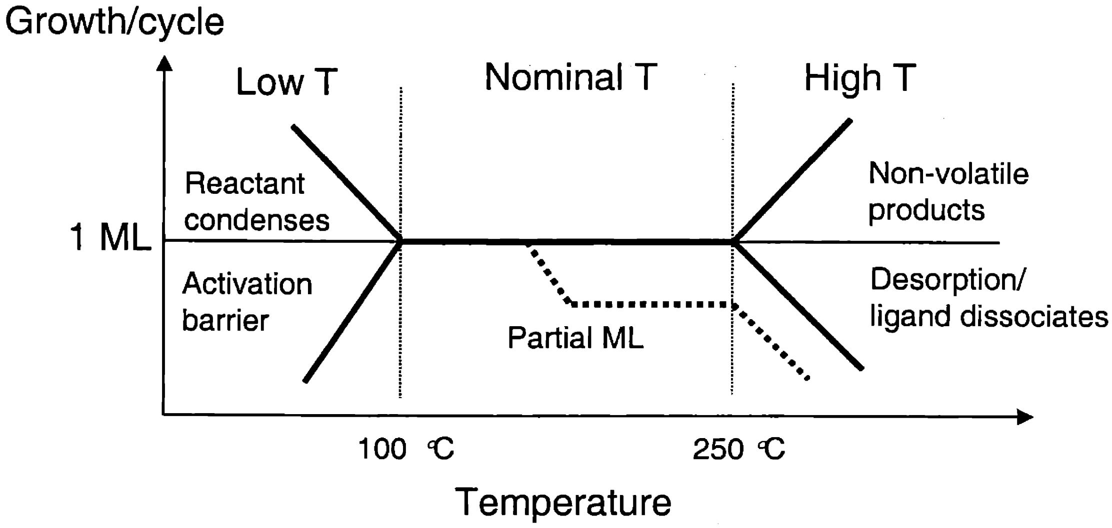

Figure 5.2 Cartoon of deposition regimes for ALE growth. The partial monolayer growth represents the possibility of desorption from the surface.

Spinning is less sensitive to the wetting properties of the solvent and provides very uniform films, however, the films produced are typically only 10 monolayers of QDs thick or less. Spinning has been shown to be very useful for creating QD layer / thin film structures. H. Mattoussi, et. al.[15] spun (CdSe)ZnS quantum dots onto a hole conducting poly(phenylene vinylene) (PPV) layer to create an electroluminescent device.

To create uniform QD-inorganic film layers we use the techniques of drop and/or spin casting to create a close packed QD layer, and ALE to create a controlled thickness ZnS thin film. Rather than atomic layer epitaxy, the ZnS deposition will be referred to as atomic layer deposition (ALD) since the films being put down are not epitaxial.

5.2 Atomic Layer Deposition Reactor and Conditions

The reactor used in this work to deposit ALD ZnS films is a vertical flow cold-wall chemical vapor deposition (CVD) reactor with substrate heating carried out by a meandering filament beneath a molybdenum susceptor, on which the substrate rests. Figure 5.3 gives a rough cartoon of the reactor. The pulse – purge switching of the precursors to and from the reactor are carried out by automated pneumatic valves. These valves bypass the precursor flow to the reactor exhaust while off and allow the carrier gas (H_2) to flow unimpeded into the reactor. The carrier gas flow acts to purge the reactor of excess precursor. When switched "on" though, the precursor flow is merged with that of the carrier gas to the reactor and the substrate is dosed with the precursor. The pneumatic valves are controlled via computer using a Visual Basic program.

Typical ALD growth conditions are: 20μmol/min flow diethylzinc (DEZn), 400 μmol/min flow H_2S, a substrate temperature of ~150 °C, and a total carrier gas flow rate of 1.0slm with 0.5slm flowing through the separate H_2S and DEZn lines. The DEZn flow rate is set by the bubbler temperature and the flow rate of a stream of H_2 gas which flows through the bubbler and carries the DEZn to the reactor. The reaction chamber is open directly to the vent, producing a reactor pressure of <5 torr. Having the reaction chamber open to the exhaust equalizes its pressure with that of the exhaust lines for the precursors. In this way, the precursors will immediately flow to either the reaction chamber or the exhaust after the pneumatic valve has switched the flow. The pulse times for DEZn and

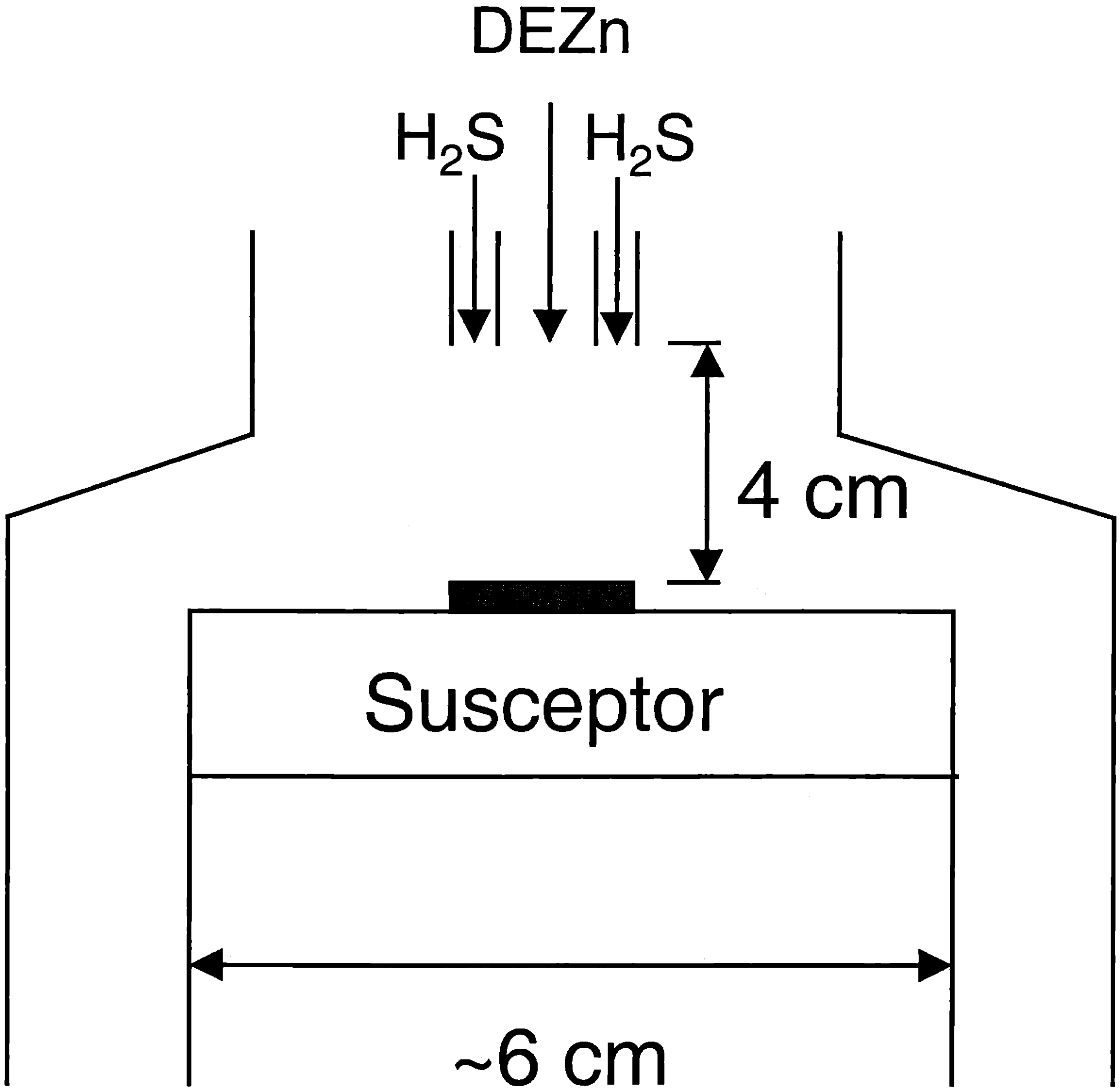

Figure 5.3 Cartoon of reaction chamber used for ALD of ZnS. Both the DEZn and H_2S are introduced from above. The susceptor is heated from below by a meandering resistive filament. The substrate is heated while in contact with the susceptor.

H_2S are both 4 seconds. The purge time after each pulse is 1 second. With an estimated 0.5L volume above the substrate to be cleared by the purge, the necessary purge time is calculated to be <0.2 seconds.

5.3 ALD ZnS Film Characterization

Film thicknesses and roughnesses were determined through the use of a Tencor P-10 Profilometer. X-ray diffraction (XRD) measurements were carried out on a Rigaku 300 rotating anode diffractometer in the θ-2θ configuration using CuKα radiation. Surface chemical analysis of ZnS films was carried out via X-ray photoelectron spectroscopy using a Physical Electronics Model 5200C X-ray Photoelectron Spectrometer using MgKα radiation. The surface morphology of films was examined using tapping-mode atomic force microscopy with a Digital Instruments Nanoscope IIIa Scanned Probe Microscope.

Various parameters, such as the DEZn and H_2S pulse times and flow rates, purge times, and the substrate temperature, were varied in an attempt to determine a processing window in which monolayer by monolayer growth would occur. Unfortunately, varying the growth temperature, H_2S flow rate, and pulse and purge times, generally gave variations of film growth rate, leading to the conclusion that while the pulse-purge technique gave uniform film growth over large areas, incomplete saturation or purging of the reactor at various conditions precluded monolayer by monolayer growth. For example, deposition at 150 °C, one second pulse times, 4 second purge times, 20μmol/min DEZn and 400 μmol/min H_2S is found to have a growth rate of 1.4 Å/cycle. This is about half of what is expected for a full monolayer growth per cycle. Increasing the H_2S flow rate dramatically increases the growth rate. This indicates that chemisorption of the H_2S is incomplete even with flow rates greatly in excess of those of DEZn. Although the growth rate is low, the films deposited still remain viable for further work. The improved film morphology and control over film thickness enabled by using a pulse-purge technique was a significant improvement over that of ES-OMCVD.

XRD spectra taken of ZnS films grown on glass showed that the films are in fact ZnS and exhibit XRD peaks indicating growth in the (111) direction. Use of the Scherrer Equation indicates grain sizes on the order of 400 Å to 500 Å, which is an improvement over that of the films grown by ES-OMCVD. The surface roughness is also greatly improved with roughnesses on the order of 100 Å for a 2500 Å thick film. Also, the growth rate is uniform over substrates with dimensions of inches. Thus, these films may be better suited to the production of electronic devices.

ZnS was found to nucleate on and cover the surface of both glass and gold substrates after only a few cycles of growth. XPS measurements of nominally 20Å thick films laid down on both glass and gold at 200 °C found nearly complete suppression of the Si XPS peaks and complete suppression of the gold peaks. Figure 5.4 shows the XPS spectrum of 20 Å ZnS deposited on glass. Using the peak areas of the S 2p and the Zn 3p peak, 6700 and 12000 counts-eV/sec, respectively, with sensitivity factors of 0.666 and 0.946, respectively, gives a film surface composition of 43% S and 57% Zn. The Si 2p peak near 170 eV is produced by emission from the glass substrate. The C and O peaks are likely due to surface contamination from exposure to air after removal from the reactor.

AFM measurements of 20 Å films of ZnS on both gold and glass suggests the nucleation of ZnS islands rather than epitaxial growth. Figure 5.5 shows the AFM surface measurement of the ZnS on glass. AFM (1μm x 1μm) scans of bare glass and 20 Å ZnS on glass. The rms roughness of both the bare and ZnS coatedglass is 1.3nm. Some particles are found on the ZnS coated sample as well. This particulate contamination may be the source of pinholes. Maintaining system cleanliness is a major requirement for maintaining film quality. AFM measurements were also carried out with bare and ZnS coated gold films. The AFM scans are shown in Figure 5.6. Due to the high granularity of the Au film the rms roughnesses are significantly higher than that of the glass at 4nm. But, the crystal planes of the Au granules enable a clear view of the island growth of the ZnS on the Au.

In general, the films were found to be insulating and possessed a break down electric field of 0.5 MV/cm (1 V/nm). This breakdown field was determined with electrical testing of thin films of ZnS deposited on gold and on ITO. Electrical testing of 20nm ZnS sandwiched between a Au film and a 100μm to 200μm diameter Au pad showed breakdown (shorting out) at about one volt. 100nm films of ZnS shorted out at

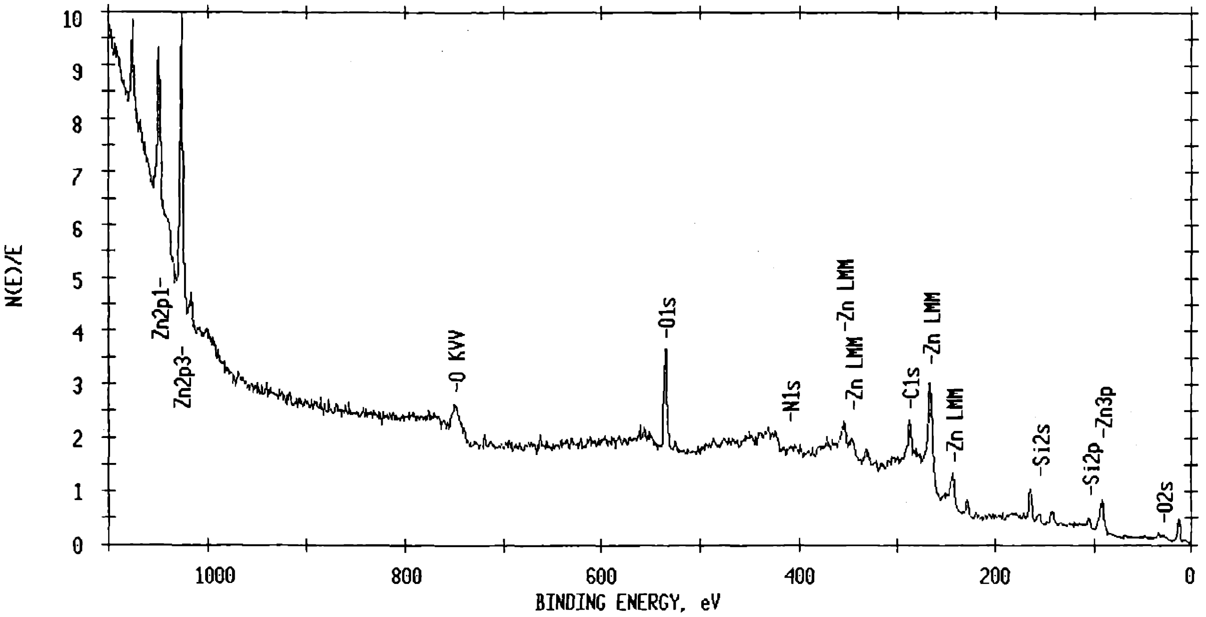

Figure 5.4 XPS spectrum for 20Å thick ZnS film on glass. Elemental analysis using using Zn 3p and S 2p peaks gives a film composition of 43% S and 57% Zn. The Si 2s peak found near 170 eV indicates that signal still apparent from the underlying glass substrate. The C and O peaks are likely due to surface contamination acquired as the sample was stored outside of the reactor and transported to the XPS equipment.

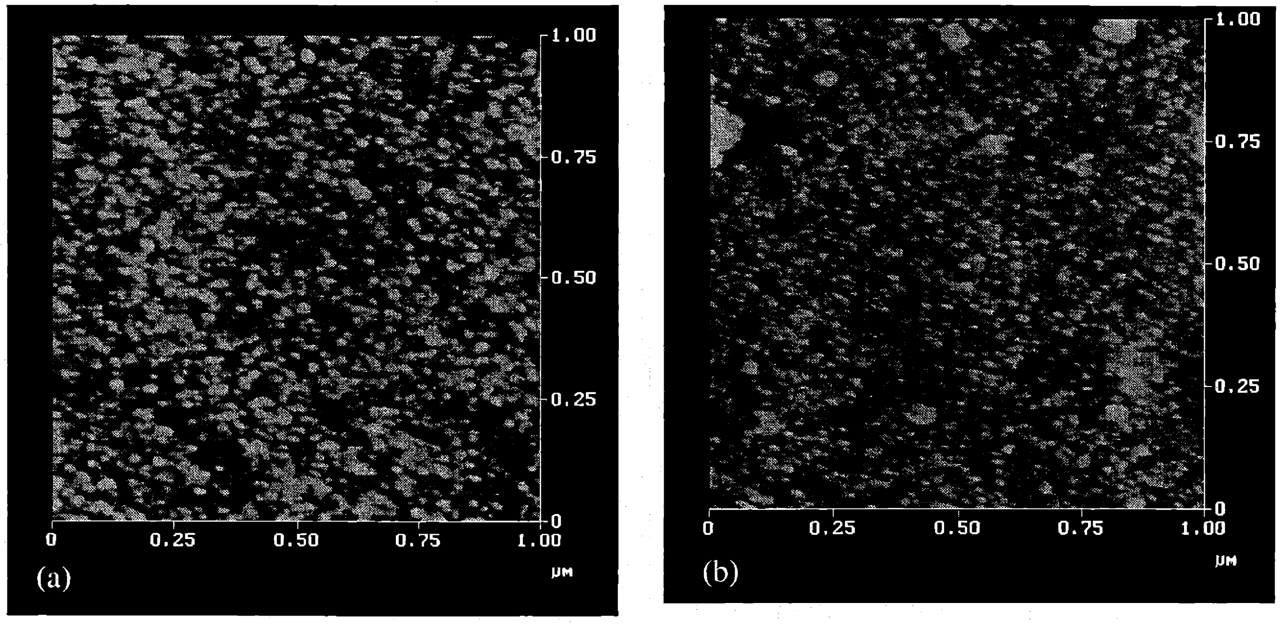

Figure 5.5 AFM (1µm x 1µm) scans of (a) bare glass and (b) 20 Å ZnS on glass. The color code runs from zero to 10 Å height for (a) and 20 Å for (b). Some larger particles and small projections are seen in (b).

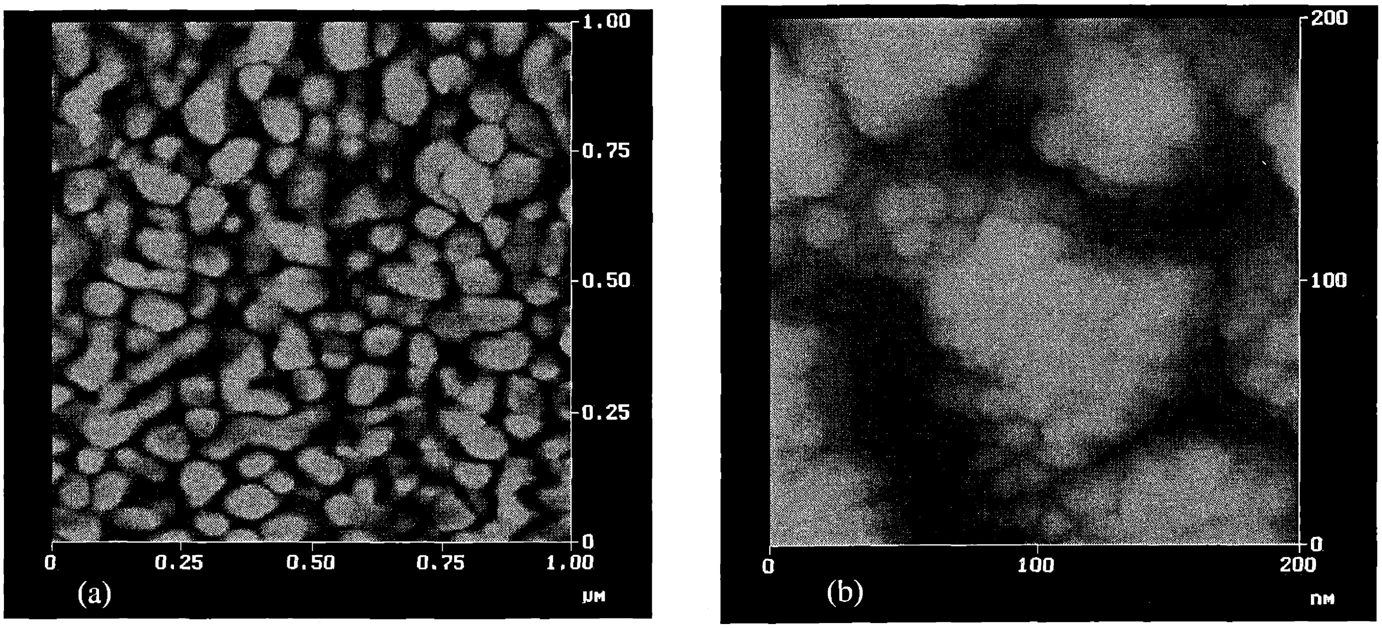

Figure 5.6 AFM (1μm x 1μm) scan of (a) bare gold and (200nm x 200nm) scan of (b) 20 Å ZnS on gold. The color code runs from zero to 30 Å height for both (a) and (b). The granular nature of the gold substrate is easily seen in (a). The island formation of the ZnS on the gold is seen in (b).

voltages above 5V. Furthermore, the capacitances measured (approximately 500nF for 100nm) corresponded to those calculated by assuming that the ZnS is an ideal dielectric.

One hundred nanometer thick films grown on ITO with 200μm wide aluminum lines evaporated on as top electrodes also exhibited breakdown behavior at voltages greater than 5V. Examination of an ITO/100nm ZnS/Al device using an Avtech pulse generator and an oscilloscope indicated that the device acts as a simple capacitor. The device was tested in a circuit with the pulse generator applying a voltage pulse to the ITO electrode and a 1 kΩ resistor in series with the device after the aluminum electrode, and with ground after the resistor. The voltage present at each electrode was monitored using the two channels of the oscilloscope. Applying a voltage of less than 5V (the breakdown voltage for this thickness as indicated by the Au/ZnS/Au measurements) gave a voltage spike which decayed exponentially to zero by the time 5μs had elapsed. Removal of the voltage produced a mirror image negative voltage which decayed exponentially. This is classical RC-circuit charge-discharge behavior. The RC time constant was calaculated using the FWHM of the initial current spike. This gave a capacitance of approximately 1 nF which is about twice what one would expect for a 100nm insulator with a relative dielectric constant of 9 (ε_r of ZnS) sandwiched between electrodes of about 0.6mm^2 (0.2mm Al x 3mm ITO). Increasing the voltage above 5V leads to a voltage drop across the resistor (i.e. a non-zero baseline voltage at the aluminum electrode). This voltage is found to be the difference between the pulse voltage and 5V, which indicates that the device conducts after 5V. Small spikes in the voltage drop across the resistor are also seen and become more frequent and prominent with increasing voltage.

Current-voltage measurements on Al/ZnS/ITO films also reveals Schottky diode like behavior. Figure 5.7 is a I-V curve for a 250nm ZnS film between ITO and aluminum. The voltage is being applied to the aluminum electrode. It appears that applying a negative voltage to the aluminum contact produces a significantly lowered breakdown voltage. However, when exposed to a gradually increasing application of voltage, some films appear to become charged before breaking down and exhibit highly insulating behavior, as shown in Figure 5.8.

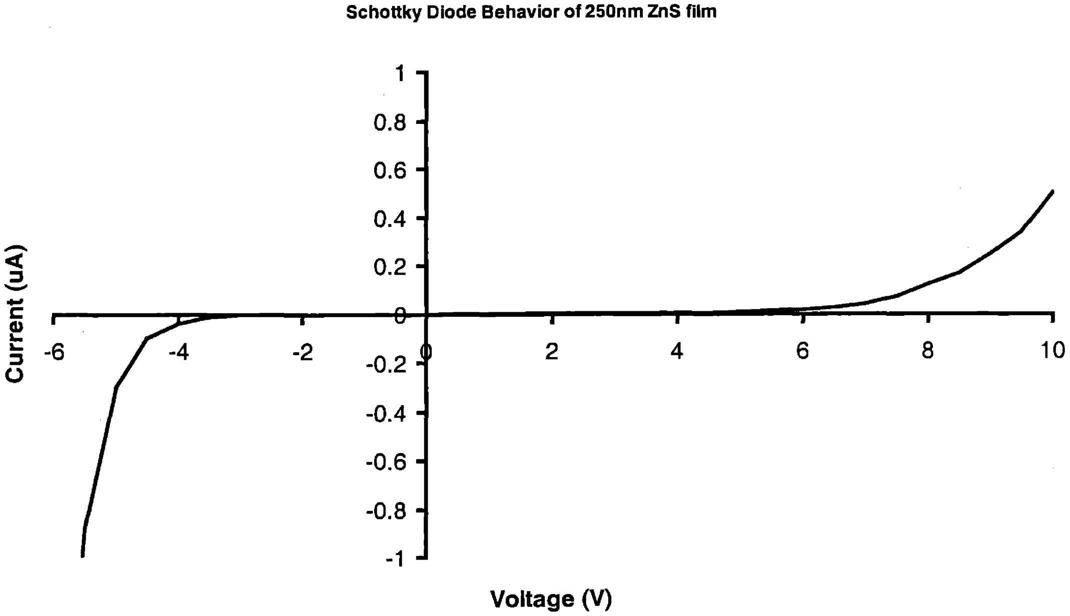

Figure 5.7 I-V characteristics of 250nm ZnS film between ITO and Al contacts. The voltage is applied to the Al contact. Film exhibits asymmetric Schottky diode behavior. Asymmetry caused in part by difference in contact material.

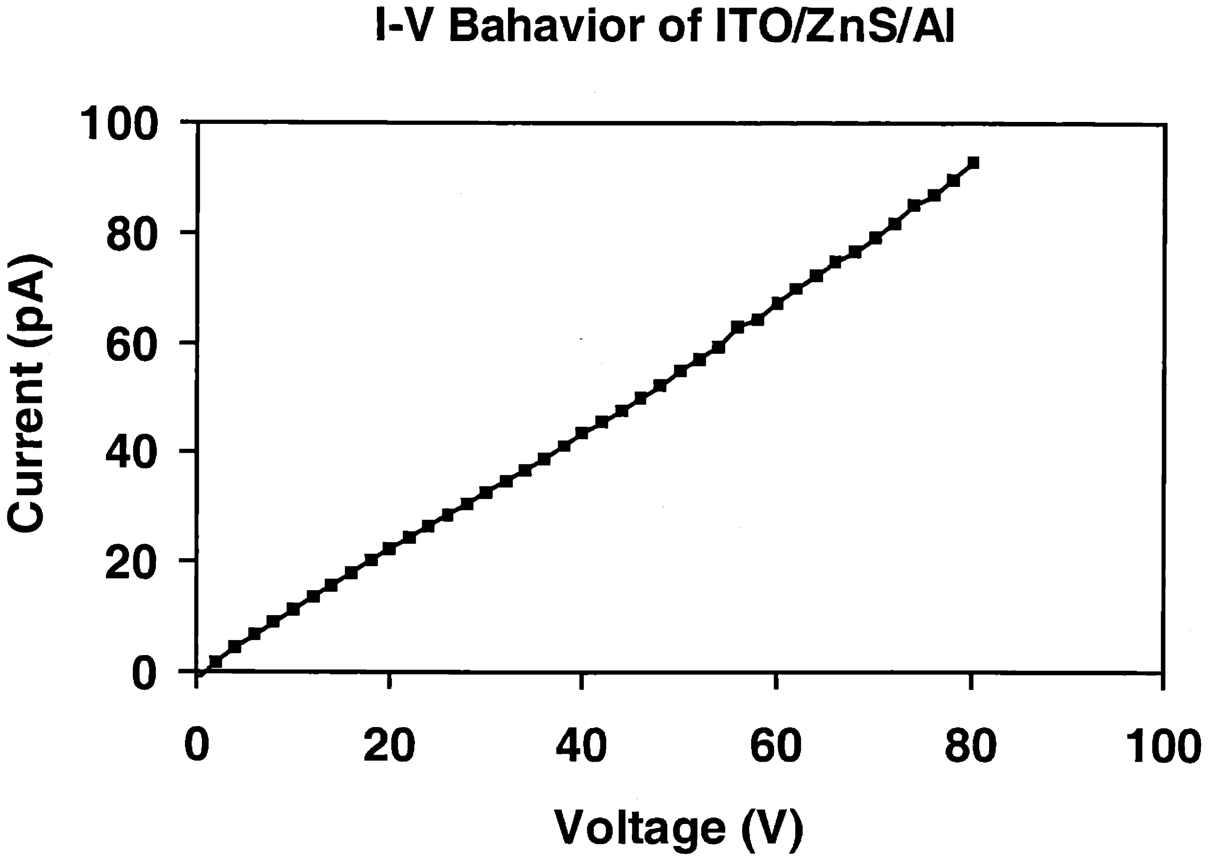

Figure 5.8 I-V curve of 500nm thick ZnS film. After being allowed to charge, the film is resistive to breakdown and exhibits a high resistivity

Attempts to dope the ZnS n-type with chlorobutane[16], chlorotrimethylsilane, and iodoethane[17] were not successful. It is possible that the deposition temperature (< 250 °C) was insufficient to crack the doping compound.

5.4 Casting of QDs on ZnS films

Both drop casting and spin casting were tried as means to deposit thin films of QDs on ZnS.

5.4.1 Drop Casting

ZnS, which has a polar surface due to its ionic nature, is wet by polar solvents rather than non-polar solvents. Both of the casting techniques described in section 5.1.2 involve the use of polar solvents. To determine the robustness of the QDS during the ZnS deposition process, the strongly bound TOPO cap was removed by repeated washing in excess quantities of a more weakly bound ligand. Specifically, following the QD treatment in Chapter 4 to prepare the QD for incorporation into ZnS, the QDs were cap-exchanged with pyridine. Unfortunately, a solution with 10% pyridine still did not wet ZnS. A wetting solution was created by precipitating the QDs out of pyridine solution and then redispersing the wet powder left after discarding the supernatant in a 1:99 solution of pyridine/methanol with the pyridine added first to completely redisperse the QDs. After casting the pyridine/methanol solution onto the glass or ZnS substrate, the solvent slowly evaporates and leaves large macroscopic clumps of QDs over the surface of the substrate.

To increase the evaporation rate and improve the solubility of the QDs in the casting solvent the QDs were derivatized with a polar compound that would bind well to the QD surface and also be compatible with methanol as a solvent. 6-mercapto-1-hexanol binds well to the QD surface via the SH end and is miscible with methanol due to the OH end. TOPO-capped quantum dots were cap-exchanged with mercaptohexanol by precipitating out the TOPO capped QDs from solution, redispersing them in mercaptohexanol, and heating the solution in an oil bath at 60 °C to 70 °C while stirring for 2+ hours. After this cap-exchange process, the QDs were precipitated out from solution with hexane and then redispersed in methanol. Films cast using this solution were much more uniform than that of the pyridine solution.

Thin films of ZnS were subsequently deposited on the QD layers and photoluminescence measurements were carried out to determine how well the QDs held up to the ALD conditions. Green-emitting QDs (13 Å CdSe radius, 9 Å ZnS shell thickness) and red-emitting QDs (30 Å CdSe radius, 13 Å ZnS shell thickness) with emission peaks at 520nm and 635nm in dilute solution, respectively, were drop cast on a ZnS thin film. 300nm ZnS and 500nm ZnS were deposited at 200 °C on the green and red QDs, respectively. Figures 5.9 and 5.10 show the emission spectrum of the QDs in dilute solution, as cast, and after being embedded in the ZnS. The significant shift to the red for both sizes of QDs when going from dilute solution to cast film is not surprising. Energy transfer from small QDs to larger ones in a close-packed thin film cause a red-shift in the luminescence of that film relative to that of the QDs in dilute solution.[18] However, depositing ZnS shifts the luminescence of the green QDs only slightly and hardly at all for the red QDs. This indicates that the QDs are robust to experiencing temperatures up to 200 °C (just as was seen with the ES-OMCVD films in Chapter 4). Profilometry measurements of the film surface show final roughnesses of only up to 50nm for a total film thickness of 500nm to 1000nm. This is considerably better than the film roughnesses achieved with ES-OMCVD.

5.4.2 Spin Casting

Highly uniform thin films of (CdSe)ZnS QDs have been produced by spin casting.[15] TOPO capped QDs dispersed in toluene with an optical density of ~10 over a 1mm optical path length, were spun onto a PPV thin film. In this work, QDs capped with TOPO and mercaptohexanol were spun onto ITO and ZnS using the same technique as described in Reference 15. Quantum dot solutions with optical densities of 3 to 4 over a 1mm optical pathlength were spun onto ITO and ZnS at 6000 rpm. After spinning, the color of the film due to interference effects was uniform, which indicates that the film thickness is uniform with less than 10% variation in film thickness. ZnS films were then deposited on top of the spun films. Examination with a UV lamp showed that the

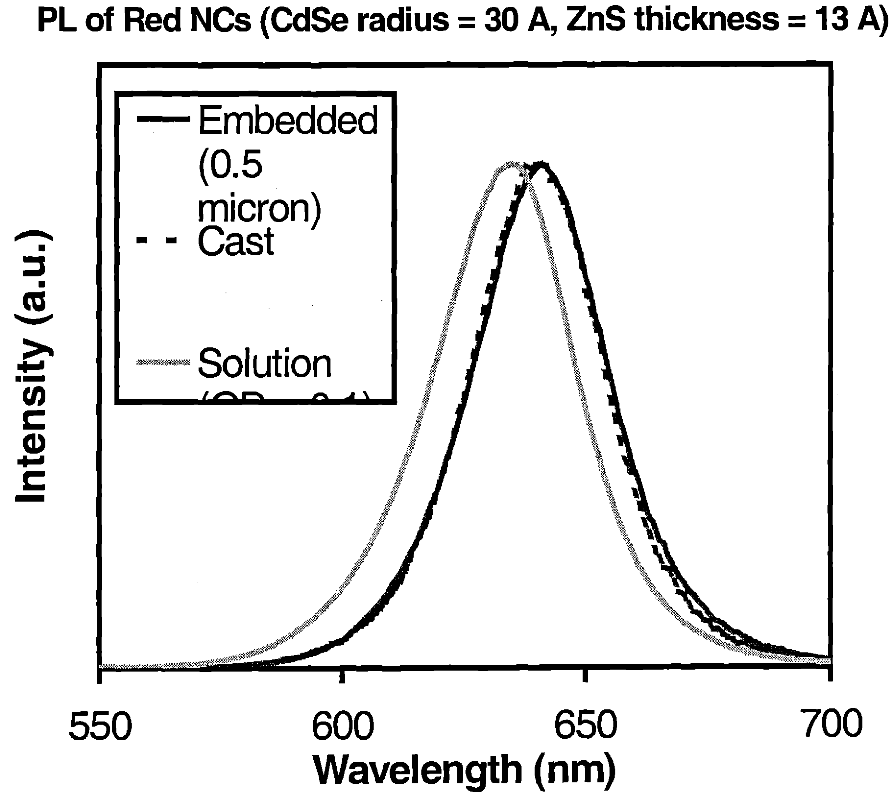

Figure 5.9 Photoluminescence spectra of 30 Å radius CdSe, 13 Å thickness ZnS QDs. The luminescence spectra include that for the QDs dispersed in hexane, cast onto a ZnS film, and after deposition of another ZnS film on top of the QDs. The luminescence spectrum of the QDs is unaltered by the deposition process.

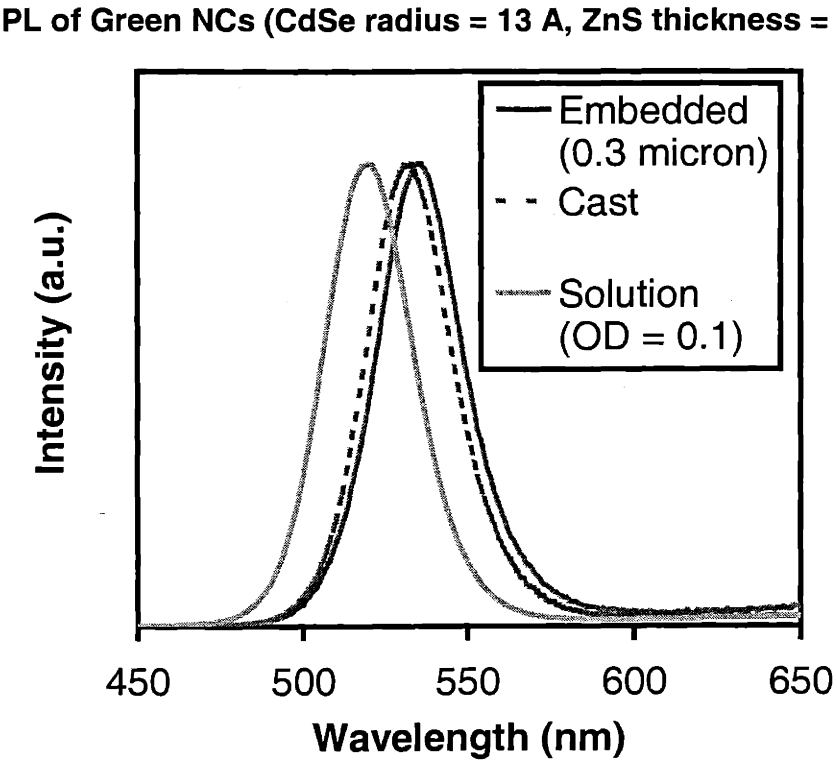

Figure 5.10 Photoluminescence spectra of 13 radius CdSe, 9Å thickness ZnS QDs. The luminescence spectra include that for the QDs dispersed in hexane, cast onto a ZnS film, and after deposition of another ZnS film on top of the QDs. The luminescence spectrum of the QDs shifts slightly to the red during the deposition process.

luminescence of the QDs is preserved. The mercaptohexanol capped QDs were dimmer than the TOPO capped QDs, so TOPO capped QDs were used in the luminescence experiments described in the next chapter.

5.5 Conclusions

ALD enables the production of uniform layers of ZnS at deposition temperatures which are not destructive of the QDs. XPS has shown the presence of ZnS at a very early point in the deposition process, which indicates the absence of a film nucleation barrier. Electrical measurements have demonstrated the insulating nature of the ZnS. Furthermore, drop casting and, especially, spin casting the QDs produces uniform thin films of QDS. These layers of QDs are not damaged during subsequent deposition of newer ZnS layers.

5.6 References

1. C. T. Hsu, Thin Solid Films **335** (1998) 284.
2. A. Szcerbakow, E. Dynowska, K. Swiatek, and M. Godlewski, J. Cryst. Growth **207** (1999) 148.
3. R. Ares, C. A. Tran, and S. P. Watkins, Appl. Phys. Lett. **67** (1995) 1576.
4. K. S. Boutros, F. G. McIntosh, J. C. Roberts, S. M. Bedair, E. L. Piner, N. A. El-Masry, Appl. Phys. Lett. **67** (1995) 1856.
5. G. Eres, Appl. Phys. Lett. **67** (1995) 1727.
6. J. W. Klaus, S. J. Ferro, and S. M. George, Thin Solid Films **360** (2000) 145.
7. S. Dosho, Y. Takemura, M. Konagai, and K. Takahashi, J. Cryst. Growth, **95** (1989) 580.
8. R. Engelmann, J. Ferguson, and R. Solanki, Appl. Phys. Lett. **70** (1997) 411.
9. N. C. Frateschi, M. Y. Jow, P. D. Dapkus, and A. F. J. Levi, Appl. Phys. Lett. **65** (1994) 1748.
10. H. Kumagai, K. Toyoda, K. Kobayashi, M. Obara, and Y. Limura, Appl. Phys. Lett. **70** (1997) 2338.
11. W. Kong, J. Fogerty, R. Solanki, and R. T. Tuenge, Appl. Phy. Lett. **66** (1995) 419. T. Suntola,
12. C. B. Murray, C. R. Kagan, and M. G. Bawendi, Science **270** (1995) 1335.
13. C. A. leatherdale, C. R. kagan, N. Y. Morgan, S. A. Empedocles, M. A. Kastner, and M. G. Bawendi, Phys. Rev. B **62** (2000) 2669.
15. H. Mattoussi, L. H. Radzilowski, B. O. Dabbousi, E. L. Thomas, M. G. Bawendi, and M. F. Rubner, J. Appl. Phys. **83** (1998) 7965.
16. T. Yasuda, B. P. Zhang, and Y. Segawa, J. Cryst. Growth **175** (1997) 583.
17. S. Yamaga, A. Yoshikawa, and H. Kasai, J. Cryst. Growth **106** (1990) 683.
18. C. R. Kagan, C. B. Murray, and M. G. Bawendi, Phys. Rev. B **54** (1996) 8633.

Chapter 6

Electric Field Induced Quenching of Quantum Dot Luminescence

Cathodoluminescence (electrodarkening), photoluminescence (photodarkening), and single QD spectroscopy experiments suggest that introducing a charge into a QD causes the QD to stop emitting light.[1,2] This darkening is thought to occur because the recombination of an exciton within the charged QD results in the transfer of energy to the "excess" charge carrier via an Auger process rather than the emission of a photon. To further probe this behavior we synthesized QD/ZnS layer devices with ITO and Al electrodes on top and bottom, with the aim of directly charging the QDs via direct charge injection from either electrode. H. Mattoussi et.al.[3] have demonstrated electroluminescence produced by the "simultaneous" injection of both electrons and holes into a QD thin film. In our devices, either electrons or holes are injected into the layer, not both, with the ZnS layers behave as insulating layers, which prevent charge injection from one or both electrodes at low voltages. The QD layer was deposited either right next to the ITO, the Al, or between two layers of ZnS. Figure 6.1 has cartoons of the device structures.

6.1 Device Synthesis

Glass substrates with 3mm wide stripes of ITO were used as the base for the devices. For the first device, 20 Å radius CdSe, ZnS overcoated QDs were spun onto the ITO-striped glass from 3.6 OD/mm solution in toluene at 6000rpm. Then a nominally 100nm thick film of ZnS was deposited on top at 150 °C. A 200 μm Al line oriented so

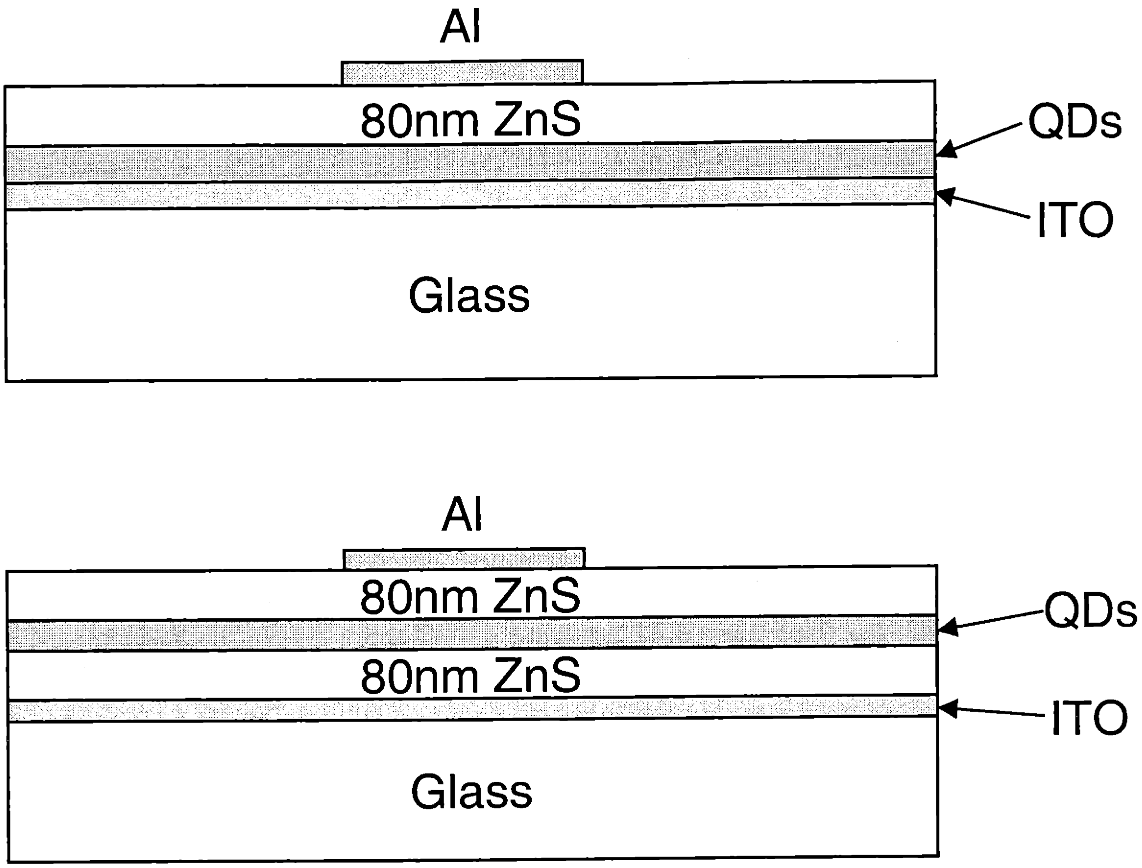

Figure 6.1 Cartoons of two device structures synthesized for QD quenching experiments. The top device has QDs next to the ITO electrode and may be charged directly from that electrode when a field is applied. The bottom device isolates the QDs between two layers of ZnS. Charge injection from the electrodes should be very difficult. The third device places the ZnS next to the ITO and the QDs next to the aluminum.

that it is perpendicular to the ITO stripe was then evaporated on top for the second electrical contact. Profilometry measurements with a P-10 Tencor profilometer give the layer thicknesses as: 65nm QDs, 85nm ZnS. The second device was produced by depositing a 100nm ZnS film onto the substrate first and then depositing a QD film and then second ZnS film as described above. Profilometry gives the layer thicknesses as: 80nm ZnS, 30nm QDs, 80nm ZnS.

6.2 Photoluminescence measurements

A cartoon of the charging/photoluminescence experiment is shown in Figure 6.2. The 514nm line of an Argon ion laser is used to excite the QDs. The laser light strikes the glass/ITO side of the device and the PL emission from the QDs is gathered using a Nikon 0.7NA 60X air objective lens from the same side. The light is then reflected to a Princeton Instruments intensified CCD camera via a Triax 320 spectrometer. The PL was both spatially and spectrally resolved. The intensity of the laser light was adjusted to give a QD PL intensity of about 150 counts/pixel/100msec for most of the runs. This corresponds to approximately 10 μW in the 30 μm spot size.

A voltage was then applied to the ITO electrode while the Al electrode was grounded. The voltage applied was stepped from zero volts to a positive voltage, held at that voltage for some length of time, dropped back to zero volts and held at zero (usually the same amount of time as that for the positive voltage). Then the voltage is stepped to a negative voltage equal in magnitude to the positive voltage applied previously and for the same amount of time, then dropped back to zero and the cycle repeated. The use of both positive and negative voltage is to probe any asymmetry in the device operation. The periods of zero voltage are present to allow the device to discharge.

6.3 Results

All of the devices exhibit an immediate (<100ms) decrease in luminescence intensity upon the application of the external field. Moreover, the application of a positive field on the ITO gave a significantly larger drop in luminescence than did a negative applied bias. Also, at high voltages all of the films exhibited some slow

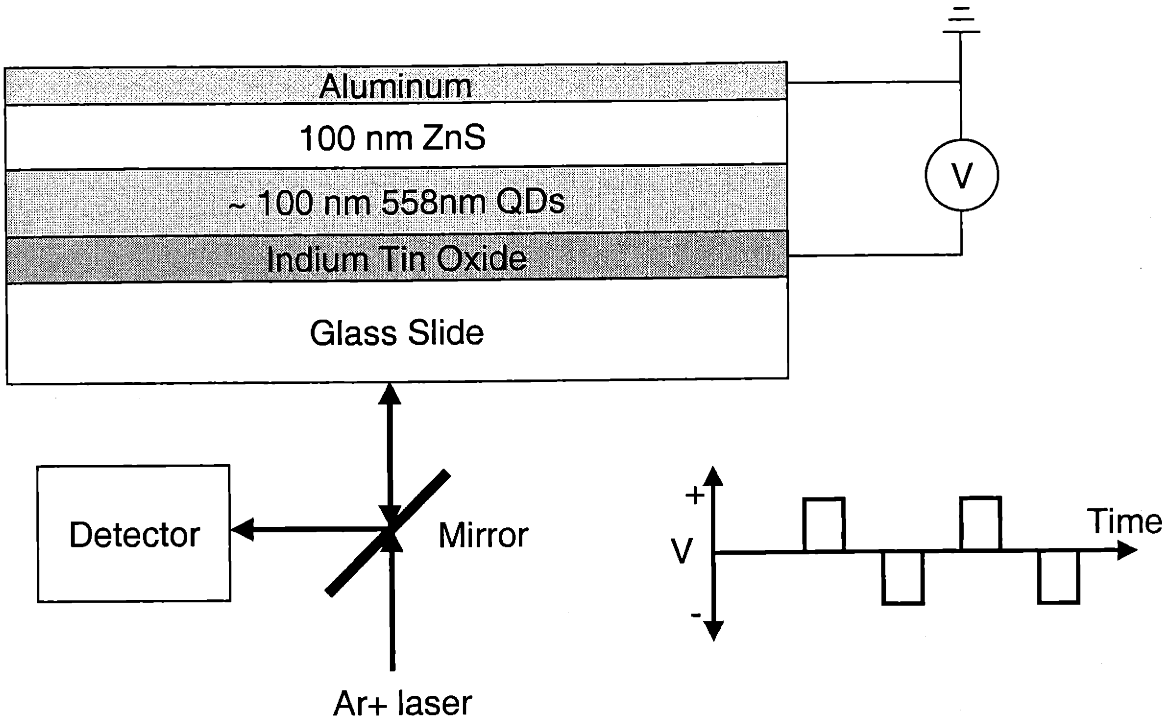

Figure 6.2 Cartoons of basic device structure and testing setup. Ar+ laser light excites the quantum dots and their luminescence is gathered and sent to a detector. At the same time an step-wise applied voltage is used to modulate the luminescence.

quenching after the rapid drop with positive applied voltage, but a negative bias produced almost no discernible additional quenching.

6.3.1 *ITO/QDs/ZnS/Al*

Figures 6.3 and 6.4 show the PL behavior of the Al/ZnS/QD/ITO device with low voltages and high voltages respectively. At low voltages only a sharp drop in the luminescence is observed. However, the drop when a positive voltage is applied to the ITO is significantly larger than that when a negative voltage is applied. At higher voltages a slow drop in the luminescence is seen when the positive voltage is applied but the PL when a negative voltage is applied follows the recovery of luminescence seen when zero voltage is applied. The steady drop in luminescence over the course of a run is likely due to bleaching of the QDs, which may be a combination of photo-oxidation as well as Auger charging.[1]

6.3.2 *ITO/ZnS/QDs/ZnS/Al*

Examination of the luminescence from the second device shows very similar behavior, as seen in Figure 6.5. The main difference is that the slow drop in PL at high positive voltages is retarded. This suggests that the QD layer is effectively preventing charging of the QDs from the ITO or Al. The current at low voltages ranges from 35pA to 500pA when raising the voltage from 3V to 10V. This nonlinearity in current rise suggests that the ZnS films are not contacted ohmically with the electrodes. At high voltages the films breakdown and pinholes form/ become more dominant, which leads to wide variability in the current. However, the photoluminescence behavior remains steady and as expected which suggests that the QD layer still experiences the electric field typical for that voltage.

6.3.3 *ITO/ZnS/QDs/Al*

The photoluminescent behavior of this device is significantly different from that of the previous two. The drop off in intensity is significantly slower at the moderate laser intensities normally used (10 μW in a 30 μm spot size). Increasing the intensity of the

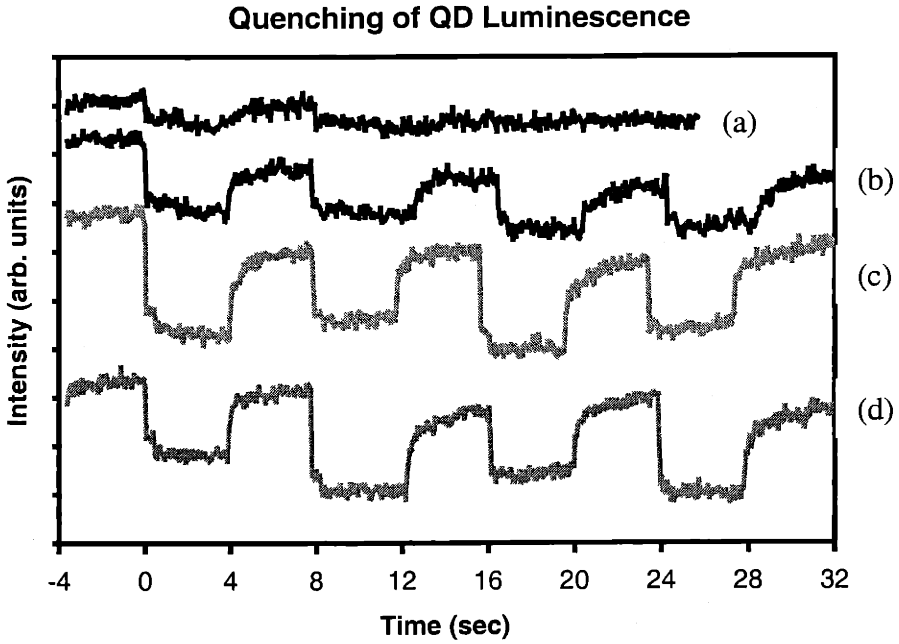

Figure 6.3 PL quenching behavior of the Al/ZnS/QD/ITO device. The voltages applied are (a) 1V,(b) 3V,(c) 5V, and (d) 7V, which correspond to $7x10^4$ V/cm, $2*10^5$ V/cm, $3x10^5$ V/cm, and $5x10^5$ V/cm, respectively. All of these fields are below that of the breakdown field strength of the ZnS determined in the previous chapter. Increasing the applied voltage increases the drop in luminescence. With constant applied voltage no further drop in luminescence is observed.

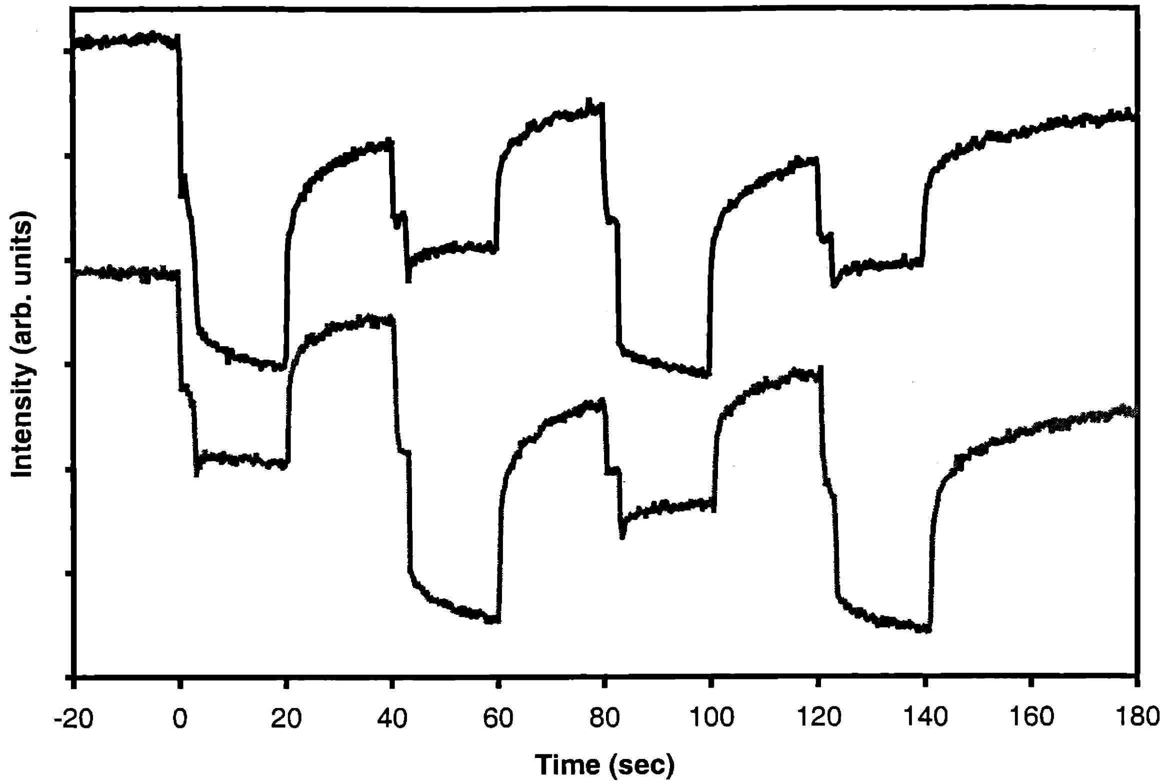

Figure 6.4 Quenching behavior with the same device at 20V. The upper curve represents a run with the positive voltage applied first. The second run with the negative applied first. Note that at the positive voltage, a further drop in luminescence is observed. The PL with negative voltage applied exhibits the same PL recovery seen with zero volts applied.

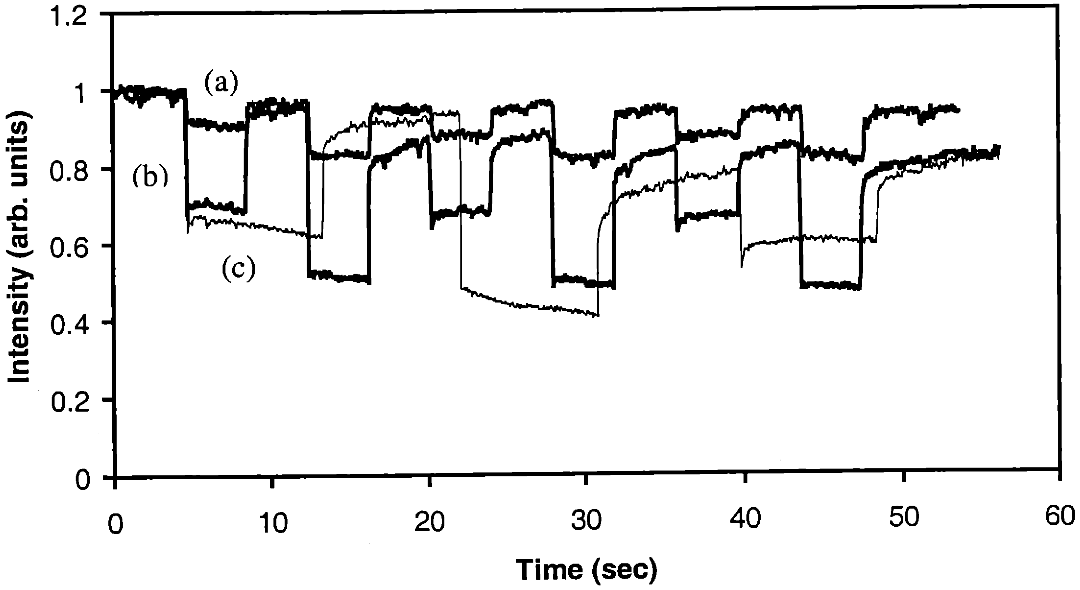

Figure 6.5 Photoluminescence quenching of the ITO/ZnS/QD/ZnS/Al structure. The voltages applied during the four second voltage-on data are (a) 10V and (b) 25V, with the negative bias applied first. The relative flatness of the intensity at both positive and negative applied biases suggest that the ZnS is successfully preventing charge injection from both electrodes. The longer 10 second voltage-applied run at 27 V (c) suggests that a small amount of charge injection is occuring and that the luminescence recovery is quite slow after the fast quenching process ceases. The currents flowing through the devices are (a) 500 pA, (b) 1.5 μA, and (c) 0.5 μA, at positive voltages. The decrease in current going from 25V to 27V is typical for these devices at high voltages where current appears to be dominated by pinholes. The intensity scale is actually a relative scale: gives fractional intensity.

beam increases the speed of the quenching. Figure 6.6 show the luminescence drop when various voltages are applied. Figures 6.7 and 6.8 show the increased quenching rate as the incident light intensity is increased with applied voltages of 5V and 10V, respectively.

6.4 Discussion

The quenching of the luminescence of the QDs is attributed to charging of the QDs as mentioned above. Two possible sources of charge of the QDs are the QDs themselves via photoionization, and from the conducting electrodes. Both of these sources are considered below.

Two regimes of quenching appear to be present: a fast drop (<100ms) upon the initial application of a voltage and a slow drop at higher voltages.

The rapid drop in the photoluminescence is influenced by at least two parameters: the voltage applied and the intensity of the incident laser light. Increasing the applied voltage increased the magnitude of the drop, while increasing the intensity of the beam increased the speed of the drop, as seen for the ITO/ZnS/QD/Al device. At incident laser intensities half or less than that usually used for illuminating the device, the initial quench has a time scale of several seconds. At usual incident intensities ($10\mu W/700\mu m^2$) the initial quench behaves similarly to an ITO/polymer/QD/Al device studied by others in the Bawendi group.

It has also been found that the current produced by the device under bias is influenced by the beam intensity. The device produces almost no current (<10 pA) when no light is applied and becomes more conducting as the intensity of the incident beam is increased (80 pA at 5V and both 20 and 250 cts/pixel/0.1sec, and 130 pA at 5V and 3300 cts/pixel/0.1sec). The corrent was approximately the same for both positive and negative bias on the ITO. At 10 V, the variation in current was significantly greater. With intensities of 100, 300, and 3300 cts/pixel/0.1sec the currents with positive voltage on the ITO were 120 pA, 210 pA, and 530 pA, respectively. The negative bias currents were 390 pA, 400 pA, and 710 pA, respectively. The increase in current with the presence of light suggests that the device is behaving as a photodiode, with charge generation occuring by photoionization of the QDs. C. Leatherdale[4] found that when exciting QDs

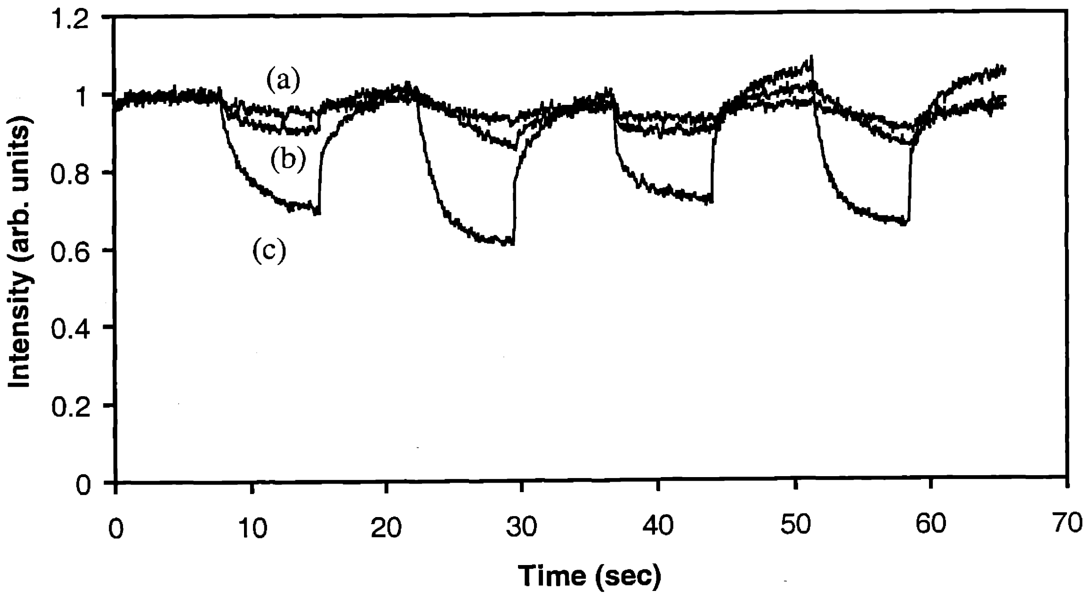

Figure 6.6 Quenching produced by applied voltage on ITO/ZnS/QD/Al device. Note that the rate of quenching is significantly reduced compared to the two previous devices. The voltages applied are (a) 3V, (b) 5V, and (c) 10V. Maximum quenching found with 10V: about 40%

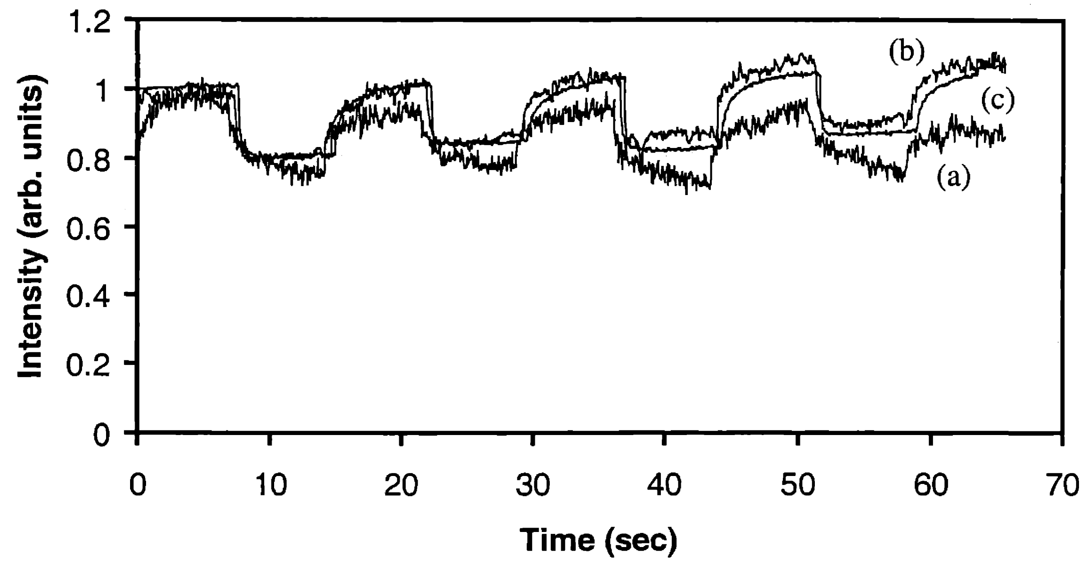

Figure 6.7 Increasing quenching rate at 5V applied to ITO/ZnS/QD/Al device. QD PL intensities (cts/100msec/pixel): (a) 20, (b) 250, (c) 3300. As the intensity increases the noise level goes down because there is more signal. The sharpness of the quenching is clearly seen to increase with increasing illumination. Quenching is approximately 20%.

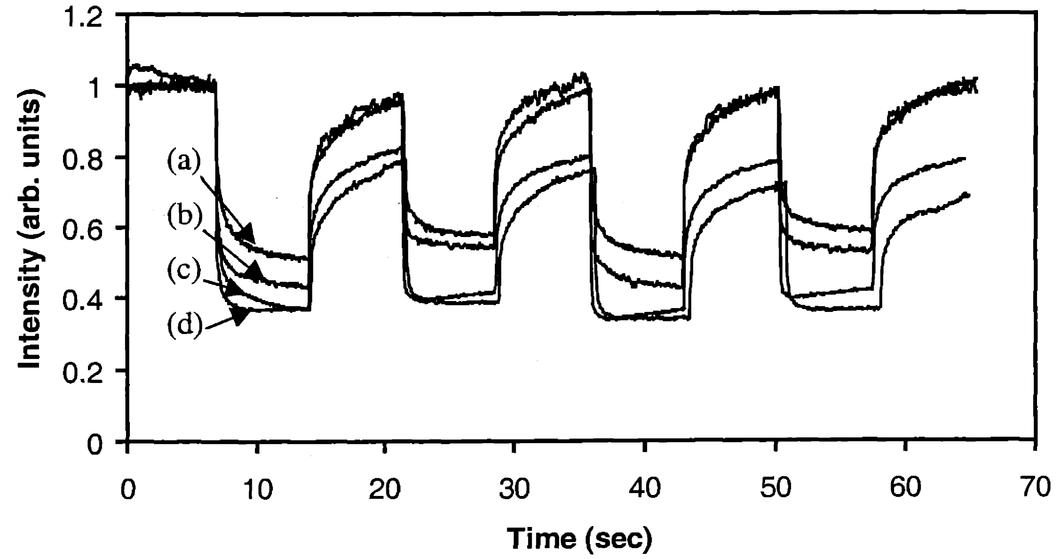

Figure 6.8 Increasing quenching rate at 10V applied to ITO/ZnS/QD/Al device. QD PL intensities (cts/100msec/pixel): (a) 100, (b) 250, (c) 1300, (d) 3300. As the intensity increases the noise level goes down because there is more signal. The sharpness of the quenching is clearly seen to increase with increasing illumination. Quenching reaches levels of 60%.

optically, approximately one in 10,000 excitons eject a carrier rather than recombine radiatively. Thus the QDs are known to photoconduct. Furthermore, the wavelength of the incident light, 514nm, makes absorption by the ZnS or organic matrix unlikely, making the QDs the sole source of additional free carriers in the material.

One possible explanation for the fast drop behavior is via photoionization of the QDs. By applying a voltage, the newly generated charge, which may be trapped near the QD and therefore would normally rapidly reenter and make it bright again, is helped by the electric field to tunnel further away from the QD, leaving it dark longer. These photoionization produced charges may also tunnel into a neutral QD, thereby making it dark as well. After the voltage is removed, charges which remained near the photoionized QDs are able to diffuse back rapidly and re-establish a zero voltage charged QD-carrier equilibrium. Charges which are in deep traps or have entered neutral QDs while higher voltages were applied take longer to return to photo-ionized QDs and neutralize them. This explanation, however, does not explain the asymmetry between the positive and negative biases.

Another possible explanation is that electrons at the surfaces of the electrodes are aided in tunneling into the QD layer by a photoelectric type effect. The incident light may raise the surface electron energy so that it can more easily tunnel into or through the ZnS layer. Assuming that the ITO and Al respond differently to the incident light, this may explain the asymmetry of the quenching between positive and negative bias applied to the ITO. With the ITO positively biased the Al injects electrons into the ZnS layer which may screen the field in the ZnS and increase it in the QD layer. Other experiments involving other metals as electrodes are necessary to evaluate this possibility.

The slow drop seen at higher voltages is probably due to carrier injection from the electrodes. At the higher voltages, the breakdown field of the ZnS films is exceeded which allows carriers to flow through it. Hole injection from the ITO electrode is another possibility. After the voltage is removed, there is a slow discharge of the QD layer.

6.5 Conclusions

Layered devices of ZnS and QDs have been synthesized. Applying electric fields to these devices has provided evidence for several electronic processes which influence the light emission of the QDs. Two different charging mechanisms have been proposed to explain the fast quenching of the luminescence: photoionization and electric field enhanced carrier migration from photoionzed QDs, and enhanced carrier injection from the electrodes via a photoelectric effect. However, further work is required to elucidate their relative contributions, if any. A longer-time quenching process at higher voltages is attributed to direct charging of the QDs from an electrode.

6.6 References

1. J. Rodriguez-Viejo, H. Mattoussi, J. R. Heine, M. K. Kuno, J. Michel, M. G. Bawendi, and K. F. Jensen, J. Appl. Phys. **87** (2000) 8526.
2. R. G. Neuhauser, K. T. Shimizu, W. K. Woo, S. A. Empedocles, and M. G. Bawendi, Phys. Rev. Lett. **85** (2000) 3301.
3. H. Mattoussi, L. H. Radzilowski, B. O. Dabbousi, E. L. Thomas, M. G. Bawendi, and
4. M. F. Rubner, J. Appl. Phys. **83** (1998) 7965.
5. C. A. Leatherdale, MIT Thesis, 2000.

Publications

J. W. Lee, V. C. Sundar, J. R. Heine, M. G. Bawendi, K. F. Jensen, *Full Color Emission from II-VI Semiconductor Quantum Dot-Polymer Composites*, Adv. Mat. **12** (15), 2000

J. Rodriguez-Viejo, H. Mattoussi, J. R. Heine, M. K. Kuno, J. Michel, M. G. Bawendi, K. F. Jensen, *Evidence of photo- and electrodarkening of (CdSe)ZnS quantum dot composites*, J. Appl. Phys. **87** (12) 8526, 2000

J. R. Heine, J. Rodriguez-Viejo, M. G. Bawendi, and Klavs F. Jensen, *Synthesis of CdSe quantum dot-ZnS matrix thin films via electrospray organometallic chemical vapor deposition*, J. Cryst. Growth **195** (1-4) 564, 1998

B. O. Dabbousi, J. Rodriguez-Viejo, F. V. Mikulec, J. R. Heine, H. Mattoussi, R. Ober, K. F. Jensen, and M.G. Bawendi, *(CdSe)ZnS Core-Shell Quantum Dots: Synthesis and Characterization of a Size Series of Highly Luminescent Nanocrystallites*, J. Phys. Chem. B **101** (46) 9463, 1997

Patent (pending): Moungi Bawendi, Jason Heine, Klavs F. Jensen, Jeffrey Miller, and Ronald Moon, *Quantum Dot White and Colored Light Emitting Diodes*